UNIVERSIDADE ESTADUAL PAULISTA

PROGRAMA DE PÓS-GRADUAÇÃO EM FÍSICA

ÁREA DE FÍSICA APLICADA

Hurst Exponent: An Indicator of Weak Chaos

Daniel Borin

INSTITUTO DE GEOCIÊNCIAS E CIÊNCIAS EXATAS

RIO CLARO

2026

UNIVERSIDADE ESTADUAL PAULISTA "JÚLIO DE MESQUITA FILHO"

Instituto de Geociências e Ciências Exatas
Câmpus de Rio Claro

Daniel Borin

Hurst Exponent: An Indicator of Weak Chaos

Tese de doutorado apresentada ao Instituto de Geociências e Ciências Exatas do Câmpus de Rio Claro, da Universidade Estadual Paulista "Júlio de Mesquita Filho", como parte dos requisitos para a obtenção do título de Doutor em Física.

Orientador: Prof. Tit. Edson Denis Leonel

RIO CLARO - SP
2026

B734h

Borin, Daniel
Hurst Exponent: An Indicator of Weak Chaos / Daniel Borin. -- Rio Claro, 2026
146 p.

Tese (doutorado) - Universidade Estadual Paulista (UNESP), Instituto de Geociências e Ciências Exatas, Rio Claro
Orientador: Edson Denis Leonel

1. Hurst exponent. 2. Weak chaos. 3. Stickiness. 4. Dynamical traps. 5. Hamiltonian systems. I. Título.

Sistema de geração automática de fichas catalográficas da Unesp. Dados fornecidos pelo autor(a).

UNIVERSIDADE ESTADUAL PAULISTA "JÚLIO DE MESQUITA FILHO"

Instituto de Geociências e Ciências Exatas
Câmpus de Rio Claro

Daniel Borin

Hurst Exponent: An Indicator of Weak Chaos

Tese de doutorado apresentada ao Instituto de Geociências e Ciências Exatas, Câmpus de Rio Claro, da Universidade Estadual Paulista "Júlio de Mesquita Filho", como parte dos requisitos para a obtenção do título de Doutor em Física.

Comissão Examinadora

Prof. Dr. Edson Denis Leonel (Orientador)
IGCE / UNESP / Rio Claro (SP), Brasil

Prof. Dr. Iberê Luiz Caldas
IF / USP / São Paulo (SP), Brasil

Prof. Dr. Everton Santos Medeiros
IGCE / UNESP / Rio Claro (SP), Brasil

Prof. Dr. Roberto Venergeroles Nascimento
UFABC / Santo André (SP), Brasil

Prof. Dr. Marcelo Lobato Martins
UFV / Viçosa (MG), Brasil

Conceito: **Aprovado.**

Rio Claro (SP), 10 de novembro de 2026.

This Thesis is dedicated to my parents

ANTONIO VALDECI BORIN
and
EVA APARECIDA RIBEIRO BORIN

You are everything to me.

e aos neurônios que primeiro sucumbiram
às frias exigências do doutorado, dedico,
como saudosa lembrança, esta tese.

Acknowledgements

First of all, I would like to thank everyone who, in some way, helped me reach this point or contributed to the completion of this work. In particular, I would like to express my gratitude to:

- My parents, Antonio Valdeci Borin and Eva Aparecida Ribeiro Borin, without whom I would not have come this far, nor would I have been able to write this thesis. You are my foundation, supporting me through all of life's difficulties. There are no words to describe how grateful I am to you.
- To Leticia, for being the person with whom I shared my dreams, goals, and frustrations during the final years of my PhD, standing by my side through both achievements and challenges. Thank you for everything you taught me during this time, and for agreeing to come to Grand Forks with me and share that experience by my side.
- To the "double Matheus", Matheus Hansen Francisco and Matheus Rolim Sales, my own Morpheus figures. You offered me the red pill and showed me what the true academic world is like, with all its challenges and rewards. Your guidance and shared insights helped me grow in ways I could not have imagined, and for that I am deeply grateful.
- Professor Edson Denis Leonel, for his words of encouragement and patience.
- My former advisor, Professor Dr. Marta Cilene Gadotti, who became more than a mentor, a friend. I also thank Professor Dr. Daniel Augusto Turolla Vanzella, my advisor during my Master's degree, who, despite the difficulties of supervision during the pandemic, never abandoned me and always placed his trust in me and in my potential.
- I cannot forget to thank Professor Dr. Diego Fregolent Mendes de Oliveira for graciously hosting me during my doctoral period in the United States, whose generosity and hospitality were remarkable, and whose exchanges of ideas during this time left a lasting mark on my academic development. I am also deeply grateful to him for giving me the opportunity to live in Grand Forks, one of the best cities I have ever known, where I created memories that I will carry for all my life.
- This study was financed, in part, by the São Paulo Research Foundation (FAPESP), Brasil. Process Numbers #22/03612-6 and #24/06749-8. The opinions, hypotheses, conclusions, or recommendations expressed in this material are the responsibility of the author(s) and do not necessarily reflect the views of FAPESP.

People just don't understand how
obsessed I am with winning.

Kobe Bryant / Neymar Jr.

Abstract

The coexistence of regular and chaotic regions in Hamiltonian phase space gives rise to weak chaos, a dynamical regime characterized by slow decay of correlations and anomalous transport. A common mechanism underlying weak chaos in such systems is stickiness, whereby chaotic orbits become intermittently trapped near stability islands, behaving almost regularly for long but finite times before escaping.

Traditional chaos indicators, such as the Lyapunov exponent, converge slowly in the presence of stickiness and require knowledge of the equations of motion. In this thesis, we propose the Hurst exponent as an alternative indicator to characterize weak chaos. Originally developed in hydrology to quantify long-term dependence in time series, the Hurst exponent is computed solely from the orbit's data, requiring no underlying dynamical equations.

We apply this method to three paradigmatic area-preserving maps: the standard map, the bouncer model, and the kicked Harper map. We show that the Hurst exponent clearly distinguishes regular, weakly chaotic, and strongly chaotic motion. Moreover, a finite-time analysis reveals multimodal distributions of the finite-time Hurst exponent, where each peak corresponds to a distinct hierarchical level of the islands-around-islands structure, a feature not captured by finite-time Lyapunov exponents.

We extend the analysis to fractional dynamical systems, specifically the Riemann-Liouville fractional standard map, which exhibits cascade of bifurcations type trajectories (CBTT), a distinctive behavior in which a single trajectory undergoes a sequence of bifurcations as it evolves in time, alternating between different dynamical regimes. The Hurst exponent successfully identifies transitions between strongly chaotic, weakly chaotic, and periodic-like regimes along a single trajectory, again producing multimodal distributions.

The results establish the Hurst exponent as a practical, robust, and computationally efficient tool for detecting weak chaos and dynamical traps.

Keywords: Hurst exponent; weak chaos; stickiness; Hamiltonian systems; fractional maps; dynamical traps; finite-time analysis.

Resumo

A coexistência de regiões regulares e caóticas no espaço de fase de sistemas Hamiltonianos dá origem ao caos fraco, um regime dinâmico caracterizado por um decaimento lento de correlações e transporte anômalo. Um mecanismo comum que está na base do caos fraco nesses sistemas é o *stickiness*, pelo qual órbitas caóticas ficam intermitentemente aprisionadas próximas a ilhas de estabilidade, comportando-se de forma quase regular por longos, porém finitos, intervalos de tempo antes de escapar.

Indicadores tradicionais de caos, como o expoente de Lyapunov, convergem lentamente na presença de *stickiness* e requerem conhecimento das equações de movimento. Nesta tese, propomos o expoente de Hurst como um indicador alternativo para caracterizar o caos fraco. Originalmente desenvolvido na hidrologia para quantificar dependência de longo prazo em séries temporais, o expoente de Hurst é calculado unicamente a partir dos dados da órbita, não exigindo as equações dinâmicas subjacentes.

Aplicamos o método a três mapas preservadores de área paradigmáticos: o mapa padrão, o modelo *bouncer* e o mapa *kicked Harper*. Mostramos que o expoente de Hurst distingue claramente movimento regular, caos fraco e caos forte. Além disso, uma análise de tempo finito revela distribuições multimodais do expoente de Hurst de tempo finito, onde cada pico corresponde a um nível hierárquico distinto da estrutura de ilhas em torno de ilhas, característica não capturada por expoentes de Lyapunov de tempo finito.

Estendemos a análise a sistemas fracionários, em particular o mapa padrão fracionário de Riemann-Liouville, que exibe trajetórias do tipo cascata de bifurcações (CBTT), um comportamento peculiar no qual uma única trajetória sofre uma sequência de bifurcações ao longo de sua evolução temporal, alternando entre diferentes regimes dinâmicos. O expoente de Hurst identifica com sucesso transições entre regimes fortemente caótico, fracamente caótico e quase periódico ao longo de uma única trajetória, novamente produzindo distribuições multimodais.

Os resultados estabelecem o expoente de Hurst como uma ferramenta prática, robusta e computacionalmente eficiente para detectar caos fraco e armadilhas dinâmicas.

Palavras-chave: Expoente de Hurst; caos fraco; stickiness; sistemas Hamiltonianos; mapas fracionários; armadilhas dinâmicas; análise de tempo finito.

Table of Contents

Page

1 Introduction 12

2 Hamiltonian Systems in a Nutshell 16

2.1 Hamiltonian Formalism 17

2.2 Integrable Systems 21

2.3 Rational and Irrational Tori 24

2.4 Quasi-Integrable Systems 25

2.5 KAM Theorem 29

2.6 Fixed Points 32

2.6.1 Fixed Points and Periodic Orbits 32

2.6.2 Stability of Fixed Points 36

2.6.3 The Hartman–Grobman Theorem 37

2.7 Poincaré Section 39

2.7.1 The Twist Map 41

2.7.2 The Perturbed Twist Map 43

2.8 Poincaré–Birkhoff Theorem 44

2.9 Invariant Manifolds 49

2.9.1 Homoclinic and heteroclinic intersections 51

2.9.2 Synthesis: The structure of the perturbed phase space 54

3 Characterizing Chaos 56
3.1 Defining chaos 57
3.2 Quantifying chaos: Lyapunov exponents 59
3.2.1 One-dimensional maps 60
3.2.2 Higher-dimensional maps 61
3.3 Some chaotic discrete-time models 65
3.3.1 Standard Map 66
3.3.2 The Bouncer Model 73
3.3.3 Kicked Harper Model 84
4 Hurst Exponent: A New Indicator of Chaos 90
4.1 Historical Origins 91
4.2 The method 95
4.3 Hamiltonian Systems 96
4.4 Fractional Dynamics 106
4.4.1 The Riemann-Liouville fractional standard map and CBTT 107
4.4.2 Quantifying the CBTT 110
5 Conclusion 116
Appendix A - Published Papers 118
References 131
Index 145

CHAPTER 1

Introduction

Chaos and order have fascinated thinkers for centuries. The philosopher George Santayana (1863–1925) wrote that "chaos is the name given to any order that produces confusion in our minds," and psychiatrist Carl Jung (1875–1961) believed that "in all disorder there is a secret order." These thoughts about human nature were voiced after Jules Henri Poincaré (1854–1912) had already developed the first theoretical work on chaotic dynamics, but well before Edward Norton Lorenz (1917–2008) performed his famous numerical simulation. Taken together, they hint that a seemingly patternless evolution in time can emerge from order, namely from a system obeying clear and precise rules. In fact, chaos is one of the dynamical behaviors that deterministic equations can generate.

For a long time the physical world was viewed through the lens of Newton's deterministic principle. The mathematician Pierre-Simon Laplace (1749–1827) captured the spirit of the age in his book *Essai philosophique sur les probabilités* (A philosophical essay on probabilities) (1812) [104]:

> We may regard the present state of the universe as the effect of its past and the cause of its future. An intellect that at a certain moment would know all forces that set nature in motion, and all positions of all items of which nature is composed, if this intellect were also vast enough to submit these data to analysis, it would embrace in a single formula the movements of the greatest bodies of the universe and those of the tiniest atom; for such an intellect nothing would be uncertain and the future just like the past would be present before its eyes.

For Laplace, knowing all forces and all positions of things at one instant, could predict the

entire future of the universe with perfect certainty. In that picture, determinism and predictability were the same thing.

This view was first seriously challenged near the end of the 19th century, when Henri Poincaré set out to answer a seemingly simple question: is the solar system stable? In 1887, to mark his sixtieth birthday, King Oscar II of Sweden and Norway sponsored a mathematical competition with a money prize for settling this very question. While studying the problem, Poincaré submitted in May 1888 a nearly three-hundred-page manuscript titled Sur le problème des trois corps et les équations de la dynamique ("On the Problem of the Three Bodies and the Equations of Dynamics") [164], in which he developed several new theorems, and he was awarded the prize in 1889. Poincaré studied the gravitational interaction of just three bodies and demonstrated that, for most starting conditions, no exact mathematical solution exists [165]. More importantly, he showed that tiny differences in the initial state can cause trajectories to diverge wildly. A system governed by precise, deterministic equations could thus behave in a way that was unpredictable in practice. This sensitive dependence on initial conditions is the heart of deterministic chaos.

The source of this unpredictability lies in the impossibility of knowing the exact value of the initial conditions. If one could measure the positions and velocities of particles with infinite precision, one would indeed know the future state of any system with certainty. In practice, however, both measuring instruments and numerical simulations carry an unavoidable uncertainty (the finite precision of the device or the limited number of digits in the simulation), and this uncertainty causes nearby trajectories to diverge extremely fast.

What, then, is chaos? In a scientific sense and few words, chaos occurs in a deterministic system when the motion is bounded, never exactly repeats, and depends sensitively on the starting state. The historian Henry Adams captured the dual nature of the phenomenon when he wrote that "chaos often breeds life, when order breeds habit." [31] This remark points to the fact that chaotic motion is not merely random noise; it can coexist with order and even generate complex structures.

After Poincaré's breakthrough, researchers asked how a perfectly orderly system, in which all motions are strictly periodic or quasiperiodic, could give way to chaos, or more precisely: given an integrable Hamiltonian system, how strong must a perturbation be to destroy integrability? This question began to be answered only in the mid-20th century, when Andrey Nikolaevich Kolmogorov (1903–1987) showed that most quasiperiodic solutions (the non-resonant tori) survive

small perturbations [99]; only the resonant tori and their immediate neighbourhood are destroyed. Nearly a decade later, Jürgen Kurt Moser (1928–1999) gave a rigorous proof of Kolmogorov's conjecture for discrete area-preserving maps of an annulus [149], and Kolmogorov's student Vladimir Igorevich Arnold (1937–2010) proved the conjecture for analytic Hamiltonian systems [7][1]. This result became known as the Kolmogorov–Arnold–Moser (KAM) theorem, which is often regarded as the most important contribution to classical mechanics of the 20th century.

In this sense the result tells us that most of the regular quasiperiodic orbits survive when the system is only weakly perturbed. These surviving orbits form distorted "tori" that act like invisible walls in the abstract space of all possible motions. Because of these barriers, a chaotic trajectory cannot move freely throughout the phase space; it is confined to regions between the tori. A chaotic orbit trapped outside a KAM torus cannot cross into a regular island, and an initially regular orbit can never escape into the chaotic sea.

As the perturbation grows stronger, many tori break apart and leave behind ghost-like remnants called cantori [132–133]. A cantorus is a fractured torus: it still blocks most motions, but contains tiny gaps. A chaotic orbit may wander through one of those gaps and become temporarily trapped in the region inside. While trapped, the orbit behaves almost like a regular, quasiperiodic one, only to escape again after a long time. This phenomenon is known as stickiness [93]. It causes the system to alternate between long intervals of seemingly calm, regular behavior and sudden bursts of chaotic wandering.

The stickiness was first noted by Contopoulos [39] in the context of celestial mechanics and has profound consequences. In a fully chaotic system the influence of the initial state (i.e., temporal correlations) decays very quickly (exponentially) [83, 215], and the system has poor memory of its past. However, when stickiness is present, correlations between past and future states decay much more slowly, causing a slower algebraic decay of temporal correlations instead of an exponential decay, and affecting the recurrence-time statistics as well [37, 70, 208]. The transport of orbits through the available space becomes anomalous [89, 127, 142, 221, 224] . For these reasons, a system that exhibits stickiness is called weakly chaotic. It is not fully ordered, yet it is also very far from a completely featureless, strongly chaotic sea. Distinguishing weak chaos from strong chaos is a delicate problem, but it is crucial for understanding long-term dynamics in areas like plasma physics [158, 178].

[1] A function f is said to be analytic, if it is C^∞ and equals its Taylor series expansion around any point in its domain of definition.

This thesis proposes to use the Hurst exponent to characterize weak chaos. Originally developed by Harold Hurst (1880–1978), who spent 62 years of his life in Egypt, mostly working on projects involving the design of reservoirs along the Nile River [50, 190], the Hurst exponent is a single number that measures how strongly the past of a time series influences its future, that is, the degree of long-range dependence in the data. Because stickiness introduces long-lasting memory into the dynamics, the statistical properties of a weakly chaotic orbit differ from those of a strongly chaotic one. By measuring the Hurst exponent of orbits in Hamiltonian systems with mixed phase space, this work provides a simple quantitative tool that distinguishes weak chaos from strong chaos.

CHAPTER

2 Hamiltonian Systems in a Nutshell

The fundamental concepts of what we now call Hamiltonian dynamics emerged in the first half of the nineteenth century, through the pioneering works of William Hamilton (1805–1865) and Carl Jacobi (1804–1851) [150]. In the span of just four years, the foundations of the field were laid by two papers Hamilton published in the *Philosophical Transactions of the Royal Society of London* in 1834 and 1835 [76–77], a communication Jacobi presented to the academies of Paris and Berlin in 1836 [90], and an article Jacobi published in *Crelle's Journal* in 1837 [91]. Hamiltonian dynamics provides a powerful framework for describing the evolution of physical systems. Its central object, the Hamiltonian function, encodes all the information necessary to determine the time evolution of the system via a set of first-order differential equations.

This chapter introduces the essential concepts and mathematical tools needed to analyse the behavior of Hamiltonian systems. We begin by introducing the foundations of dynamical systems and the specific structure of Hamiltonian flows, including canonical transformations and the Hamilton–Jacobi method. The simplest possible behavior is found in *integrable* systems, for which the motion is completely regular and confined to invariant tori in phase space. However, integrability is extremely fragile: it takes only a tiny perturbation to destroy some of these tori and trigger a transition to chaotic motion.

The central part of the chapter is devoted to the consequences of breaking integrability. We first classify tori into rational and irrational ones according to the commensurability of their frequencies. The celebrated KAM theorem then tells us that *sufficiently irrational* tori survive small perturbations, while rational tori are generically destroyed. To understand what replaces them, we develop the necessary machinery: the linearisation and stability of fixed points,

the construction of Poincaré maps as a dimension-reducing bridge between flows and discrete dynamics, and the concept of the twist map. This leads us to the Poincaré–Birkhoff theorem, which reveals that the remnants of a rational torus consist of alternating chains of elliptic and hyperbolic fixed points. The hyperbolic points are particularly important because their stable and unstable invariant manifolds, when they intersect transversely, form a homoclinic tangle of extraordinary complexity, the geometric signature of deterministic chaos, as later formalised by Smale's horseshoe construction.

2.1 Dynamical Systems and Hamiltonian Formalism

A dynamical system is a mathematical framework that governs the time evolution of a system [155]. Such a description may take several forms; the most common are those employing differential equations for continuous time and difference equations for discrete time. Mathematical modelling of time-varying systems is ubiquitous across the natural sciences, engineering, and economics [3, 48, 189].

According to Alligood, Sauer, and Yorke [3], a dynamical system consists of a set of possible states together with a rule that determines the present state from the preceding one. Hence, for a deterministic system that contains no randomness, the current state is uniquely fixed by the initial condition.

In general, dynamical systems can be expressed as [155]

$$\frac{d\mathbf{x}}{dt} = f(\mathbf{x}(t)), \tag{2.1}$$

when the time variable is continuous, or as

$$\mathbf{x}_{n+1} = f(\mathbf{x}_n), \tag{2.2}$$

when time is discrete.. Here, $\mathbf{x} \in \mathbb{R}^N$ is an N-dimensional state vector that defines the phase space of the system, and $f : \mathbb{R}^N \to \mathbb{R}^N$ is a vector field (for flows) or a mapping (for discrete systems) that encodes the underlying dynamical rules.The system described by Eq. (2.1) is commonly called a flow, where the state $\mathbf{x}(t)$ is uniquely determined for all $t \geq 0$ given an initial condition $\mathbf{x}(0)$. In contrast, the system in Eq. (2.2) is referred to as a map, where the discrete time steps are called iterates, and the state $\mathbf{x}_n$ at any iterate n is uniquely determined by the initial state $\mathbf{x}_0$.

Within the broad class of dynamical systems, Hamiltonian systems form a well-established subclass. In a Hamiltonian system, the entire dynamics is captured by a single scalar function $\mathcal{H}$,

known as the Hamiltonian, which depends on the system variables. Examples of phenomena described by the Hamiltonian formalism include mechanical problems where friction or any energy loss can be neglected, the behavior of magnetic field lines in plasmas, celestial mechanics and the stability of the solar system, and advection and transport in fluids, among many others [155, 203, 222]. The Hamiltonian formalism combines concepts from differential equations with variational principles [131].

For a classical Hamiltonian system with N degrees of freedom, the state is specified by a generalized coordinate vector $\mathbf{q} = (q_1, q_2, \ldots, q_N)$ and a generalized momentum vector $\mathbf{p} = (p_1, p_2, \ldots, p_N)$. Its dynamics is completely described by the Hamiltonian function $\mathcal{H}(\mathbf{p}, \mathbf{q}, t)$, where t denotes time. The time evolution is given by Hamilton's equations:

$$\begin{aligned} \frac{dq_i}{dt} &= \frac{\partial \mathcal{H}(\mathbf{p}, \mathbf{q}, t)}{\partial p_i}, \\ \frac{dp_i}{dt} &= -\frac{\partial \mathcal{H}(\mathbf{p}, \mathbf{q}, t)}{\partial q_i}, \end{aligned} \tag{2.3}$$

with $i = 1, 2, \ldots, N$. The solution of Eq. (2.3) yields the trajectory $(\mathbf{p}(t), \mathbf{q}(t))$ in the $2N$-dimensional phase space spanned by $\mathbf{q}$ and $\mathbf{p}$. Any set of variables $(\mathbf{p}, \mathbf{q})$ whose evolution obeys a system of equations of the form Eq. (2.3) is said to be *canonical*, and p_i and q_i are conjugate variables.

The Hamiltonian can also be obtained through a Legendre transform of the Lagrangian, which itself is defined by [116]

$$\mathcal{L}(\dot{\mathbf{q}}, \mathbf{q}, t) = T(\dot{\mathbf{q}}, \mathbf{q}) - U(\mathbf{q}, t), \tag{2.4}$$

where $\dot{\mathbf{q}}$ and $\mathbf{q}$ are the vectors of generalized velocities and positions, respectively. The function T represents the kinetic energy, while U is the potential energy of the system. The Hamiltonian then follows as

$$\mathcal{H}(\mathbf{p}, \mathbf{q}, t) \equiv \sum_i \dot{q}_i p_i - \mathcal{L}(\dot{\mathbf{q}}, \mathbf{q}, t), \tag{2.4}$$

with the momenta given by

$$p_i \equiv \frac{\partial \mathcal{L}}{\partial \dot{q}_i}. \tag{2.5}$$

While the Lagrangian formalism of mechanics is naturally set in the configuration space of the generalized coordinates $\mathbf{q}$, the Hamiltonian formalism is framed in the *phase space*. For a system with N degrees of freedom, the phase space is a $2N$-dimensional space whose axes are the generalized coordinates q_i and the conjugate momenta p_i. At any instant t, the state of the system is completely specified by a single point $(\mathbf{p}(t), \mathbf{q}(t))$ in this space, called the *representative point*.

As time progresses, this point traces out a trajectory governed by Hamilton's equations[Eq. (2.3)]. Under suitable smoothness assumptions on the right-hand sides of Hamilton's equations, the theorem of existence and uniqueness for ordinary differential equations [19, 28–29, 38, 81, 166] guarantees that through each point of phase space passes one and only one trajectory . A crucial consequence is that distinct trajectories can never intersect; if they did, a point of intersection would have two possible futures, violating uniqueness [189]. Phase space thus furnishes an extremely powerful geometric language for Hamiltonian dynamics, enabling qualitative analyses of the motion, for instance, distinguishing between open and closed trajectories.

For time-independent generalized coordinates and conservative forces, the Hamiltonian coincides with the total energy of the system and can be written as $\mathcal{H} = T + U$ [69]. When $\mathcal{H}$ has no explicit time dependence, the system is called autonomous. In that case one can readily show that $\mathcal{H}(\mathbf{p}(t), \mathbf{q}(t))$ remains constant throughout the evolution [131, 155]. Using Hamilton's equations,

$$\frac{d\mathcal{H}}{dt} = \sum_i \left(\frac{\partial \mathcal{H}}{\partial q_i} \frac{dq_i}{dt} + \frac{\partial \mathcal{H}}{\partial p_i} \frac{dp_i}{dt} \right) = \sum_i \left(\frac{\partial \mathcal{H}}{\partial q_i} \frac{\partial \mathcal{H}}{\partial p_i} - \frac{\partial \mathcal{H}}{\partial p_i} \frac{\partial \mathcal{H}}{\partial q_i} \right) = 0. \tag{2.6}$$

Thus, identifying $\mathcal{H}$ with the system's energy E, autonomous Hamiltonian systems conserve energy.

With the help of Hamilton's equations [Eq. (2.3)], we can compute the total time derivative of an arbitrary function $f = f(\mathbf{p}, \mathbf{q}, t)$:

$$\begin{aligned} \frac{df(\mathbf{p},\mathbf{q},t)}{dt} &= \sum_i \left(\frac{\partial f}{\partial q_i} \frac{dq_i}{dt} + \frac{\partial f}{\partial p_i} \frac{dp_i}{dt} \right) + \frac{\partial f}{\partial t} \\ &= \sum_i \left(\frac{\partial f}{\partial q_i} \frac{\partial \mathcal{H}}{\partial p_i} - \frac{\partial f}{\partial p_i} \frac{\partial \mathcal{H}}{\partial q_i} \right) + \frac{\partial f}{\partial t} \\ &= [f, \mathcal{H}] + \frac{\partial f}{\partial t}. \end{aligned} \tag{2.7}$$

The above expression provides a criterion for identifying quantities that remain unchanged during the time evolution of a Hamiltonian system. Such quantities are known as *constants of motion* and play a central role in the analysis of dynamical systems [116, 155].

Definition 2.1.1 — Constant of Motion. A function $f(\mathbf{p}, \mathbf{q}, t)$ is called a *constant of motion* if its total time derivative vanishes,

$$\frac{df}{dt} = 0.$$

According to Eq. (2.7), this condition is equivalent to

$$[f,\mathcal{H}]+\frac{\partial f}{\partial t}=0.$$

In particular, if f has no explicit time dependence ($\partial f/\partial t=0$), then f is a constant of motion if and only if

$$[f,\mathcal{H}]=0.$$

For conservative systems, the Hamiltonian itself has no explicit time dependence and satisfies $[\mathcal{H},\mathcal{H}]=0$. Therefore,

$$\frac{d\mathcal{H}}{dt}=0,$$

showing that the total energy is a constant of motion

One notable advantage of the Hamiltonian formalism is that it replaces the N second-order ordinary differential equations encountered in Newtonian and Lagrangian mechanics with a set of $2N$ first-order ordinary differential equations.

Although this reduction in order is conceptually appealing, solving Hamilton's equations directly can still be a difficult task. It is often possible, however, to perform a change of variables that renders the equations of motion much simpler. In general, an arbitrary change of variables alters the form of Hamilton's equations. The transformations that preserve their canonical form are of particular importance in Hamiltonian mechanics and are known as *canonical transformations*.

Definition 2.1.2 — Canonical Transformation. A transformation from the canonical variables $(\mathbf{q},\mathbf{p})$ to a new set of variables $(\mathbf{Q},\mathbf{P})$ is called a *canonical transformation* if it preserves the form of Hamilton's equations. That is, the transformed variables satisfy

$$\dot{Q}_i=\frac{\partial\mathcal{K}}{\partial P_i},\qquad \dot{P}_i=-\frac{\partial\mathcal{K}}{\partial Q_i},$$

where $\mathcal{K}(\mathbf{Q},\mathbf{P},t)$ is the Hamiltonian expressed in the new variables (also known as the *Kamiltonian*).

A systematic way to generate such transformations is through scalar functions that depend on a mixture of old and new coordinates. The four standard types are

$$F_1(\mathbf{q},\mathbf{Q},t),\quad F_2(\mathbf{q},\mathbf{P},t),\quad F_3(\mathbf{p},\mathbf{Q},t),\quad F_4(\mathbf{p},\mathbf{P},t),$$

where $(\mathbf{Q},\mathbf{P})$ denotes the new set of canonical variables. Focusing on the generating function

$S(\mathbf{q},\mathbf{P},t) \coloneqq F_2(\mathbf{q},\mathbf{P},t)$, the transformation equations take the form

$$p_i = \frac{\partial S}{\partial q_i}, \qquad Q_i = \frac{\partial S}{\partial P_i}, \qquad \mathcal{K}(\mathbf{P},\mathbf{Q},t) = \mathcal{H}(\mathbf{p},\mathbf{q},t) + \frac{\partial S}{\partial t}. \tag{2.8}$$

These relations open a formal route to solve the equations of motion. If we choose a generating function that makes the new Hamiltonian vanish identically, $\mathcal{K} \equiv 0$, then the new coordinates are constants; they are simply the initial values of the original variables. Substituting the first relation of Eq. (2.8) into the last, with $\mathcal{K} = 0$, leads to a partial differential equation for S:

$$\mathcal{H}\left(\frac{\partial S}{\partial \mathbf{q}}, \mathbf{q}, t\right) + \frac{\partial S}{\partial t} = 0. \tag{2.9}$$

Eq. (2.9) is the time-dependent *Hamilton–Jacobi equation*, and its solution S is known as *Hamilton's principal function*.

For autonomous systems, where $\mathcal{H}$ does not depend explicitly on time, it is sufficient to require that the new Hamiltonian be a constant, $\mathcal{K} \equiv E$ (the conserved energy). Then Eq. (2.8) yields the time-independent Hamilton–Jacobi equation

$$\mathcal{H}\left(\frac{\partial S}{\partial \mathbf{q}}, \mathbf{q}\right) = E, \tag{2.10}$$

and S in this context is called *Hamilton's characteristic function*. Thus, through canonical transformations and the Hamilton–Jacobi formulation, one obtains a powerful alternative method for determining the trajectories of a Hamiltonian system.

2.2 Integrable Systems

As discussed in the previous section, for autonomous conservative systems the Hamiltonian equals the total energy and constitutes a constant of motion. More generally, any function $f(\mathbf{p},\mathbf{q})$ of the canonical variables that Poisson-commutes with the Hamiltonian, $[f,\mathcal{H}] = 0$, and has no explicit time dependence is also a constant of motion. Such conserved quantities play a fundamental role in determining whether a Hamiltonian system is integrable.

Definition 2.2.1 Two functions $f_1(\mathbf{p},\mathbf{q})$ and $f_2(\mathbf{p},\mathbf{q})$ are said to be *in involution* if their Poisson bracket vanishes identically,

$$[f_1, f_2] = 0. \tag{2.11}$$

A set of functions is said to be in involution if this condition holds for every pair of functions in the set.

The importance of this property for Hamiltonian systems is established by the Liouville theorem on integrable systems, which states that the existence of a sufficient number of independent first integrals in involution allows the system to be integrated by quadratures.

Theorem 2.2.1 — Liouville-Arnold. Consider a Hamiltonian system with N degrees of freedom, defined on a $2N$-dimensional symplectic manifold, and suppose that it possesses N first integrals $f_1, \ldots, f_N$ in involution,

$$[f_i, f_j] = 0, \qquad i, j = 1, \ldots, N. \tag{2.12}$$

Consider a common level set of these functions,

$$M_{\mathbf{c}} = \{(\mathbf{p}, \mathbf{q}) : f_i(\mathbf{p}, \mathbf{q}) = c_i, \quad i = 1, \ldots, N\}. \tag{2.13}$$

Assume that the differentials $df_1, \ldots, df_N$ are linearly independent at every point of $M_{\mathbf{c}}$. Then:

1. $M_{\mathbf{c}}$ is a smooth N-dimensional invariant manifold under the Hamiltonian flow generated by $\mathcal{H} = f_1$.
2. If $M_{\mathbf{c}}$ is compact and connected, it is diffeomorphic to an N-dimensional torus, T^N.
3. The motion on this torus is conditionally periodic. In suitable angular coordinates $\theta = (\theta_1, \ldots, \theta_N)$, the equations of motion take the form

$$\dot{\theta}_i = \omega_i(\mathbf{c}), \qquad i = 1, \ldots, N, \tag{2.14}$$

   where the frequencies ω_i depend on the values of the first integrals.
4. The Hamiltonian system can be integrated by quadratures.

For a proof and further details, see Ref. [8]. Based on the definition of involution and the Liouville-Arnold theorem, the conditions for Liouville integrability can be summarized as follows:

Property 2.1 — Integrability. An autonomous Hamiltonian system with N degrees of freedom is integrable in the Liouville sense if it possesses N functionally independent

constants of motion $f_i(\mathbf{p},\mathbf{q})$, $i = 1,\ldots,N$, that mutually Poisson-commute,

$$[f_i, f_j] = 0, \qquad \text{for all } i, j. \tag{2.15}$$

Consider an autonomous integrable Hamiltonian system. One can introduce a canonical transformation such that the new Hamiltonian $\mathcal{K}$ depends only on the new momentum vector $\mathbf{P}$, i.e., $\mathcal{K} = \mathcal{K}(\mathbf{P})$ and $\partial\mathcal{K}/\partial Q_i = 0$ for all i. This is achieved by choosing the components of $\mathbf{P}$ to be the N constants of motion, $P_i = f_i(\mathbf{p},\mathbf{q})$. Because the f_i are conserved,

$$\frac{dP_i}{dt} = \frac{df_i}{dt} = -\frac{\partial\mathcal{K}}{\partial Q_i} = 0, \tag{2.16}$$

confirming that $\mathcal{K}$ is independent of the new coordinates. Any functionally independent set of functions of the N constants can serve as the new momenta. A particularly convenient choice leads to *action–angle variables*, denoted by $(\mathbf{I},\boldsymbol{\theta})$, where the action $\mathbf{I}$ is defined as

$$I_i = \frac{1}{2\pi}\oint_{C_i} \mathbf{p}\cdot d\mathbf{q}, \qquad i = 1,2,\ldots,N, \tag{2.17}$$

and the C_i are independent closed paths on the N-torus. The canonically conjugate variable $\boldsymbol{\theta}$ is angle-like: completing a circuit along the closed path C_i around the torus advances θ_i by 2π, while all other θ_j return to their original values.

This canonical transformation is generated by

$$S(\mathbf{I},\mathbf{q}) = \int_{\mathbf{q}_0}^{\mathbf{q}} \mathbf{p}(\mathbf{I},\mathbf{q}')\cdot d\mathbf{q}', \tag{2.18}$$

through the relations

$$\theta_i = \frac{\partial S(\mathbf{I},\mathbf{q})}{\partial I_i}, \qquad p_i = \frac{\partial S(\mathbf{I},\mathbf{q})}{\partial q_i}. \tag{2.19}$$

The torus is determined by the constants of motion, i.e., by the initial conditions. By construction the new Hamiltonian depends only on the actions, $\mathcal{K} = \mathcal{K}(\mathbf{I})$, and the equations of motion become

$$\frac{dI_i}{dt} = -\frac{\partial\mathcal{K}(\mathbf{I})}{\partial\theta_i} = 0, \qquad \frac{d\theta_i}{dt} = \frac{\partial\mathcal{K}(\mathbf{I})}{\partial I_i} = \omega_i(\mathbf{I}). \tag{2.20}$$

These integrate immediately to

$$I_i(t) = \text{const}, \tag{2.21a}$$

$$\theta_i(t) = \theta_i(0) + \omega_i(\mathbf{I})\,t, \tag{2.21b}$$

where the frequencies ω_i are constant along each trajectory and each θ_i is a 2π-periodic function.

In summary, integrable Hamiltonian systems display highly regular dynamics: every trajectory is confined to an invariant N-dimensional torus, and the motion in the angle variables

is linear in time. The character of this motion depends on the frequency ratios. When the frequencies are rationally dependent, the trajectory closes on itself (a rational torus); when they are incommensurate, the orbit fills the torus densely (an irrational torus). The next section discusses the consequences of these two possibilities in detail.

2.3 Rational and Irrational Tori

For an integrable Hamiltonian system with N degrees of freedom, the trajectories are confined to N-dimensional tori. The constant actions $\mathbf{I}$ fix the radii of these tori, while the angle variables $\boldsymbol{\theta}$ are cyclic coordinates. The frequencies

$$\omega_i(\mathbf{I}) = \frac{\partial \mathcal{K}(\mathbf{I})}{\partial I_i}, \qquad i = 1, \ldots, N, \tag{2.22}$$

are the components of the frequency vector $\boldsymbol{\omega}(\mathbf{I})$, which governs the flow on a given torus. Depending on the values of these frequencies, the motion can be either periodic or quasi-periodic.

Definition 2.3.1 A trajectory on an N-torus is said to be *periodic* if there exists a non-zero integer vector $\mathbf{m} = (m_1, m_2, \ldots, m_N)$ such that

$$\mathbf{m} \cdot \boldsymbol{\omega} = 0. \tag{2.23}$$

Eq. (2.23) is the *resonance condition*. When it holds, the orbit closes after completing m_1 circuits in the θ_1 direction, m_2 circuits in θ_2, and so on.

In the two-degree-of-freedom case ($N = 2$), the resonance condition reduces to $m_1\omega_1 + m_2\omega_2 = 0$, or equivalently

$$\frac{\omega_1}{\omega_2} = -\frac{m_2}{m_1}. \tag{2.24}$$

Since m_1 and m_2 are integers, the frequency ratio is a rational number. In general, when there exist coprime integers m_1 and m_2 such that $m_1\omega_1 = m_2\omega_2$, the two frequencies are called *commensurate* and the motion is periodic.

Definition 2.3.2 A torus is called *rational* (or resonant) if there exists a nonzero integer vector $\mathbf{m}$ satisfying the resonance condition Eq. (2.23). Equivalently, its fundamental frequencies are commensurate. If no such integer vector exists, the frequencies are *incommensurate*; the torus is then called *irrational* (or non-resonant).

On an irrational torus, a single trajectory winds around indefinitely, filling the torus densely

as $t \to \infty$. In a Poincaré surface of section, the intersection of an irrational torus appears as a closed, continuous circle.

For an autonomous integrable Hamiltonian system with two degrees of freedom, the four-dimensional phase space foliates into invariant two-dimensional tori. Each trajectory carries two frequencies, ω_1 and ω_2, corresponding to the independent circuits C_1 and C_2 on the torus.

Definition 2.3.3 The *rotation number* (or *winding number*) of a trajectory is the ratio

$$\nu = \frac{\omega_1}{\omega_2}, \tag{2.25}$$

which measures the average number of revolutions in the θ_1 angle for each revolution in the θ_2 angle. It provides a direct criterion for classifying the dynamics: if $\nu = r/s$ with $r, s \in \mathbb{Z}$ (a rational number), the trajectory is periodic and lies on a rational torus; otherwise, ν is irrational and the motion is quasi-periodic on an irrational torus.

The distinction between rational and irrational tori is not merely a formal classification; it lies at the heart of understanding what happens when an integrable system is subjected to a small perturbation. As will be examined in the next section on quasi-integrable systems, and ultimately in the context of the Kolmogorov–Arnold–Moser (KAM) theorem, sufficiently irrational tori survive under weak perturbations, while rational tori are generally destroyed, giving rise to intricate structures in phase space.

2.4 Quasi-Integrable Systems

In the previous section we saw that for integrable systems a canonical transformation to action–angle variables yields a trivial solution: the actions are constant and the angles evolve linearly in time. Such a transformation, however, exists only when the system possesses N independent integrals of motion in involution, and integrable Hamiltonians with more than one degree of freedom[1] are exceedingly rare. A natural question then arises: what happens to the dynamics when an integrable Hamiltonian is slightly perturbed? In other words, how robust is integrability under a small change of the Hamiltonian?

A natural expectation is that any perturbation destroys all constants of motion except the energy. However, for sufficiently weak perturbations, not all invariant tori are destroyed; many

[1] A degree of freedom is an independent coordinate needed to specify the configuration of a dynamical system. In Hamiltonian mechanics, each degree of freedom corresponds to a canonical coordinate–momentum pair (q_i, p_i).

survive, although they become slightly deformed. This behavior is described by the celebrated work of Kolmogorov (1954) [99], Arnold (1963) [7], and Moser (1962) [149], collectively known as the KAM theorem.

A standard framework to study quasi-integrable systems consists of a perturbed Hamiltonian written as the sum of an integrable part $\mathcal{H}_0$ and a perturbation $\varepsilon\mathcal{H}_1$,

$$\mathcal{H}(\mathbf{p},\mathbf{q}) = \mathcal{H}_0(\mathbf{p},\mathbf{q}) + \varepsilon\mathcal{H}_1(\mathbf{p},\mathbf{q}), \tag{2.26}$$

where $\varepsilon \ll 1$ measures the perturbation strength. Expressing the unperturbed system in action–angle variables $(\mathbf{I},\boldsymbol{\theta})$, the Hamiltonian becomes

$$\mathcal{H}(\mathbf{I},\boldsymbol{\theta}) = \mathcal{H}_0(\mathbf{I}) + \varepsilon\mathcal{H}_1(\mathbf{I},\boldsymbol{\theta}), \tag{2.27}$$

with the unperturbed frequencies

$$\omega_i(\mathbf{I}) = \frac{\partial \mathcal{H}_0}{\partial I_i}, \qquad i = 1,\dots,N. \tag{2.28}$$

For $\varepsilon = 0$, the motion is simply

$$I_i = \text{const}, \qquad \theta_i(t) = \theta_i(0) + \omega_i(\mathbf{I})\,t. \tag{2.29}$$

Our goal is to find a canonical transformation $(\mathbf{I},\boldsymbol{\theta}) \to (\mathbf{J},\boldsymbol{\psi})$ that renders the new Hamiltonian $\mathcal{K}$ a function of the new actions $\mathbf{J}$ alone, eliminating all dependence on the new angles ψ. We seek a generating function $S(\mathbf{J},\boldsymbol{\theta})$ of type two, from which the transformation follows as

$$I_i = \frac{\partial S}{\partial \theta_i}, \qquad \psi_i = \frac{\partial S}{\partial J_i}. \tag{2.30}$$

The Hamilton–Jacobi equation for S is, using Eq. (2.27),

$$\mathcal{H}\left(\frac{\partial S}{\partial \boldsymbol{\theta}}, \boldsymbol{\theta}\right) = \mathcal{K}(\mathbf{J}), \qquad \text{i.e.,} \qquad \mathcal{H}_0\left(\frac{\partial S}{\partial \boldsymbol{\theta}}\right) + \varepsilon\mathcal{H}_1\left(\frac{\partial S}{\partial \boldsymbol{\theta}}, \boldsymbol{\theta}\right) = \mathcal{K}(\mathbf{J}). \tag{2.31}$$

Because the perturbation is small, it is natural to expand the generating function around the identity transformation,

$$S(\mathbf{J},\boldsymbol{\theta}) = S_0(\mathbf{J},\boldsymbol{\theta}) + \varepsilon S_1(\mathbf{J},\boldsymbol{\theta}) + \mathcal{O}(\varepsilon^2), \tag{2.32}$$

with the zeroth-order term chosen to generate the identity $(\mathbf{I} = \mathbf{J}, \boldsymbol{\psi} = \boldsymbol{\theta})$, i.e.,

$$S_0(\mathbf{J},\boldsymbol{\theta}) = \mathbf{J}\cdot\boldsymbol{\theta}. \tag{2.33}$$

Substituting Eq. (2.32) into Eq. (2.30) gives, to first order,

$$\mathbf{I} = \mathbf{J} + \varepsilon \frac{\partial S_1}{\partial \boldsymbol{\theta}} + \mathcal{O}(\varepsilon^2), \qquad \boldsymbol{\psi} = \boldsymbol{\theta} + \varepsilon \frac{\partial S_1}{\partial \mathbf{J}} + \mathcal{O}(\varepsilon^2). \tag{2.34}$$

Now insert $\mathbf{I}$ into the left-hand side of Eq. (2.31) and expand consistently to first order in ε:

$$\begin{aligned} \mathcal{K}(\mathbf{J},\boldsymbol{\theta}) &= \mathcal{H}_0\left(\mathbf{J} + \varepsilon \frac{\partial S_1}{\partial \boldsymbol{\theta}}\right) + \varepsilon \mathcal{H}_1(\mathbf{J},\boldsymbol{\theta}) + \mathcal{O}(\varepsilon^2) \\ &= \mathcal{H}_0(\mathbf{J}) + \varepsilon \sum_{k=1}^{N} \frac{\partial \mathcal{H}_0}{\partial J_k} \frac{\partial S_1}{\partial \theta_k} + \varepsilon \mathcal{H}_1(\mathbf{J},\boldsymbol{\theta}) + \mathcal{O}(\varepsilon^2) \\ &= \underbrace{\mathcal{H}_0(\mathbf{J})}_{\mathcal{K}_0(\mathbf{J})} + \underbrace{\varepsilon \left[\boldsymbol{\omega}(\mathbf{J}) \cdot \frac{\partial S_1}{\partial \boldsymbol{\theta}} + \mathcal{K}_1(\mathbf{J},\boldsymbol{\theta}) \right]}_{\mathcal{K}_1(\mathbf{J},\boldsymbol{\theta})} + \mathcal{O}(\varepsilon^2), \end{aligned} \tag{2.35}$$

where $\boldsymbol{\omega}(\mathbf{J}) = \partial \mathcal{H}_0 / \partial \mathbf{J}$ is the unperturbed frequency vector.

We now demand that the first-order term in Eq. (2.35) be independent of $\boldsymbol{\theta}$, i.e., $\mathcal{K}_1(\mathbf{J},\boldsymbol{\theta}) = \mathcal{K}_1(\mathbf{J})$. To achieve this, we expand both $\mathcal{H}_1$ and S_1 in multiple Fourier series in the old angles $\boldsymbol{\theta}$:

$$\mathcal{H}_1(\mathbf{J},\boldsymbol{\theta}) = \sum_{\mathbf{m}} \mathcal{H}_{1,\mathbf{m}}(\mathbf{J})\, e^{i\mathbf{m}\cdot\boldsymbol{\theta}}, \tag{2.36a}$$

$$S_1(\mathbf{J},\boldsymbol{\theta}) = \sum_{\mathbf{m}} S_{1,\mathbf{m}}(\mathbf{J})\, e^{i\mathbf{m}\cdot\boldsymbol{\theta}}, \tag{2.36b}$$

where the sum runs over all integer vectors $\mathbf{m} \in \mathbb{Z}^N$. Inserting these expansions into the $\mathcal{O}(\varepsilon)$ part of Eq. (2.35) yields

$$\mathcal{K}_1(\mathbf{J},\boldsymbol{\theta}) = \sum_{\mathbf{m}} \Big[i\mathbf{m}\cdot\boldsymbol{\omega}(\mathbf{J})\, S_{1,\mathbf{m}}(\mathbf{J}) + \mathcal{H}_{1,\mathbf{m}}(\mathbf{J}) \Big] e^{i\mathbf{m}\cdot\boldsymbol{\theta}}. \tag{2.37}$$

We must now distinguish between resonant and non-resonant tori of the unperturbed system. From Definition 2.3.2, a torus characterized by the action $\mathbf{J}$ is *resonant* (rational) if there exists a non-zero integer vector $\mathbf{m}$ for which $\mathbf{m}\cdot\boldsymbol{\omega}(\mathbf{J}) = 0$; otherwise it is *non-resonant* (irrational). In this section we restrict attention to non-resonant tori. For such tori, we can choose the Fourier coefficients of S_1 as

$$S_{1,\mathbf{m}}(\mathbf{J}) = \begin{cases} i\dfrac{\mathcal{H}_{1,\mathbf{m}}(\mathbf{J})}{\mathbf{m}\cdot\boldsymbol{\omega}(\mathbf{J})}, & \mathbf{m} \neq \mathbf{0}, \\[2ex] 0, & \mathbf{m} = \mathbf{0}, \end{cases} \tag{2.38}$$

which cancels every $\boldsymbol{\theta}$-dependent term in Eq. (2.37). Only the $\mathbf{m} = \mathbf{0}$ component survives, giving the angle-independent first-order Hamiltonian

$$\mathcal{K}_1(\mathbf{J}) = \mathcal{H}_{1,\mathbf{0}}(\mathbf{J}) = \frac{1}{(2\pi)^N} \int_0^{2\pi} \cdots \int_0^{2\pi} \mathcal{H}_1(\mathbf{J},\boldsymbol{\theta})\, d\theta_1 \cdots d\theta_N \equiv \langle \mathcal{H}_1 \rangle(\mathbf{J}). \tag{2.39}$$

Notice that Eq. (2.39) establishes a fundamental result of the averaging principle: isolating the secular part of the Hamiltonian (the $\mathbf{m} = \mathbf{0}$ Fourier coefficient) is strictly equivalent to averaging the perturbation $\mathcal{H}_1$ over the entire angular domain.

Thus, to first order in ε, the new Hamiltonian and the generating function are

$$\mathcal{K}(\mathbf{J}) = \mathcal{H}_0(\mathbf{J}) + \varepsilon\langle\mathcal{H}_1\rangle(\mathbf{J}) + \mathcal{O}(\varepsilon^2), \tag{2.40a}$$

$$S(\mathbf{J},\boldsymbol{\theta}) = \mathbf{J}\cdot\boldsymbol{\theta} + i\varepsilon\sum_{\mathbf{m}\neq\mathbf{0}} \frac{\mathcal{H}_{1,\mathbf{m}}(\mathbf{J})}{\mathbf{m}\cdot\boldsymbol{\omega}(\mathbf{J})}\, e^{i\mathbf{m}\cdot\boldsymbol{\theta}} + \mathcal{O}(\varepsilon^2), \tag{2.40b}$$

which formally solves the problem at first order.

At this point we face the notorious *problem of small denominators*, a difficulty already recognized by Poincaré in his pioneering work on the N-body problem [164]. The situation is even more subtle than it first appears: even when the frequencies are incommensurate, so that $\mathbf{m}\cdot\boldsymbol{\omega} \neq 0$ for all non-zero integer vectors $\mathbf{m}$, one can always find a sequence of integers m_j that makes $\mathbf{m}\cdot\boldsymbol{\omega}$ arbitrarily small [14]. Because the perturbative series involves terms with arbitrarily large $|\mathbf{m}|$, small denominators are virtually inevitable, casting serious doubt on whether the series can converge at all, even away from exact resonances. This difficulty has historically been a central obstacle in celestial mechanics, where perturbation theory is a primary analytical technique.

Fortunately, in many celestial mechanics settings the unperturbed frequencies are sufficiently far from low-order commensurabilities that $\mathbf{m}\cdot\boldsymbol{\omega}$ becomes small only for large values of $|\mathbf{m}|$. For such large $|\mathbf{m}|$, the Fourier coefficients $\mathcal{H}_{1,\mathbf{m}}$ generally decay rapidly, often exponentially, because the perturbation is a smooth function. Partial sums of the series can therefore be used with good accuracy over long, although not infinite, times. A classic example of incommensurability is the Earth's orbital motion, whose frequency is roughly 11.86198... times that of Jupiter, its principal perturber [14]. On the other hand, notable low-order resonances do exist: the orbital periods of Neptune and Pluto are locked in a $2:3$ ratio [211], and Saturn's satellites Titan and Hyperion exhibit a $3:4$ commensurability [15].

These considerations underscore the fragile nature of integrability under perturbation. While rational tori are generally destroyed, a large set of "sufficiently irrational" tori can survive if the frequency vector satisfies stringent arithmetic conditions. The precise formulation of these conditions and the proof that such tori persist form the content of the celebrated KAM theorem, which we discuss in the next section.

2.5 KAM Theorem

A fundamentally novel approach to the small-denominator problem was developed by Kolmogorov, Arnold, and Moser, leading to what is now known as the KAM theorem. The key insight is to replace the slowly converging perturbative series of the form Eq. (2.40a) with a rapidly converging sequence of successive approximations, namely a Newton-type iteration, that guarantees the existence of invariant tori for infinite times. As mentioned in the Introduction, Kolmogorov first formulated the conjecture [99], which was later proved by Arnold [7] for Hamiltonian systems, and by Moser [149] for twist maps. Following the notation of Arnold, the theorem can be stated as follows.

Theorem 2.5.1 — KAM. Consider an integrable Hamiltonian $\mathcal{H}_0(\mathbf{I})$ with N degrees of freedom and a sufficiently smooth perturbation $\varepsilon\mathcal{H}_1(\mathbf{I},\theta)$. Non-resonant tori of the unperturbed system are not destroyed by a sufficiently small perturbation; they are merely deformed. The surviving tori are those satisfying the following conditions:

1. **Linear independence of frequencies:** the frequency vector $\omega(\mathbf{I}) = \partial\mathcal{H}_0/\partial\mathbf{I}$ satisfies
$$\mathbf{m}\cdot\omega(\mathbf{I}) \neq 0, \tag{2.41}$$
for every non-zero integer vector $\mathbf{m}\in\mathbb{Z}^N$.
2. **Non-degeneracy (Kolmogorov condition):** the unperturbed Hamiltonian $\mathcal{H}_0$ is non-degenerate, meaning the Hessian matrix of $\mathcal{H}_0$ with respect to the actions is non-singular:
$$\det\left(\frac{\partial^2\mathcal{H}_0}{\partial\mathbf{I}\partial\mathbf{I}}\right) = \det\left(\frac{\partial\omega}{\partial\mathbf{I}}\right) \neq 0. \tag{2.42}$$
3. **Smoothness of the perturbation:** $\mathcal{H}_1$ possesses a sufficient number M of continuous derivatives. (Lichtenberg [116] notes that $M > 3$ is always sufficient, while $M = 2$ is conjectured to be necessary.)
4. **Diophantine condition:** the initial action $\mathbf{I}$ must be sufficiently far from resonances, i.e., there exists a constant $\kappa(\varepsilon) > 0$, independent of $\mathbf{m}$ and vanishing as $\varepsilon\to 0$, such that
$$|\mathbf{m}\cdot\omega(\mathbf{I})| \geq \frac{\kappa(\varepsilon)}{|\mathbf{m}|^{N+1}} \tag{2.43}$$
for all non-zero $\mathbf{m}$, where $|\mathbf{m}| = \sum_i |m_i|$.

The invariant tori that meet all three criteria are called *KAM tori*. Condition Eq. (2.43)

cannot be satisfied if κ is too large; since κ grows with the perturbation strength ε, the KAM theorem requires ε to be sufficiently small. Originally the theorem required an extremely weak perturbation ($\varepsilon \sim 10^{-48}$), but modern formulations admit much larger values. [193]

For systems with $N = 2$ degrees of freedom, the rotation number $\nu = \omega_1/\omega_2$ is commonly used. The Diophantine condition [Eq. (2.43)] then takes the equivalent form

$$\left|\nu - \frac{r}{s}\right| > \frac{\kappa(\varepsilon)}{s^{5/2}}, \tag{2.44}$$

for all integers r, s ($s > 0$). This inequality expresses the tori that survive are those whose rotation number cannot be well approximated by rational numbers; they are *sufficiently irrational*. The last KAM torus to be destroyed as ε increases is the one with the "most irrational" rotation number.

A convenient way to characterize the degree of irrationality of a real number is through its continued fraction expansion [96]. Let γ be an irrational number. It can be uniquely expressed as

$$\gamma = a_0 + \cfrac{1}{a_1 + \cfrac{1}{a_2 + \cfrac{1}{a_3 + \cdots}}} \equiv [a_0; a_1, a_2, a_3, \ldots], \tag{2.45}$$

where the coefficients a_i are positive integers. Some classic examples are

$$\begin{aligned}
\pi &= [3; 7, 15, 1, 292, 1, 1, 1, 2, \ldots], \\
\sqrt{2} &= [1; 2, 2, 2, 2, 2, 2, 2, \ldots], \\
\sqrt{3} &= [1; 1, 2, 1, 2, 1, 2, 1, \ldots], \\
e &= [2; 1, 2, 1, 1, 4, 1, 1, 6, \ldots].
\end{aligned}$$

Truncating the continued fraction at a finite order n yields the rational approximant

$$\alpha_n = \frac{r_n}{s_n} = [a_0; a_1, a_2, \ldots, a_n], \tag{2.46}$$

which gives the best possible rational approximation to γ in the sense that no rational r/s with $s \leq s_n$ lies closer to γ than r_n/s_n. The sequence $\{\alpha_n\}$ converges to γ, and satisfies an error bound [96].

$$\left|\gamma - \frac{r_n}{s_n}\right| < \frac{1}{s_n s_{n+1}}. \tag{2.47}$$

For instance, the successive approximants of π are

$$\alpha_0 = 3, \quad \alpha_1 = \frac{22}{7} \approx 3.1429, \quad \alpha_2 = \frac{333}{106} \approx 3.14151, \quad \alpha_3 = \frac{355}{113} \approx 3.1415929,$$

which converge much faster than decimal approximations; the error for a decimal fraction is of order $1/s$, while for continued fractions it is of order $1/s^2$, cf. Eq. (2.47).

The speed of convergence of α_n to γ is dictated by how quickly the sequence $\{a_n\}$ diverges. The slowest possible convergence, and therefore the "worst approximated" irrational, occurs when all a_n equal 1. This is the golden mean (also known as golden number or golden ratio),

$$\varphi = \frac{1+\sqrt{5}}{2} = 1.618033989\cdots = [1;1,1,1,\ldots]. \tag{2.48}$$

In this precise sense, φ is the most irrational number.

An important question is whether the set of surviving irrational tori has a significant measure for weak perturbations. The answer is affirmative, as can be illustrated by a simple argument. Assume $0 \leq \nu \leq 1$. For each rational r/s in this interval, we remove an interval of width $\kappa(\varepsilon)/s^{5/2}$ centred at r/s; these correspond to the rational tori destroyed by the perturbation. Figure 2.1 shows some of these subintervals, for a given value of $K(\varepsilon)$, belonging to the interval [0,1]. The total length of the removed intervals is bounded above by

$$L(\varepsilon) = \sum_{s=1}^{\infty} s \cdot \frac{\kappa(\varepsilon)}{s^{5/2}} = \kappa(\varepsilon) \sum_{s=1}^{\infty} \frac{1}{s^{3/2}} = \kappa(\varepsilon)\, \zeta\left(\tfrac{3}{2}\right) \approx 2.612\, \kappa(\varepsilon), \tag{2.49}$$

where ζ is the Riemann zeta function. (This is an overestimate because many of the removed intervals overlap.) Since $\kappa(\varepsilon) \to 0$ as $\varepsilon \to 0$, the total measure of destroyed tori vanishes in the integrable limit. For a small but finite $\varepsilon \ll 1$, $L(\varepsilon)$ is small, so the complement $1 - L(\varepsilon)$, corresponding to the set of surviving irrational tori, remains large. Thus, most irrational tori persist under a weak perturbation, although they are slightly deformed.

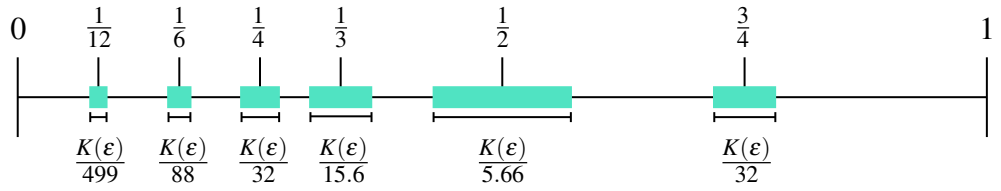


Figure 2.1 – Deleted intervals of width $K(\varepsilon)/s^{5/2}$ centered at rational points r/s in the unit interval.
Source: By the author

Besides the smallness of ε, the KAM theorem also requires a *non-degeneracy condition* on the unperturbed Hamiltonian. The integrable part $\mathcal{H}_0(\mathbf{I})$ must be genuinely nonlinear, i.e., the frequency map $\mathbf{I} \mapsto \omega(\mathbf{I})$ must have a non-vanishing Jacobian:

$$\det\left[\frac{\partial^2 \mathcal{H}_0}{\partial I_j \partial I_k}\right] = \det\left[\frac{\partial \omega_j}{\partial I_k}\right] \neq 0 \tag{2.50}$$

everywhere in phase space. If, for example, one frequency is constant (linear oscillations), the determinant vanishes and the KAM theorem does not apply. This condition guarantees that the rotation number changes monotonically across the energy surfaces.

The proof of the KAM theorem is beyond the scope of this text (the interested reader may consult Refs. [213]). A more accessible exposition can be found in Lichtenberg [116]. The central technical idea is to replace the slowly convergent perturbative series with a super-convergent Newton iteration: each step uses the current approximation as the basis for the next, thereby accelerating convergence.

To summarise, KAM theory teaches us that non-resonant tori with a sufficiently irrational rotation number preserve their topology and are only slightly deformed under a small perturbation. On the other hand, the theorem does not apply to resonant tori and their immediate neighbourhood. To begin understanding the fate of these destroyed tori, we must first introduce the fundamental concepts of linearisation and stability of fixed points, as well as the construction of Poincaré maps, which form the subject of the next sections.

2.6 Linearization and Stability of Fixed Points

To analyze a nonlinear dynamical system, whether governed by a map or a differential equation, the first step is to identify its fixed points (equilibria) and examine the local behavior of orbits in their vicinity. Under suitable conditions, the qualitative dynamics near such points is described by an associated linear system. This section focuses on recurrence maps but presents the parallel concepts for continuous-time flows.

2.6.1 Fixed Points and Periodic Orbits

Let $f : U \subseteq \mathbb{R}^n \to \mathbb{R}^n$ be a map. The iterates of f are defined by

$$f^{t+1} = f \circ f^t, \qquad f^1 = f, \qquad f^0 = \mathrm{id}_U,$$

where $\mathrm{id}_U : U \to U$ denotes the identity map, defined by $\mathrm{id}_U(x) = x$ for all $x \in U$, and $t \in \mathbb{N}_0$. If f is a diffeomorphism[2], negative iterates are defined and the notation extends to $t \in \mathbb{Z}$.

[2] In the mathematical literature, diffeomorphisms are often preferred; Smale [185] points to "its natural beauty" and the fact that "problems in the qualitative theory of differential equations are present in their simplest form in the theory of diffeomorphisms."

Definition 2.6.1 Let $U \subseteq \mathbb{R}^n$ be an open set and let $f : U \to \mathbb{R}^m$. The function f is said to be of class C^k if all its partial derivatives up to order k exist and are continuous on U. In particular, a C^0 function is continuous, a C^1 function is continuously differentiable, and a C^∞ function has continuous derivatives of every order and is called *smooth*.

Definition 2.6.2 Let U and V be open subsets of $\mathbb{R}^n$. A function

$$f : U \to V$$

is called a C^k *diffeomorphism* if it is a bijection and both f and its inverse f^{-1} are C^k functions. If both f and f^{-1} are C^0, then f is called a *homeomorphism*. A C^1 diffeomorphism is often referred to simply as a *diffeomorphism* when no ambiguity arises.

Definition 2.6.3 Given a point $x \in U \subseteq \mathbb{R}^n$, the *forward orbit* (or simply the orbit or trajectory) of f through x is the set $\{ f^t(x) \mid t \in \mathbb{N}_0 \}$, ordered by increasing t. If f is invertible, the *backward orbit* is $\{ f^{-t}(x) \mid t \in \mathbb{N}_0 \}$ and the *(whole) orbit* is $\{ f^t(x) \mid t \in \mathbb{Z} \}$.

Definition 2.6.4 A point $x^* \in U$ is a *fixed point* (or equilibrium point) if $f(x^*) = x^*$. Its orbit consists of the point itself. A point x^* is *periodic* if $f^\tau(x^*) = x^*$ for some non-zero integer τ. The smallest such positive τ is the *period* T, and the set $\{ f^t(x^*) \mid t = 0, 1, \ldots, T-1 \}$ is a *periodic orbit* (a T-cycle).

Maps that are related by a homeomorphism preserving orbits are called conjugate.

Definition 2.6.5 — Conjugacy of maps. Two maps $f, g : U \subseteq \mathbb{R}^n \to \mathbb{R}^n$ are *topologically conjugate* if there exists a homeomorphism h such that

$$h \circ f = g \circ h \qquad \text{or} \qquad h \circ f \circ h^{-1} = g.$$

Conjugacy implies $h \circ f^t \circ h^{-1} = g^t$ for all $t \in \mathbb{N}$, so h maps orbits of f onto orbits of g. In particular, if x^* is a periodic point of f of period T, then $h(x^*)$ is a periodic point of g of the same period.

A classic illustration is the conjugacy between the logistic map $f_4(x) = 4x(1-x)$ and the

tent map T_2 on $[0,1]$, defined by

$$T_2(x) = \begin{cases} 2x, & 0 \le x < 1/2, \\ 2-2x, & 1/2 \le x \le 1. \end{cases}$$

The homeomorphism $h(x) = \sin^2(\frac{\pi}{2}x)$ provides the conjugacy, since it is continuous, bijective, with continuous inverse, and satisfies $f_4 \circ h = h \circ T_2$:

$$(f_4 \circ h)(x) = 4\sin^2\left(\tfrac{\pi}{2}x\right)\left(1-\sin^2\left(\tfrac{\pi}{2}x\right)\right) = \sin^2(\pi x) = (h \circ T_2)(x).$$

In the continuous-time case, the dynamics of a system is governed by a vector field $X : U \subseteq \mathbb{R}^n \to \mathbb{R}^n$, where U denotes the phase space. The evolution of the state $x(t) \in U$ is described by the ordinary differential equation

$$\dot{x} = X(x), \tag{2.51}$$

which specifies the instantaneous rate of change of the state at every point of the phase space.

Assuming that the vector field X is at least of class C^1, the existence and uniqueness theorem for ordinary differential equations guarantees that, for every initial condition $x_0 \in U$, there exists a unique solution $x(t;x_0)$ of Eq. (2.51). Therefore, for each time t, one can define the map

$$\phi_t : U \to U, \qquad \phi_t(x_0) = x(t;x_0),$$

which associates each initial condition with the corresponding state of the system at time t. The family of maps $\{\phi_t\}_{t\in\mathbb{R}}$ is called the *flow* generated by the vector field X.

Definition 2.6.6 — Flow. The family of maps $\{\phi_t\}_{t\in\mathbb{R}}$ generated by Eq. (2.51) is called the *flow* of the vector field X. The flow satisfies the composition law

$$\phi_{t+s} = \phi_t \circ \phi_s, \tag{2.52}$$

for all admissible times t and s, with $\phi_0 = \mathrm{id}$. Whenever the trajectories exist for both positive and negative times, each map ϕ_t is invertible and

$$\phi_t^{-1} = \phi_{-t}.$$

Furthermore, the vector field is recovered from the flow through

$$X(x) = \frac{d}{dt}\phi_t(x)\bigg|_{t=0}, \tag{2.53}$$

showing that the flow is completely generated by the vector field.

Geometrically, the flow describes the evolution of every point in the phase space under the action of the vector field. Rather than following a single trajectory, the flow provides a global description of the dynamics, mapping every initial condition to its position at a later (or earlier) time.

Definition 2.6.7 — Equilibrium point. A point $x^* \in U$ is called an *equilibrium point* if

$$X(x^*) = 0.$$

Since the vector field vanishes at x^*, the corresponding trajectory remains constant, that is,

$$\phi_t(x^*) = x^*, \qquad \forall t.$$

Then, its orbit is just the point itself.

Just as for maps, we can compare flows that have the same qualitative behavior through the notion of conjugacy.

Definition 2.6.8 — Conjugacy of flows. Two flows $\phi_t : U \to U$ and $\psi_t : W \to W$ are *topologically conjugate* if there exists a homeomorphism $h : U \to W$ such that

$$h \circ \phi_t = \psi_t \circ h \qquad \text{for all } t \in \mathbb{R}.$$

In other words, the diagram

$$\begin{array}{ccc} U & \xrightarrow{\phi_t} & U \\ {\scriptstyle h}\downarrow & & \downarrow{\scriptstyle h} \\ W & \xrightarrow{\psi_t} & W \end{array}$$

commutes. Conjugacy of flows is an equivalence relation and captures the idea that the two flows have identical topological dynamics: h takes orbits of ϕ_t onto orbits of ψ_t, preserving their time parametrisation. If h is a C^1 diffeomorphism, we can differentiate the conjugacy relation at $t = 0$ to obtain a link between the vector fields:

$$Dh(\phi_t(x))\frac{d}{dt}\phi_t(x)\bigg|_{t=0} = \frac{d}{dt}\psi_t(h(x))\bigg|_{t=0},$$

and, taking into account Eq. (2.53), we obtain

$$Dh(x)X(x) = Y(h(x)).$$

That is, if h is a differentiable flow conjugacy between the flows ϕ_t and ψ_t, then the derivative $Dh(x)$ transforms $X(x)$ into $Y(h(x))$.

2.6.2 Stability of Fixed Points

One of the central questions in the study of dynamical systems is how the long-term behavior of trajectories changes under small perturbations of the initial condition. In particular, given a fixed point of the dynamics, it is natural to ask whether trajectories starting sufficiently close to it remain nearby or eventually converge to it. These questions motivate the notions of Lyapunov and asymptotic stability, which characterize the local behavior of orbits in the vicinity of equilibrium states. Stability concepts for maps are introduced first.

Definition 2.6.9 A fixed point x^* of $x_{t+1} = f(x_t)$ is *Lyapunov stable* if, for every $\varepsilon > 0$, there exists $\delta > 0$ such that $\|x - x^*\| < \delta$ implies $\|f^t(x) - x^*\| < \varepsilon$ for all $t > 0$. It is *asymptotically stable* if it is Lyapunov stable and there exists $\delta > 0$ such that $\lim_{t\to\infty} f^t(x) = x^*$ whenever $\|x - x^*\| < \delta$. Fixed points that are not stable are *unstable*.

Thus, near a Lyapunov stable fixed point iterates stay close; near an asymptotically stable one they converge to it. Since a T-periodic point x^* is a fixed point of f^T, its stability is determined by the sequence $\{f^{kT}(x)\}_{k\in\mathbb{N}}$ for x close to the orbit.

The convergence of orbits can often be analysed through the contraction mapping principle.

Definition 2.6.10 Let (S,d) be a metric space. A map $f : S \to S$ is *contracting* if there exists a constant $\lambda \in (0,1)$ such that

$$d(f(x), f(y)) \leq \lambda\, d(x,y) \quad \text{for all } x, y \in S.$$

Theorem 2.6.1 — Contraction Mapping Theorem. Let $f : S \to S$ be a contracting map on a complete metric space S. Then f possesses a unique fixed point $x^* \in S$, and for every $x \in S$ the sequence of iterates converges to x^* exponentially:

$$d(f^t(x), x^*) \leq \frac{\lambda^t}{1-\lambda}\, d(f(x), x).$$

The proof can be found in [17]. A direct consequence is that if a linear map A has all

eigenvalues of modulus strictly smaller than one, then A is contracting and every orbit converges to the origin exponentially fast. For flows, the definitions of stability are analogous.

Definition 2.6.11 An equilibrium point x^* of $\dot{x} = X(x)$ is *Lyapunov stable* if, for every $\varepsilon > 0$, there exists $\delta > 0$ such that $\|x_0 - x^*\| < \delta$ implies $\|\phi_t(x_0) - x^*\| < \varepsilon$ for all $t \geq 0$. It is *asymptotically stable* if it is Lyapunov stable and $\lim_{t\to\infty} \phi_t(x_0) = x^*$ for all x_0 in a neighbourhood of x^*.

2.6.3 The Hartman–Grobman Theorem

To investigate stability, introduce the deviation vector $\delta\mathbf{x} = \mathbf{x} - \mathbf{x}^*$, assumed to be sufficiently small. Substituting into the map or flow and Taylor expanding around x^* gives the linearised equations

$$\delta\mathbf{x}_{t+1} = Df(\mathbf{x}^*)\,\delta\mathbf{x}_t + \mathcal{O}(\|\delta\mathbf{x}\|^2), \tag{2.54}$$

$$\delta\dot{\mathbf{x}} = DX(\mathbf{x}^*)\,\delta\mathbf{x} + \mathcal{O}(\|\delta\mathbf{x}\|^2), \tag{2.55}$$

where Df and DX denote the Jacobian matrices. The zero solution of the linear systems $\delta\mathbf{x}_{t+1} = Df(\mathbf{x}^*)\delta\mathbf{x}_t$ and $\delta\dot{\mathbf{x}} = DX(\mathbf{x}^*)\delta\mathbf{x}$ often determines the local stability of the original nonlinear system when the fixed point is hyperbolic. The notion of hyperbolicity is defined as follows:

Definition 2.6.12 — Hyperbolic fixed point for maps. A fixed point x^* of $x_{t+1} = f(x_t)$ is *hyperbolic* if no eigenvalue of the Jacobian matrix $Df(x^*)$ has modulus equal to one. The linear part of f at x^* is the map $y \mapsto Df(x^*)y$.

Definition 2.6.13 — Hyperbolic fixed point for flows. An equilibrium point x^* of $\dot{x} = X(x)$ is *hyperbolic* if all eigenvalues of $DX(x^*)$ have non-zero real part. The linear part is the vector field $y \mapsto DX(x^*)y$.

The fundamental result that justifies linear stability analysis is the Hartman–Grobman theorem [75, 80]. It states that near a hyperbolic fixed point, the nonlinear dynamics is topologically conjugate to its linear part.

Theorem 2.6.2 — Hartman–Grobman for maps. Let x^* be a hyperbolic fixed point of a C^1 diffeomorphism f. Then there exist neighbourhoods U of x^*, V of the origin, and a

homeomorphism $h : U \to V$ such that

$$h \circ f = Df(x^*) \circ h \qquad \text{on } U.$$

In words, f is topologically conjugate to its linearisation $Df(x^*)$ in a neighbourhood of x^*.

Theorem 2.6.3 — Hartman–Grobman for flows. Let x^* be a hyperbolic equilibrium point of a C^1 vector field X. Then the flow ϕ_t is topologically conjugate to the flow generated by $\dot{y} = DX(x^*)y$ near x^*.

Proofs can be found in Palis and de Melo [157]. An intuitive interpretation is that the nonlinear neighbourhood around x^* is a distorted copy of the linear neighbourhood, and the homeomorphism h guarantees that the orientation of orbits is preserved. Consequently, the stability of a hyperbolic fixed point is entirely determined by the eigenvalues of the Jacobian: if all eigenvalues of $Df(x^*)$ lie inside the unit circle for maps (or have negative real part for flows), the fixed point is asymptotically stable; if at least one lies outside the unit circle for maps (or has a positive real part for flows), it is unstable. Hyperbolic fixed points are *robust*, their qualitative behavior is unaffected by small nonlinear terms, while non-hyperbolic ones are *fragile* and their stability may change when nonlinear corrections are included.

For two-dimensional systems, the linearised dynamics is classified by the trace τ and determinant Δ of the Jacobian matrix $J = Df(x^*)$ (maps) or $J = DX(x^*)$ (flows). The eigenvalues are the roots of $\xi^2 - \tau\xi + \Delta = 0$.

A two-dimensional map $(x_n, y_n) \mapsto (x_{n+1}, y_{n+1})$ can be viewed as a coordinate transformation. The area elements at successive steps are related by

$$dx_{n+1}\, dy_{n+1} = |\det J|\, dx_n\, dy_n,$$

where $J = Df(\mathbf{x}^*)$ is the Jacobian determinant of the map. If $|\det J| = 1$, the map *preserves areas* and is called *conservative*; if $|\det J| < 1$, areas contract (dissipative map); if $|\det J| > 1$, the map is anti-dissipative (its inverse is dissipative).

For conservative two-dimensional maps ($\det J = 1$), the characteristic equation becomes $\lambda^2 - \tau\lambda + 1 = 0$, so the eigenvalues satisfy $\lambda_1\lambda_2 = 1$. Depending on the trace τ, one finds:

- $\tau^2 > 4$: real distinct eigenvalues, $\lambda_2 = \lambda_1^{-1} \Rightarrow$ *saddle*.
- $\tau^2 = 4$: real repeated eigenvalues, $\lambda = \pm 1$ (degenerate).
- $\tau^2 < 4$: complex conjugate eigenvalues on the unit circle, $|\lambda| = 1 \Rightarrow$ *elliptic point* (center).

Classification	**Linear Maps** ($x_{t+1} = Jx_t$)	**Linear Flows** ($\dot{x} = Jx$)
Stable Node	$\xi_{1,2} \in \mathbb{R}$ with $\lvert\xi_{1,2}\rvert < 1$	$\xi_{1,2} \in \mathbb{R}$ with $\xi_{1,2} < 0$
Stable Focus	$\xi_{1,2} \in \mathbb{C}$ with $\lvert\xi_{1,2}\rvert < 1$	$\xi_{1,2} = \alpha \pm i\beta$ with $\alpha < 0$
Unstable Node	$\xi_{1,2} \in \mathbb{R}$ with $\lvert\xi_{1,2}\rvert > 1$	$\xi_{1,2} \in \mathbb{R}$ with $\xi_{1,2} > 0$
Unstable Focus	$\xi_{1,2} \in \mathbb{C}$ with $\lvert\xi_{1,2}\rvert > 1$	$\xi_{1,2} = \alpha \pm i\beta$ with $\alpha > 0$
Saddle	$\xi_{1,2} \in \mathbb{R}$ with $\lvert\xi_1\rvert > 1 > \lvert\xi_2\rvert$	$\xi_{1,2} \in \mathbb{R}$ with $\xi_1 > 0 > \xi_2$
Center	$\xi_{1,2} \in \mathbb{C}$ with $\lvert\xi_{1,2}\rvert = 1$	$\xi_{1,2} = \pm i\beta$ with $\alpha = 0$

Table 2.1: Classification of local stability for two-dimensional linear systems based on eigenvalues. For continuous-time flows, $\alpha = \mathrm{Re}(\xi)$ and $\beta = \mathrm{Im}(\xi)$.

Among these cases, only the saddle is hyperbolic, since its eigenvalues lie off the unit circle; therefore, the *Hartman–Grobman theorem* applies only in this case.

The concepts of fixed points, stability, and linearisation gain their full power when applied to continuous flows through the construction of a *Poincaré map*. By choosing an appropriate cross-section of the phase space, a periodic orbit of a flow corresponds to a fixed point of the associated Poincaré map. The stability of the periodic orbit then reduces to the stability of that fixed point, which can be analysed using the linearised map. This bridge between maps and flows is the subject of the next section, where we introduce Poincaré sections and their role in reducing the dimension of the problem.

2.7 Poincaré Section

A powerful connection between flows and maps allows one to analyse a dynamical system by reducing the dimension of the phase space. Consider a three-dimensional flow $\mathbf{F}$ and a trajectory in phase space. Choose a surface of section Σ, for instance a plane $y = \text{const}$, and record the intersections of the trajectory with this plane under a prescribed orientation; for example, only when the trajectory crosses Σ from above to below (i.e., when y is decreasing). In Fig. 2.2, the points labelled $A, B, C, \ldots$ are precisely those intersections.

Because of the existence and uniqueness theorem for differential equations, the trajectory

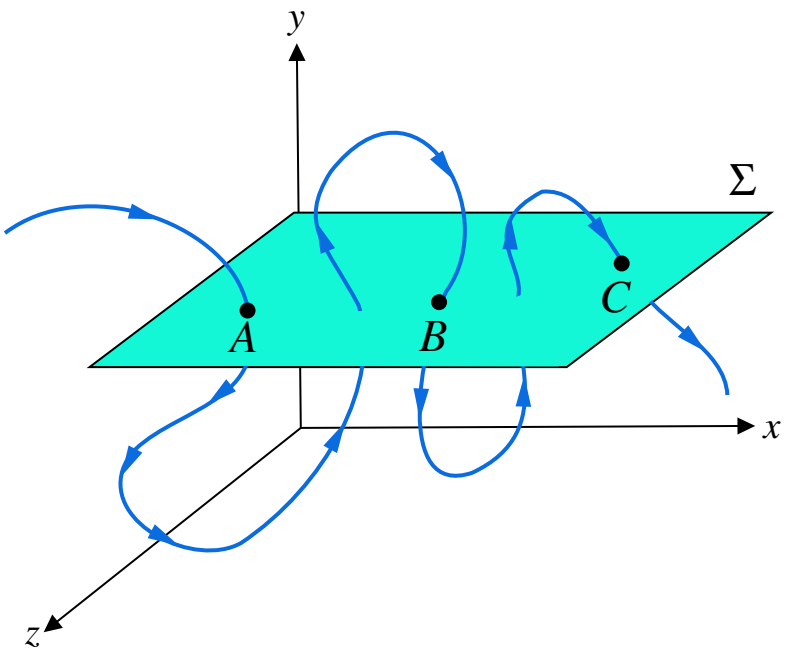


Figure 2.2 – Poincaré surface of section for a three-dimensional flow. The trajectory intersects the section Σ at the points A, B, C, defined by crossings with a prescribed orientation.
Source: By the author

through $A, B, C, \ldots$ is unique, so the coordinates of point B on Σ are single-valued functions of the coordinates of A,

$$x_B = M_x(x_A, y_A), \qquad y_B = M_y(x_A, y_A),$$

which we write symbolically as $B = \mathcal{M}(A)$. Similarly, the coordinates of C are determined by those of B,

$$C = \mathcal{M}(B) = \mathcal{M}(\mathcal{M}(A)) = \mathcal{M}^{[2]}(A),$$

and so forth. Thus $\mathcal{M}$ is a two-dimensional map for the coordinates on the surface of section Σ; it is called a *Poincaré map* of the flow $\mathbf{F}$.

A precise definition is the following.

Definition 2.7.1 Let ϕ_t be a flow on a phase space S, generated by a vector field X, and let $\Sigma \subset S$ be a subset with $\dim \Sigma = \dim S - 1$ satisfying:

1. every orbit of ϕ_t meets Σ;
2. for every $x \in \Sigma$, the vector $X(x)$ is not tangent to Σ.

Then the *Poincaré map* $P : \Sigma \to \Sigma$ is defined by

$$P(y) = \phi_{\tau(y)}(y), \tag{2.56}$$

where $y \in \Sigma$ and $\tau(y)$ is the smallest positive time for which $\phi_{\tau(y)}(y) \in \Sigma$.

In practice, one selects a specific orientation (e.g., left to right) and records successive intersections. If the n-th intersection is denoted by $(\mathbf{p}_n, \mathbf{q}_n)$, the Poincaré map relates it to the next one:

$$(\mathbf{p}_{n+1}, \mathbf{q}_{n+1}) = \mathbb{P}(\mathbf{p}_n, \mathbf{q}_n). \tag{2.57}$$

Systems with more than one degree of freedom are difficult to visualise because of their high dimensionality. The Poincaré section (or Poincaré map) represents a trajectory in the full N-dimensional phase space on an $(N-1)$-dimensional surface, making it an indispensable visualisation tool. On the Poincaré section, resonant tori with rotation number $\nu = r/s$ appear as s discrete points, while non-resonant tori appear as closed invariant curves, reflecting the quasi-periodic motion that never returns exactly to the same point on the section.

Several natural choices for the surface of section arise in practice. For a one degree of freedom Hamiltonian system with a periodic time dependence, $\mathcal{H}(p,q,t) = \mathcal{H}(p,q,t+\tau)$, one can construct the Poincaré section by recording the state $(p(t_n), q(t_n))$ at times $t_n = t_0 + n\tau$, i.e., at each multiple of the period. This variant is called a *stroboscopic map*.

Another important case is an autonomous Hamiltonian system with two degrees of freedom. The dynamics is confined to a three-dimensional energy surface $\mathcal{H}(p_1, p_2, q_1, q_2) = \mathcal{H}_0$ within the four-dimensional phase space. This equation allows one to eliminate one variable, say p_2, writing it as a function of the other three:

$$p_2 = p_2(p_1, q_1, q_2, \mathcal{H}_0). \tag{2.58}$$

If the motion is bounded, a trajectory repeatedly pierces the plane $q_2 = \text{const}$ in the three-dimensional energy manifold. The plane (p_1, q_1) is then a convenient choice for the Poincaré section.

2.7.1 The Twist Map

As seen in Section 2.2, for an integrable two degree of freedom system, the motion is described by action–angle variables $(\mathbf{I}, \theta)$:

$$I_i(t) = \text{const}, \tag{2.59a}$$

$$\theta_i(t) = \theta_i(0) + \omega_i(\mathbf{I})\, t, \tag{2.59b}$$

with frequencies $\omega_i(\mathbf{I}) = \partial \mathcal{H}_0 / \partial I_i$. The angles are 2π-periodic. For $N = 2$ and a time-independent Hamiltonian, the motion takes place on a three-dimensional energy surface, foliated by two-dimensional

invariant tori. The angles θ_1 and θ_2 correspond, respectively, to the minor and major circuits on the torus.

Choose a Poincaré surface of section Σ that cuts the torus at a fixed value of θ_2, say $\theta_2 = 0$, and record the intersections of trajectories with Σ (see Fig. 2.3). The intersection of a given torus with Σ is a circle, parametrised by the action I_1 and angle θ_1.

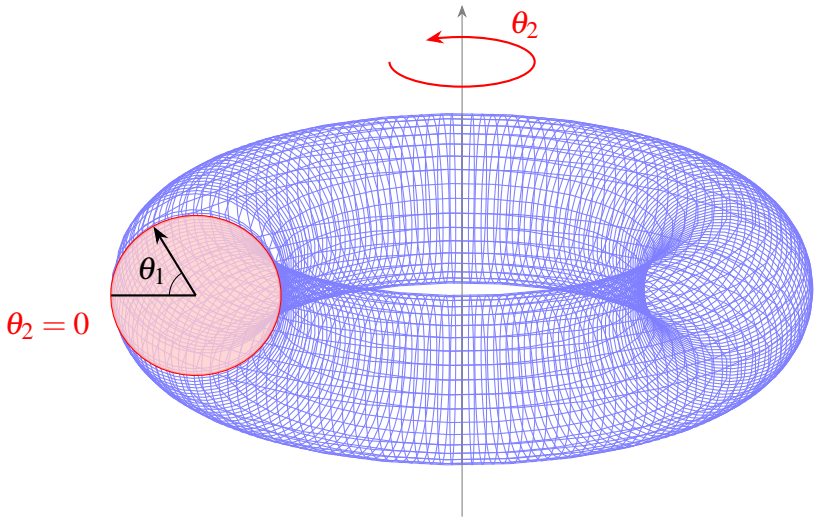


Figure 2.3 – Poincaré surface of section for an invariant two-dimensional torus in phase space. The section Σ is defined by a fixed value of the angle θ_2, and the intersections of trajectories with Σ form closed curves parametrised by (I_1, θ_1).
Source: By the author

Define discrete variables on the section as

$$I_{1,n} = I_1\big(t = n(2\pi/\omega_2)\big), \qquad \theta_{1,n} = \theta_1\big(t = n(2\pi/\omega_2)\big). \tag{2.60}$$

Since θ_2 advances linearly, a full circuit in the θ_2 direction takes time $2\pi/\omega_2$. Using the solutions in Eq. (2.59), the map relating successive intersections is

$$I_{1,n+1} = I_{1,n}, \tag{2.61}$$

$$\theta_{1,n+1} = \theta_{1,n} + 2\pi\,\alpha(I_{1,n+1}), \tag{2.62}$$

where we introduced the *rotation number* (winding number) for the torus,

$$\alpha(I_{1,n+1}) = \frac{\omega_1}{\omega_2}, \tag{2.63}$$

written here as a function of $I_{1,n+1}$ for convenience. The map defined by Eqs. (2.61)–(2.62) is called the *twist map*.

The phase-space trajectory forms a helix on the torus. Between successive intersections with the Poincaré section, the angular coordinate changes by $\Delta\theta_1 = \theta_{1,n+1} - \theta_{1,n} = 2\pi\alpha$ where α

depends on the action I_1. Since different values of I_1 define different invariant tori, the angular advance changes from one torus to another. Consequently, the helices have different pitches, which is why this property is called *twist*.

The twist map is area-preserving. Its Jacobian matrix is

$$J = \begin{pmatrix} \partial I_{1,n+1}/\partial I_{1,n} & \partial I_{1,n+1}/\partial \theta_{1,n} \\ \partial \theta_{1,n+1}/\partial I_{1,n} & \partial \theta_{1,n+1}/\partial \theta_{1,n} \end{pmatrix} = \begin{pmatrix} 1 & 0 \\ d\alpha/dI_{1,n} & 1 \end{pmatrix},$$

so $\det J = 1$. The Eqs. (2.61)-(2.62) show that trajectories flow on invariant tori, whose intersections with Σ lie on circles. Consecutive intersections are angularly separated by $2\pi\alpha$. A torus is rational if α is rational (the orbit closes after a finite number of iterations) and irrational if α is irrational (the orbit fills the circle densely).

2.7.2 The Perturbed Twist Map

According to the KAM theorem, a large fraction of irrational tori survive a small perturbation of the integrable Hamiltonian. We now examine what happens to the rational tori. For this purpose we consider a quasi-integrable Hamiltonian

$$\mathcal{H}(I_1, I_2; \theta_1, \theta_2) = \mathcal{H}_0(I_1, I_2) + \varepsilon \mathcal{H}_1(I_1, I_2; \theta_1, \theta_2), \tag{2.64}$$

with $\varepsilon \ll 1$.

On the Poincaré section Σ, the twist map is modified by the perturbation. We write the perturbed twist map in the general form

$$I_{1,n+1} = I_{1,n} + \varepsilon F(I_{1,n+1}, \theta_{1,n}), \tag{2.65}$$

$$\theta_{1,n+1} = \theta_{1,n} + 2\pi\,\alpha(I_{1,n+1}) + \varepsilon G(I_{1,n+1}, \theta_{1,n}), \tag{2.66}$$

where F and G are 2π-periodic functions of $\theta_{1,n}$. In some cases closed analytical expressions for F and G can be obtained from the perturbing Hamiltonian $\mathcal{H}_1$; more generally, they arise from the numerical integration of Hamilton's equations corresponding to Eq. (2.64).

The time evolution governed by the perturbed twist map can be viewed as a transformation between the coordinates of two successive intersections,

$$(I_{1,n}, \theta_{1,n}) \mapsto (I_{1,n+1}, \theta_{1,n+1}),$$

which preserves area. We seek a generating function of the second kind,

$$F_2(I_{1,n+1}, \theta_{1,n}) = I_{1,n+1}\theta_{1,n} + 2\pi A(I_{1,n+1}) + \varepsilon B(I_{1,n+1}, \theta_{1,n}), \tag{2.67}$$

where A describes the unperturbed twist and B accounts for the perturbation. The associated canonical transformation is

$$I_{1,n} = \frac{\partial F_2}{\partial \theta_{1,n}} = I_{1,n+1} + \varepsilon \frac{\partial B}{\partial \theta_{1,n}}, \tag{2.68}$$

$$\theta_{1,n+1} = \frac{\partial F_2}{\partial I_{1,n+1}} = \theta_{1,n} + 2\pi \frac{dA}{dI_{1,n+1}} + \varepsilon \frac{\partial B}{\partial I_{1,n+1}}. \tag{2.69}$$

Comparison of Eqs. (2.68)–(2.69) with Eqs. (2.65)–(2.66) yields

$$\alpha = \frac{dA}{dI_{1,n+1}}, \qquad F = -\frac{\partial B}{\partial \theta_{1,n}}, \qquad G = \frac{\partial B}{\partial I_{1,n+1}}. \tag{2.70}$$

Since mixed partial derivatives commute, $B_{I\theta} = B_{\theta I}$, differentiating Eq. (2.65) with respect to $I_{1,n+1}$ and Eq. (2.66) with respect to $\theta_{1,n}$, and adding the results, it follows that

$$\frac{\partial F}{\partial I_{1,n+1}} + \frac{\partial G}{\partial \theta_{1,n}} = 0. \tag{2.71}$$

Conversely, this compatibility condition ensures the local existence of a function B, so that the transformation admits the generating function Eq. (2.67). Therefore, the perturbed twist map is canonical and, consequently, area-preserving.

Having established the persistence of sufficiently irrational invariant tori, it remains to understand what happens to the complementary set of resonant tori. Their response to a perturbation is fundamentally different: instead of persisting as invariant curves, they undergo a local reorganization of the phase space into periodic orbits. This transition is described by the Poincaré–Birkhoff theorem, one of the central results in the theory of area-preserving maps.

2.8 Poincaré–Birkhoff Theorem

The Poincaré–Birkhoff theorem characterizes the local dynamics in the neighborhood of a resonant torus of a nearly integrable Hamiltonian system. It states that a rational torus with rotation number $\alpha = m_2/m_1$, where m_1 and m_2 are coprime integers, is generically replaced by an even number of periodic points under a small perturbation. More precisely, the theorem predicts the appearance of exactly m_1 elliptic and m_1 hyperbolic periodic points, alternating along the location previously occupied by the resonant torus.

A precise statement, adapted to the setting of a perturbed twist map, is the following.

Theorem 2.8.1 — Poincaré–Birkhoff. Let T_0 be the unperturbed twist map on an annulus $\mathbb{T} \times [I_-, I_+]$,

$$T_0 : \begin{cases} I_{n+1} = I_n, \\ \theta_{n+1} = \theta_n + 2\pi\,\alpha(I_{n+1}), \end{cases} \tag{2.72}$$

where the rotation function $\alpha(I)$ is strictly monotonic. Assume that for some coprime integers m_1, m_2 there exist $J_- < J_+$ such that $\alpha(I_-) < m_2/m_1 < \alpha(I_+)$. Consider a perturbed area-preserving twist map T_ε given by

$$T_\varepsilon : \begin{cases} I_{n+1} = I_n + \varepsilon\, F(I_{n+1}, \theta_n), \\ \theta_{n+1} = \theta_n + 2\pi\,\alpha(I_{n+1}) + \varepsilon\, G(I_{n+1}, \theta_n), \end{cases} \tag{2.73}$$

with F, G 2π-periodic in θ and ε sufficiently small. Then the m_1-th iterate $T_\varepsilon^{m_1}$ has at least $2m_1$ fixed points in the annular region. Generically, these fixed points appear as m_1 elliptic and m_1 hyperbolic points, alternating around the annulus.

The original theorem, formulated by Poincaré as a geometrical conjecture and proved by Birkhoff, stated that an area-preserving twist map of an annulus that rotates the inner and outer boundaries in opposite directions possesses at least two fixed points. The version above follows from applying this result to $T_\varepsilon^{m_1}$ in a neighbourhood of the resonant circle; the m_1-fold symmetry then yields $2m_1$ fixed points.

To gain insight into the theorem, we now analyze the theorem in a constructive manner, using the unperturbed and perturbed twist maps.

Recall the unperturbed twist map $\mathbf{T}_0$ defined by Eqs. (2.61)–(2.62),

$$\mathbf{T}_0 : \begin{cases} I_{1,n+1} = I_{1,n}, \\ \theta_{1,n+1} = \theta_{1,n} + 2\pi\,\alpha(I_{1,n+1}), \end{cases}$$

where $\alpha(I_1) = \omega_1/\omega_2$ is the rotation number. On a rational torus with $\alpha(I^*) = m_2/m_1$, every point is a fixed point of the m_1-th iterate $\mathbf{T}_0^{m_1}$ because the angular advance after m_1 steps is $2\pi m_2$. Thus, the entire circle of radius I^* consists of fixed points.

By the hypothesis of the theorem, $\alpha(I_1)$ is assumed to be a smooth, strictly increasing function of I_1 in the vicinity of I^*. This is a consequence of the non-degeneracy condition [Eq. (2.50)] required for the KAM theorem: the frequency map $I_1 \mapsto \omega_1(I_1)/\omega_2(I_1)$ must have a non-zero derivative. The monotonicity guarantees that on circles slightly outside I^*, where $I_1 = I_+ > I^*$, we have $\alpha(I_+) > m_2/m_1$, so successive iterations of $\mathbf{T}_0^{m_1}$ map points counter-clockwise (increasing

θ_1). Conversely, on circles slightly inside I^*, $I_1 = I_- < I^*$, we have $\alpha(I_-) < m_2/m_1$, and points move clockwise (decreasing θ_1). Exactly at I^* there is no net angular motion. This shear is the fundamental twist that will be disrupted by the perturbation (see Fig. 2.4).

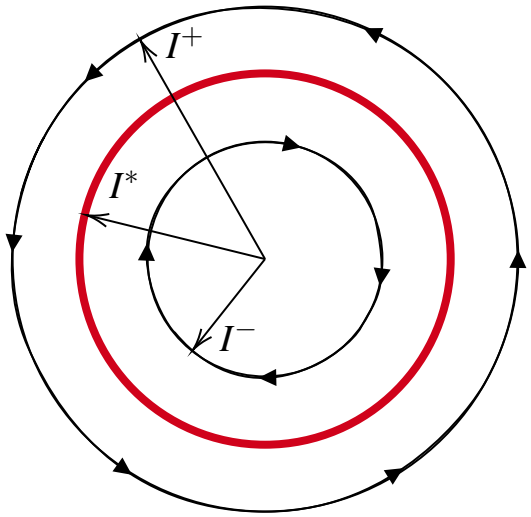


Figure 2.4 – Unperturbed twist map $\mathbf{T}_0$. Points on the circle I^* are fixed under $\mathbf{T}_0^{m_1}$. Points on the outer circle I_+ rotate counter-clockwise, and points on the inner circle I_- rotate clockwise, creating a shear.
Source: By the author

Now consider the perturbed twist map $\mathbf{T}_\varepsilon$ given by Eqs. (2.65)–(2.66),

$$\mathbf{T}_\varepsilon : \begin{cases} I_{1,n+1} = I_{1,n} + \varepsilon F(I_{1,n+1}, \theta_{1,n}), \\ \theta_{1,n+1} = \theta_{1,n} + 2\pi\,\alpha(I_{1,n+1}) + \varepsilon G(I_{1,n+1}, \theta_{1,n}), \end{cases}$$

with $\varepsilon \ll 1$. The invariant circles are no longer preserved. However, for sufficiently small ε, the twist character survives in a neighbourhood of I^*: points initially "above" I^* still experience a net counter-clockwise rotation under $\mathbf{T}_\varepsilon^{m_1}$, while points "below" I^* rotate clockwise, even though I_1 is no longer constant.

Fix an initial angle θ_1 and consider a set of initial actions near I^*. By continuity, between the region of clockwise and counter-clockwise rotation there must exist an action $\tilde{I}$ (depending on θ_1) for which the net angular shift after m_1 iterations is exactly zero. Varying θ_1 across $[0, 2\pi)$, these points trace a smooth closed curve R_ε, called the "curve of no rotation" (see Fig. 2.5). As $\varepsilon \to 0$, R_ε approaches the original circle I^*.

The curve R_ε is not invariant; its points may undergo radial motion when acted upon by $\mathbf{T}_\varepsilon^{m_1}$. Applying $\mathbf{T}_\varepsilon^{m_1}$ to each point of R_ε generates a new curve $\mathbf{T}_\varepsilon^{m_1}(R_\varepsilon)$, which is distinct from R_ε (Fig. 2.6). Because the map is area-preserving, the area enclosed by R_ε equals that enclosed by its image. Consequently, if some portions of R_ε expand radially outward, others must contract,

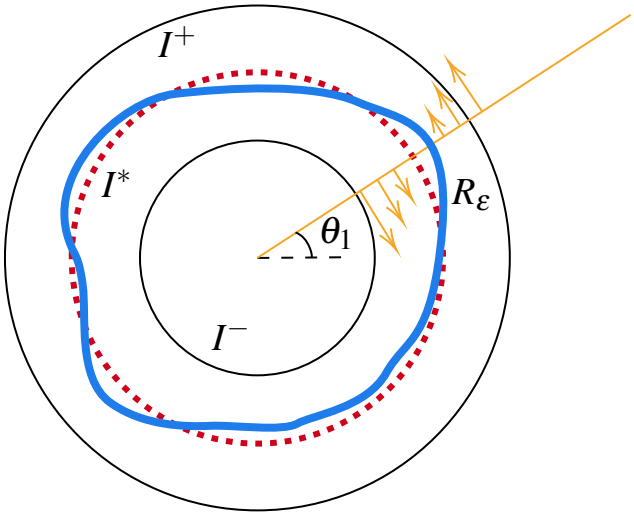


Figure 2.5 – Perturbed twist map $\mathbf{T}_\varepsilon$. The curve R_ε (blue) contains points that experience no net rotation under $\mathbf{T}_\varepsilon^{m_1}$; they can only move radially.
Source: By the author

so that the two curves intersect an *even* number of times. The intersection points have two crucial properties:

- They belong to R_ε, so they suffer no net angular displacement under $\mathbf{T}_\varepsilon^{m_1}$.
- They belong to $\mathbf{T}_\varepsilon^{m_1}(R_\varepsilon)$, meaning that their radial coordinate after m_1 steps returns to the same value (i.e., there is no net radial motion).

Hence each intersection is a fixed point of $\mathbf{T}_\varepsilon^{m_1}$.

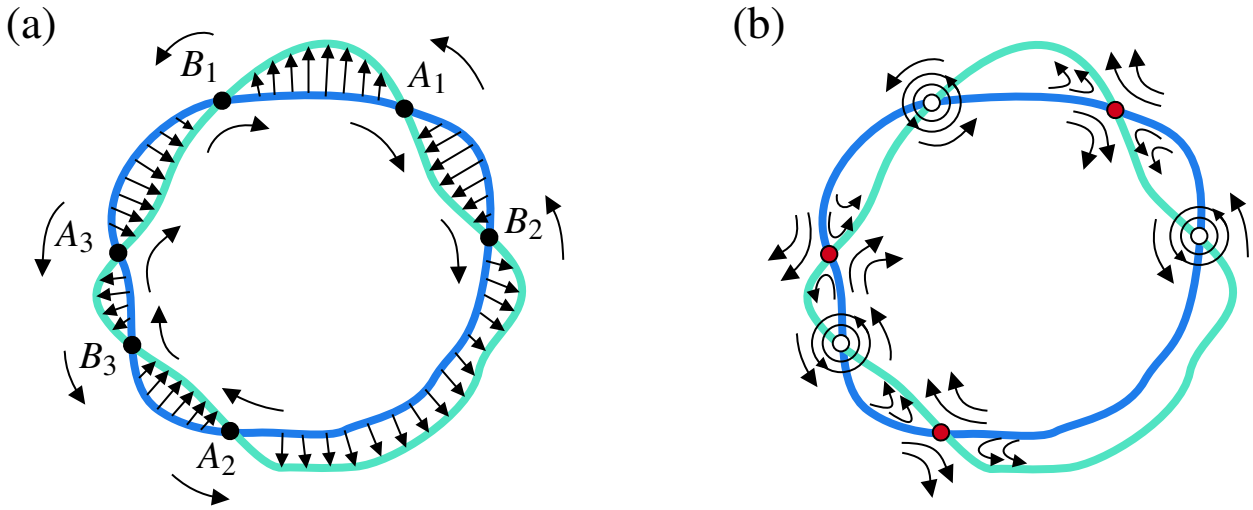


Figure 2.6 – (a) The curve R_ε (red) and its image $\mathbf{T}_\varepsilon^{m_1}(R_\varepsilon)$ (green). Their intersections A_1, A_2 and B_1, B_2 are fixed points of $\mathbf{T}_\varepsilon^{m_1}$. (b) Schematic alternation of elliptic (open circles) and hyperbolic (red circles) points.
Source: By the author

The alternating stability nature follows from the local dynamics near the intersections. As shown in Fig. 2.6, near points B_1, B_2, B_3 the map rotates surrounding points around the fixed

point, characteristic of elliptic (stable) behavior; near A_1, A_2, A_3 the dynamics is saddle-like, characteristic of hyperbolic (unstable) behavior. The elliptic and hyperbolic points appear alternately along the curve. Thus, from the original rational torus, $2m_1$ fixed points emerge, consisting of m_1 elliptic and m_1 hyperbolic points.

In summary, according to the Poincaré–Birkhoff theorem, each rational torus with $\alpha = m_2/m_1$ of the unperturbed system is destroyed by an arbitrarily small perturbation. In its place, $2m_1$ fixed points of the m_1-th iterate appear, half elliptic and half hyperbolic. Figure 2.7 illustrates this for $m_1 = 3$ and $m_1 = 4$: the original rational circles are replaced by 6 and 8 points, respectively, while the irrational tori (sufficiently irrational) survive, although they become slightly deformed.

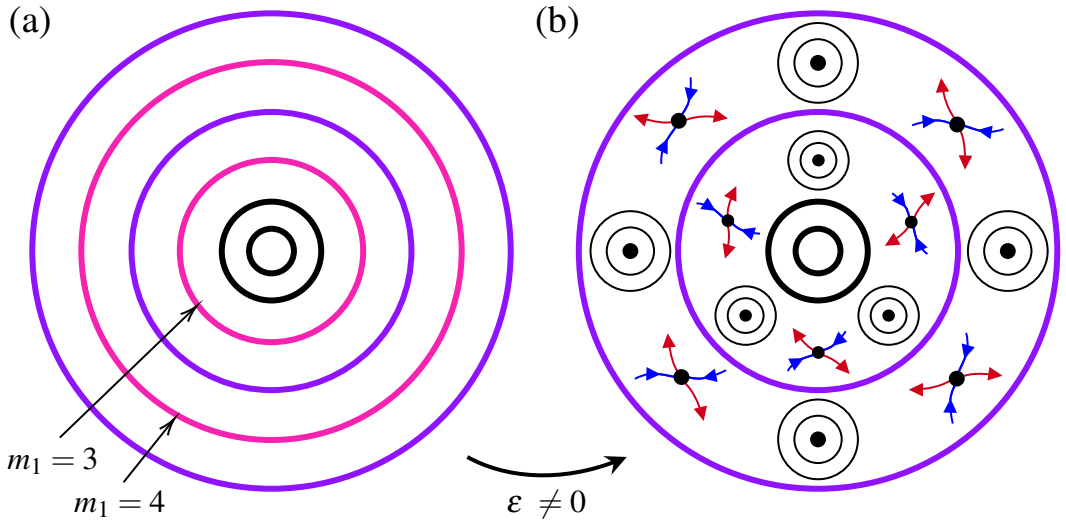


Figure 2.7 – (a) Unperturbed irrational tori (purple) and rational tori (pink) for $m_1 = 3$ and 4. (b) Under perturbation, the irrational tori are smoothly deformed and persist, whereas each rational torus breaks into $2m_1$ fixed points, alternating between elliptic and hyperbolic stability. Source: By the author

Around each surviving elliptic point, the dynamics is again described locally by a twist map. Applying the same reasoning recursively, each of these elliptic islands contains its own rational and irrational tori, and a perturbation (which is already present) breaks the rational ones into smaller elliptic-hyperbolic chains. This self-similar structure repeats ad infinitum, leading to an intricate hierarchical arrangement of islands-around-islands, which is a hallmark of Hamiltonian chaos.

The hyperbolic points, on the other hand, possess stable and unstable invariant manifolds. These curves, which emanate from the hyperbolic points and intersect transversely, form a tangled web that plays a central role in chaotic transport within phase space. The study of these manifolds and their homoclinic/heteroclinic intersections is the subject of the next section.

2.9 Invariant Manifolds: The Skeleton of Chaos

The KAM theorem tells us that most irrational tori survive a small perturbation, while the Poincaré–Birkhoff theorem dictates that each rational torus is replaced by an alternating chain of elliptic and hyperbolic fixed points. At first glance this picture seems complete, but it is far from the whole story. The hyperbolic points are not isolated curiosities; they organise the chaotic motion that pervades non-integrable Hamiltonian systems through their invariant manifolds.

Consider an area-preserving diffeomorphism $F : \mathbb{R}^2 \to \mathbb{R}^2$ with a saddle fixed point $\mathbf{x}^*$. As discussed in the previous section, saddle points are the only hyperbolic fixed points of two-dimensional conservative maps. Therefore, the Jacobian matrix $J = DF(\mathbf{x}^*)$ has two real eigenvalues ξ_1 and ξ_2 satisfying $|\xi_1| > 1$, $|\xi_2| < 1$, and $\xi_1 \xi_2 = 1$. By the Hartman–Grobman theorem, the nonlinear dynamics in a neighbourhood of $\mathbf{x}^*$ is topologically conjugate to its linearisation. Consequently, the local dynamics is described by the linear system

$$\mathbf{x}_{n+1} = J\,\mathbf{x}_n,$$

whose general solution is

$$\mathbf{x}_n = c_1\,\xi_1^n\,\mathbf{u}_1 + c_2\,\xi_2^n\,\mathbf{u}_2, \tag{2.74}$$

where $\mathbf{u}_1$ and $\mathbf{u}_2$ are the eigenvectors corresponding to ξ_1 and ξ_2, and c_1, c_2 are constants determined by the initial condition.

If we place the initial condition exactly along the direction of $\mathbf{u}_1$, then $c_2 = 0$ and

$$\mathbf{x}_n = c_1\,\xi_1^n\,\mathbf{u}_1.$$

Because $|\xi_1| > 1$, the iterates move away from the fixed point as $n \to \infty$ ($\|\mathbf{x}_n\| \to \infty$), while backward iterates ($n \to -\infty$) approach the origin. Conversely, choosing $c_1 = 0$ (the direction of $\mathbf{u}_2$) yields

$$\mathbf{x}_n = c_2\,\xi_2^n\,\mathbf{u}_2,$$

so that forward iterates converge to $\mathbf{x}^*$ as $n \to \infty$, since $|\xi_2| < 1$. These two distinguished directions are invariant under the linearised dynamics.

Definition 2.9.1 — Invariant directions for a linear map. Let $J = DF(\mathbf{x}^*)$ be the Jacobian of a map F at a hyperbolic fixed point $\mathbf{x}^*$, with eigenvalues $|\xi_1| > 1$, $|\xi_2| < 1$ and corresponding eigenvectors $\mathbf{u}_1$, $\mathbf{u}_2$. The *unstable direction* E^u and the *stable direction* E^s

are the subspaces

$$E^u = \operatorname{span}\{\mathbf{u}_1\}, \qquad E^s = \operatorname{span}\{\mathbf{u}_2\}, \tag{2.75}$$

such that

$$\lim_{n\to\infty} J^{-n}\mathbf{x}_0 = \mathbf{x}^* \quad (\mathbf{x}_0 \in E^u), \qquad \lim_{n\to\infty} J^{n}\mathbf{x}_0 = \mathbf{x}^* \quad (\mathbf{x}_0 \in E^s), \tag{2.76}$$

backward iterates along the unstable direction, respectively forward iterates along the stable direction, converge to the fixed point.

For a flow $\dot{\mathbf{x}} = X(\mathbf{x})$ with a hyperbolic equilibrium $\mathbf{x}^*$, the linearised system $\dot{\mathbf{x}} = DX(\mathbf{x}^*)\mathbf{x}$ has solution

$$\mathbf{x}(t) = c_1 e^{\xi_1 t}\mathbf{u}_1 + c_2 e^{\xi_2 t}\mathbf{u}_2, \tag{2.77}$$

where $\xi_1 > 0 > \xi_2$ are the real eigenvalues and $\mathbf{u}_1, \mathbf{u}_2$ the eigenvectors. The stable and unstable directions are defined analogously: E^s is the eigenspace corresponding to negative eigenvalues, and E^u the eigenspace for positive eigenvalues.

The Hartman–Grobman theorem tells us that in a neighbourhood of a hyperbolic fixed point, the nonlinear map F is topologically conjugate to its linearisation J. Thus the invariant directions E^s, E^u of the linear map become slightly distorted invariant curves, called the *local invariant manifolds*.

Definition 2.9.2 — Local invariant manifolds. Let $\mathbf{x}^*$ be a hyperbolic fixed point of a C^1 diffeomorphism F. The *local stable manifold* $W^s_{\text{loc}}(\mathbf{x}^*)$ is the set of points $\mathbf{x}_0$ in a small neighbourhood of $\mathbf{x}^*$ such that forward iterates of F converge to $\mathbf{x}^*$ and never leave the neighbourhood:

$$W^s_{\text{loc}}(\mathbf{x}^*) = \{\, \mathbf{x}_0 \mid F^n(\mathbf{x}_0) \to \mathbf{x}^* \text{ as } n\to\infty,\ F^n(\mathbf{x}_0) \in U \text{ for all } n \geq 0 \,\}.$$

The *local unstable manifold* $W^u_{\text{loc}}(\mathbf{x}^*)$ is defined similarly using backward iterates:

$$W^u_{\text{loc}}(\mathbf{x}^*) = \{\, \mathbf{x}_0 \mid F^{-n}(\mathbf{x}_0) \to \mathbf{x}^* \text{ as } n\to\infty,\ F^{-n}(\mathbf{x}_0) \in U \text{ for all } n \geq 0 \,\}.$$

Stable and Unstable Manifold Theorems [48] guarantees that for a hyperbolic fixed point, $W^s_{\text{loc}}(\mathbf{x}^*)$ and $W^u_{\text{loc}}(\mathbf{x}^*)$ are smooth curves, as smooth as F, tangent respectively to E^s and E^u at $\mathbf{x}^*$ (see Fig. 2.8). In essence, the nonlinear picture is a C^0 deformation of the linear one: the straight invariant directions of the linearised map bend into the curved local invariant manifolds of the full map, while preserving the tangency at the fixed point.

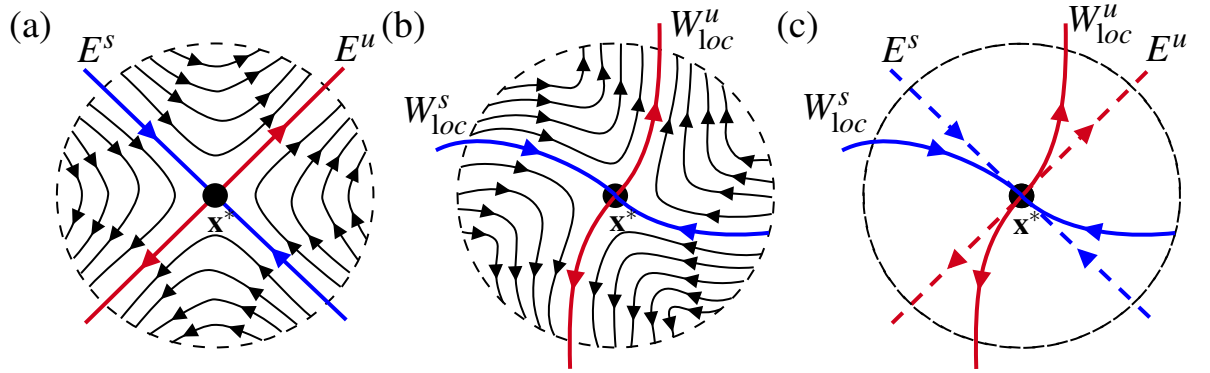


Figure 2.8 – From linearisation to local invariant manifolds. (a) The hyperbolic fixed point $\mathbf{x}^*$ with its stable direction E^s (blue) and unstable direction E^u (red) of the linearised map. (b) In the nonlinear map, these become the local invariant manifolds W^s_{loc} (blue) and W^u_{loc} (red), which are invariant curves tangent to the respective linear directions. (c) Superposition of the linear and nonlinear structures emphasises the tangency condition.
Source: By the author

The local manifolds can be extended globally by iterating the map. Forward images of points on W^u_{loc} generate the global unstable manifold, while backward images of W^s_{loc} generate the global stable manifold.

Definition 2.9.3 — Global invariant manifolds. The *global unstable manifold* $W^u(\mathbf{x}^*)$ and the *global stable manifold* $W^s(\mathbf{x}^*)$ are defined as

$$W^u(\mathbf{x}^*) = \bigcup_{n\geq 0} F^n\left(W^u_{\text{loc}}(\mathbf{x}^*)\right), \tag{2.78}$$

$$W^s(\mathbf{x}^*) = \bigcup_{n\geq 0} F^{-n}\left(W^s_{\text{loc}}(\mathbf{x}^*)\right). \tag{2.79}$$

These sets are invariant under the map: $F(W^s) = W^s$ and $F(W^u) = W^u$.

2.9.1 Homoclinic and heteroclinic intersections

Returning to the picture drawn by the Poincaré–Birkhoff theorem, each hyperbolic fixed point of the perturbed twist map has a stable and an unstable manifold. Poincaré discovered that, far from merging smoothly, the invariant manifolds belonging to neighbouring hyperbolic points intersect in an extremely intricate way.

Definition 2.9.4 — Homoclinic and heteroclinic points. Let $\mathbf{x}^*$ and $\mathbf{y}^*$ be two hyperbolic fixed points. A *homoclinic point* is a point $h \neq \mathbf{x}^*$ that lies at the intersection of $W^s(\mathbf{x}^*)$ and $W^u(\mathbf{x}^*)$; if the intersection is transverse, it is called a *transverse homoclinic point*. A

heteroclinic point is an intersection of $W^s(\mathbf{x}^*)$ with $W^u(\mathbf{y}^*)$ (or vice versa), with $\mathbf{x}^* \neq \mathbf{y}^*$.

These configurations are illustrated schematically in Fig. 2.9.

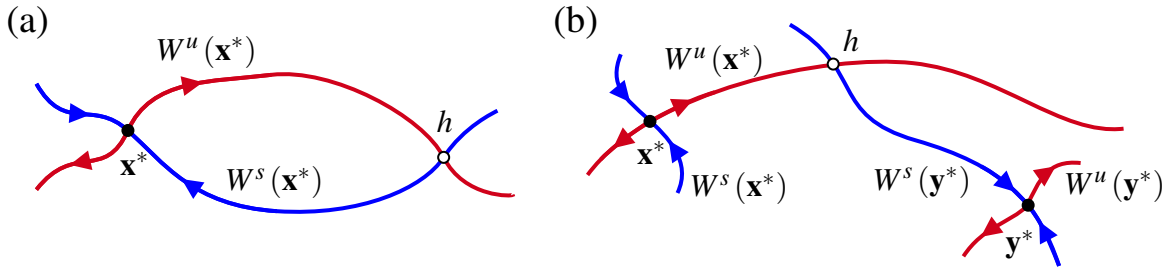


Figure 2.9 – (a) Homoclinic point corresponding to a transversal intersection of $W^s(\mathbf{x}^*)$ and $W^u(\mathbf{x}^*)$; (b) heteroclinic point given by the intersection of $W^s(\mathbf{x}^*)$ and $W^u(\mathbf{y}^*)$.
Source: By the author

REM If the stable and unstable manifolds intersect tangentially, the intersection is said to be *non-transverse*. Such an intersection is called a *homoclinic tangency* (or *heteroclinic tangency* when the manifolds belong to different hyperbolic fixed points).

Because the manifolds are invariant, the image of a homoclinic point under F is again a homoclinic point. Indeed, a homoclinic point lies simultaneously on both the stable and the unstable manifold; since every iterate of a point on a given manifold must remain on that same manifold, the only possibility is that the image of a homoclinic point belongs to another intersection of the two manifolds, hence it is itself a homoclinic point. Consequently, the existence of a single homoclinic intersection forces an infinite set of such points, which accumulate at the fixed point. The orbit generated by the forward and backward iterates of a homoclinic point is called a *homoclinic orbit*: it approaches the fixed point asymptotically both for $n \to \infty$ along the stable manifold and for $n \to -\infty$ along the unstable manifold.

Although every iterate of a homoclinic point is itself a homoclinic point, the next point of the orbit is generally not the next intersection encountered along either invariant manifold. Between two successive iterates lie intersection points belonging to the companion homoclinic orbit. Consequently, a trajectory following one homoclinic orbit appears to "jump over" these intermediate intersections. The reason lies in the preservation of orientation. At one intersection the branches of the stable and unstable manifolds cross with a given orientation (e.g., the unstable manifold crosses the stable manifold from left to right); the map preserves this orientation, so the next iterate of that intersection must exhibit the opposite crossing orientation. This forces the

two families of homoclinic points to appear alternately along each manifold, the crossings of one family interleaved with those of the other.

The necessity of this alternating pattern can also be understood from area conservation. The regions bounded by segments of the stable and unstable manifolds between successive intersections are mapped onto one another. If two consecutive intersections belonged to the same family, some of these regions would be mapped alternately into and out of the homoclinic loop in a manner incompatible with the dynamics near the fixed point.

Because the map is area-preserving on the Poincaré surface of section, the lobes must have equal area. As homoclinic points asymptotically converge to the fixed point, the distance between successive points along the orbit tends to zero. To maintain constant lobe area while preventing self-intersections of the manifolds, the lobes must stretch, fold, and become increasingly elongated and distorted. The resulting intricate structure is the *homoclinic tangle*, illustrated in Fig. 2.10.

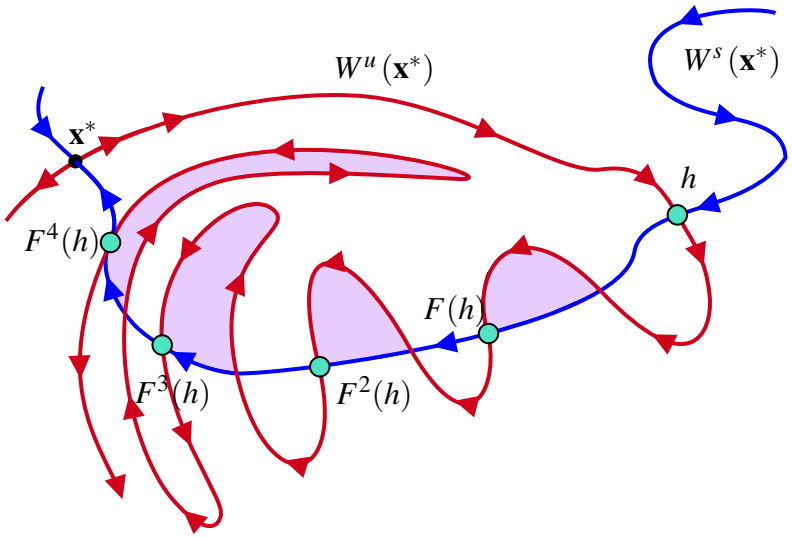


Figure 2.10 – Homoclinic tangle emanating from a hyperbolic fixed point $\mathbf{x}^*$ (green). The stable manifold $W^s(\mathbf{x}^*)$ (blue) and the unstable manifold $W^u(\mathbf{x}^*)$ (red) intersect transversely at the homoclinic point h (blue). Successive iterates of h under the map F are also homoclinic points, giving rise to an infinite set of intersections. The hatched regions have equal area, illustrating the area-preserving property of the map.
Source: By the author

Poincaré described this tangle with characteristic eloquence (see Ref. [165], Section 397):

> "If one seeks to visualise the pattern formed by these two curves and their infinite number of intersections … these intersections form a kind of lattice, a web, a network of infinitely fine mesh; each of the two curves never crosses itself, but must fold back on itself in a very complicated fashion so as to cross all the links of the

> chain an infinite number of times. ... We are struck by the complexity of this figure, which I am not even attempting to draw. Nothing can give us a better idea of the complexity of the three-body problem and of all problems in dynamics ..."

Even from this qualitative picture it is evident that the motion in the vicinity of the unstable fixed points is exceedingly complicated. Although we have so far only examined orbits confined to the invariant manifolds W^s and W^u, a generic orbit starting in this region inherits the same bewildering complexity. This is the seed of deterministic chaos in Hamiltonian systems.

The connection between homoclinic tangles and chaotic motion was rigorously established by Stephen Smale in the 1960s [185]. Smale showed that the existence of a transverse homoclinic point implies the presence of a *horseshoe*, namely a compact invariant set Λ on which the dynamics is topologically conjugate to a shift on a set of bi-infinite sequences. The Birkhoff–Smale theorem states that if a diffeomorphism F possesses a transverse homoclinic point, then some iterate F^m has a horseshoe Λ [185]. The horseshoe set Λ has the following hallmark properties:

1. It contains a countable infinity of periodic orbits of arbitrarily high period.
2. It contains an uncountable infinity of bounded non-periodic orbits.
3. It contains a dense orbit, i.e. the dynamics is topologically transitive[3].

These properties are the signature of deterministic chaos: sensitivity to initial conditions, dense periodic points, and mixing. Thus, the presence of a homoclinic tangle guarantees that orbits starting in its vicinity are chaotic. While a detailed construction of the Smale horseshoe is beyond our scope (see e.g. Refs. [155]), the essential point is that the invariant manifolds are the *skeleton* that organises chaos in Hamiltonian systems.

2.9.2 Synthesis: The structure of the perturbed phase space

We can now summarise the dynamics of an integrable Hamiltonian system under a small perturbation ε:

- **Irrational tori** (most of them) survive, only slightly deformed, as guaranteed by the KAM theorem.
- **Rational tori** are destroyed. In their place, the Poincaré–Birkhoff theorem predicts an even number of fixed points of the corresponding iterate of the Poincaré map, with half elliptic, half hyperbolic, alternating around the former torus.

[3] Essentially, topological transitivity means that there exist points whose orbits can move from one arbitrarily small neighborhood to any other under iteration. A rigorous definition will be given later, more precisely in Definition 3.1.3 on page 57.

- Around each **elliptic point**, the dynamics again resembles a local twist map, so the KAM and Poincaré–Birkhoff analysis repeats on smaller scales, leading to the characteristic island-around-island structure.
- The **hyperbolic points** possess stable and unstable invariant manifolds. These manifolds intersect transversely, forming an intricate homoclinic tangle that gives rise to chaotic orbits via the Smale horseshoe mechanism.

A schematic view of the resulting phase space is shown in Fig. 2.11: irrational tori persist, while each rational torus is replaced by a chain of elliptic islands (surrounded by secondary KAM tori) and a chaotic sea generated by the homoclinic tangle of the hyperbolic points.

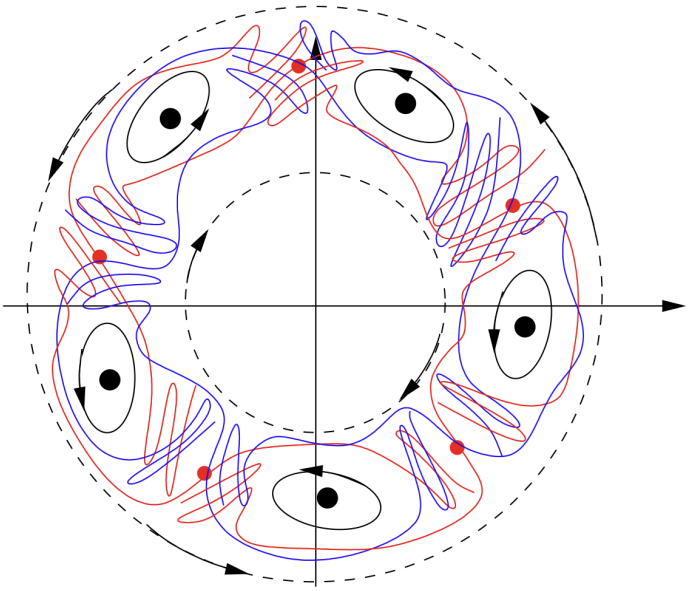


Figure 2.11 – Schematic phase space of a perturbed integrable system. Surviving irrational tori (solid circles), chains of elliptic islands around stable fixed points, and the homoclinic tangle (red/blue curves) forming a chaotic sea.
Source: [47]

Which of these regimes is visited by a particular initial condition depends on its location. As the perturbation strength ε increases, the fraction of phase space occupied by the surviving KAM tori decreases, while the chaotic sea expands. Because the rational numbers are dense, between any two KAM tori lies a destroyed rational torus, and hence a layer of chaos. The infinite self-similarity, with islands within islands, persists at all scales, making the phase space of non-integrable Hamiltonian systems a rich fractal mixture of order and chaos.

In summary, the invariant manifolds emerging from hyperbolic points are the true drivers of chaos: they form the homoclinic tangle that enables orbits to diffuse through large regions of phase space, exploring the complexity that so impressed Poincaré.

CHAPTER

3 Characterizing Chaos

Chaos, together with relativity and quantum mechanics, stands as one of the major scientific developments of the twentieth century. Over the past decades, the study of chaotic systems has evolved into a well-established field, providing new ways to understand complex and intrinsically nonlinear phenomena that were previously difficult to describe. The term *chaos* in the context of interval maps was formally introduced into mathematics by Li and Yorke in 1975 [115], when they established a simple and remarkable result for one-dimensional difference equations, commonly known as the "period three implies chaos" theorem.

In recent years, the study of chaos has gained increasing attention in physics and engineering [160], mainly due to its wide range of applications. Despite its widespread use, the concept of chaos requires a precise definition. Initially, many irregular and unpredictable behaviors, such as weather evolution, were attributed to limitations in measurement or computational accuracy. However, advances in experimental and numerical techniques have shown that the difficulty in long-term prediction is not merely a consequence of these limitations, but rather a fundamental property of certain systems. In particular, even simple deterministic systems can exhibit highly complex dynamics, characterized by strong sensitivity to initial conditions and nonlinear interactions. This quasirandom behavior, often referred to as deterministic chaos, is now recognized as a common feature in many natural systems.

In this chapter, we introduce the main concepts and methods used to identify and analyze chaos in discrete-time dynamical systems. We first present a topological definition of chaos and discuss its main ingredients and implications. We then introduce Lyapunov exponents as a practical and widely used measure of sensitivity to initial conditions, both for one-dimensional and higher-dimensional maps. With these tools in hand, we turn to specific two-dimensional

discrete-time models that will be used in the following chapters as representative examples of chaotic dynamics. In particular, we discuss the standard map, the bouncer model, and the kicked Harper model, emphasizing their construction, phase-space structure, and the role of Lyapunov exponents in their dynamical characterization.

3.1 Defining chaos

The term "chaotic," used to describe the apparently random behavior of deterministic nonperiodic orbits of one-dimensional maps, seems to have been introduced for the first time in 1975 by Li and York [115]. Since then, several definitions of *chaos* have appeared in the literature [113]. Here, we adopt one of the most well-known definitions, due to Devaney [48], which is based on a topological approach and is among the simplest.

Definition 3.1.1 — Chaos . Let S be a metric space. A continuous map $\vec{f} : S \to S$ is said to be **chaotic** on S if

1. $\vec{f}$ has sensitive dependence on initial conditions.
2. $\vec{f}$ is topologically transitive.
3. $\vec{f}$ has periodic points that are dense in S.

We now explain these assumptions in more detail.

Definition 3.1.2 Let S be a metric space. The mapping $\vec{f} : S \to S$ has *sensitive dependence on initial conditions* if there exists $\delta > 0$ such that, for any $\vec{x} \in S$ and any neighborhood Δ of $\vec{x}$, there exist $\vec{y} \in \Delta$ and $n \geq 0$ such that

$$|\vec{f}^n(\vec{x}) - \vec{f}^n(\vec{y})| > \delta,$$

where $\vec{f}^n$ denotes n successive applications of $\vec{f}$.

In practice, this means that there are points arbitrarily close to $\vec{x}$ that eventually separate from it by at least δ under iteration of $\vec{f}$. Note that not every point near $\vec{x}$ must move away from it; it is enough that at least one such point exists in every neighborhood of $\vec{x}$.

Definition 3.1.3 Let S be a set. The mapping $\vec{f} : S \to S$ is said to be *topologically transitive* if for any pair of open sets $U, W \subset S$ there exists $n > 0$ such that

$$\vec{f}^n(U) \cap W \neq \emptyset.$$

This definition implies the existence of points whose orbits can move from one arbitrarily small neighborhood to any other under iteration. Consequently, the dynamical system cannot be decomposed into two disjoint invariant open sets.

Definition 3.1.4 Let A be a set and B a subset of A. The subset B is said to be **dense** in A if for any $a \in A$ and any $\varepsilon > 0$, there exists a point $b \in B$ such that $\|a - b\| < \varepsilon$.

As an example, the rational numbers are dense in the real numbers, and the irrational numbers are also dense in the real numbers, whereas the integers are not. In the case of Devaney's definition, this means that for every point $x \in S$, there exists a periodic orbit arbitrarily close to that point.

After introducing this definition, Robert Devaney adds the following comment:

> To summarize, a chaotic map possesses three ingredients: unpredictability, indecomposability, and an element of regularity. A chaotic system is unpredictable because of sensitive dependence on initial conditions. It cannot be broken down or decomposed into two subsystems (two invariant open subsets) which do not interact under f because of topological transitivity. And, in the midst of this random behavior, we nevertheless have an element of regularity, namely the periodic points which are dense.

Actually, Devaney's definition of chaos is redundant. It can be shown [11] that sensitive dependence on initial conditions follows from topological transitivity and the existence of a dense set of periodic points. For general maps, this is the only redundancy [9]. However, for maps on an interval, finite or infinite, continuity and topological transitivity imply the existence of a dense set of periodic points and sensitive dependence on initial conditions. The proof of this result, which relies on the ordering of $\mathbb{R}$, cannot be extended to maps defined on $\mathbb{R}^n$ for $n > 1$ or on the unit circle S^1 [207].

In physics and the applied sciences, one usually focuses on the first hypothesis in Definition 3.1.1 and uses the notion of chaos in relation to sensitive dependence on initial conditions. The most commonly employed method to distinguish regular from chaotic motion, and to quantify this sensitivity, is the calculation of Lyapunov exponents. This method was developed in the late 1970s, based on theoretical results obtained in the late 1960s. We discuss this method in detail in the following sections.

In conclusion, chaotic motion can be understood as a form of bounded yet unstable stationary

behavior. Although the system remains confined within certain limits over time, it exhibits sensitivity and instability at a local level. Unlike equilibrium states or motions that are periodic or almost periodic, chaotic behavior lacks repeating patterns while still maintaining an overall bounded structure.

3.2 Quantifying chaos: Lyapunov exponents

A defining characteristic of chaotic dynamics is the strong dependence on initial conditions: trajectories that start arbitrarily close to one another can separate very quickly over time, making the orbit unpredictable. The Lyapunov exponents [12, 180, 212] have proven to be one of the most useful dynamical diagnostics for chaotic motion as they provide a quantitative measures of the response sensitivity of a dynamical system to small changes in initial conditions.

The Lyapunov Exponents are asymptotic measures characterizing the average rate of growth (or shrinking) of small perturbations to the orbits of a dynamical system. Their concept was introduced by Lyapunov when studying the stability of nonstationary solutions of ordinary differential equations [128], and has since become a standard approach in nonlinear dynamics.

For chaotic trajectories, at least one exponent is positive, indicating exponential divergence of nearby orbits. In contrast, regular motion is associated with vanishing exponents. Thus, a positive Lyapunov exponent is commonly taken as evidence of chaos. In many situations, computing only the maximal exponent is enough, since a positive value already guarantees chaotic dynamics.

The characterization of the chaoticity of an orbit in terms of the divergence of nearby orbits was introduced by Hénon and Heiles [82] and further used by several authors (e.g., [33–34, 64–66, 188]). In these studies, two initial points were chosen very close to each other, having phase space distance of about 10^{-7}-10^{-6}, and were evolved in time. If the two initial points were located in a region of regular motion, their distance increased approximately linearly with time, while if they belonged to a chaotic region, the distance exhibited an exponential increase in time.

Although the formal theory of Lyapunov exponents was established by Oseledec [154], the connection with exponential divergence became clearer only in later developments [13, 163]. An example is the quantity introduced by Casartelli et al. [33], referred to as the "stochastic parameter", which was later recognized [13] as an estimator of the largest Lyapunov exponent in the long-time limit $t \to \infty$.

In the following, we present the basic ideas behind Lyapunov exponents. We start with one-dimensional maps to illustrate the method in a simple setting, and then extend the discussion

to higher-dimensional systems.

3.2.1 One-dimensional maps

The Lyapunov Exponents are nothing more than a measure of the average exponential rates at which infinitesimal perturbations to a trajectory in a dynamical system grow or decay over time. Given an one-dimensional discrete dynamical system $x_{n+1} = f(x_n)$, where $f : \mathbb{R} \to \mathbb{R}$ is a smooth map. Let x_0 and $y_0 = x_0 + \delta_0$ be two initial conditions infinitesimally close to each other ($|\delta_0| \ll 1$). After one iteration, the two initial conditions become

$$\begin{aligned} x_1 &= f(x_0), \\ y_1 &= f(x_0 + \delta_0). \end{aligned} \tag{3.1}$$

The difference between them is

$$\delta_1 = y_1 - x_1 = f(x_0 + \delta_0) - f(x_0). \tag{3.2}$$

For δ_0 small enough, we can linearize $f(x_0 + \delta_0)$ using a first-order Taylor expansion:

$$f(x_0 + \delta_0) = f(x_0) + f'(x_0)\delta_0 + \mathcal{O}(\delta_0^2), \tag{3.3}$$

leading us to $\delta_1 = f'(x_0)\delta_0$. For the next iteration, we obtain $\delta_2 = f'(x_1)f'(x_0)\delta_0$. Thus, repeating this for n iterations, we obtain

$$\delta_n = \left(\prod_{i=0}^{n-1} f'(x_i) \right) \delta_0. \tag{3.4}$$

We want to quantify how this perturbation grows exponentially

$$\delta_n = \delta_0 \exp(\lambda_n n). \tag{3.5}$$

Thus, we derive the exponential rate of divergence:

$$\lambda_n = \frac{1}{n} \ln \left| \frac{\delta_n}{\delta_0} \right| = \frac{1}{n} \ln \left(\prod_{i=0}^{n-1} \left| f'(x_i) \right| \right) = \frac{1}{n} \sum_{i=0}^{n-1} \ln \left| f'(x_i) \right|. \tag{3.6}$$

The Lyapunov exponent λ is defined as the long-term average exponential rate of separation, i.e.,

$$\lambda = \lim_{n \to \infty} \frac{1}{n} \sum_{i=0}^{n-1} \ln \left| f'(x_i) \right|. \tag{3.7}$$

3.2.2 Higher-dimensional maps

For systems with dimension d, the evolution of infinitesimal perturbations is no longer described by a scalar quantity, but by a vector in the tangent space. Consider the discrete dynamical system

$$\mathbf{x}_{n+1} = \mathbf{f}(\mathbf{x}_n),$$

where $\mathbf{f} : \mathbb{R}^d \to \mathbb{R}^d$ is a smooth map. Suppose that two trajectories start from nearby initial conditions $\mathbf{x}_0$ and $\mathbf{y}_0 = \mathbf{x}_0 + \delta\mathbf{x}_0$, where $\|\delta\mathbf{x}_0\| \ll 1$. After one iteration,

$$\mathbf{x}_1 = \mathbf{f}(\mathbf{x}_0), \qquad \mathbf{y}_1 = \mathbf{f}(\mathbf{x}_0 + \delta\mathbf{x}_0).$$

Expanding $\mathbf{f}$ about $\mathbf{x}_0$ to first order gives

$$\mathbf{f}(\mathbf{x}_0 + \delta\mathbf{x}_0) = \mathbf{f}(\mathbf{x}_0) + J(\mathbf{x}_0)\delta\mathbf{x}_0 + \mathcal{O}(\|\delta\mathbf{x}_0\|^2),$$

where

$$J(\mathbf{x}) = D\mathbf{f}(\mathbf{x})$$

is the Jacobian matrix of the map. Therefore, the perturbation evolves according to

$$\delta\mathbf{x}_1 = J(\mathbf{x}_0)\delta\mathbf{x}_0.$$

Repeating the same argument for subsequent iterations yields

$$\delta\mathbf{x}_2 = J(\mathbf{x}_1)J(\mathbf{x}_0)\delta\mathbf{x}_0,$$

and, after n iterations,

$$\delta\mathbf{x}_n = J_n(\mathbf{x}_0)\delta\mathbf{x}_0, \tag{3.8}$$

where

$$J_n(\mathbf{x}_0) = J(\mathbf{x}_{n-1}) \cdots J(\mathbf{x}_1)J(\mathbf{x}_0)$$

is the product of Jacobian matrices evaluated along the trajectory. Unlike the one-dimensional case, the growth of $\delta\mathbf{x}_n$ generally depends on its initial direction, since the Jacobian acts differently along different directions of the tangent space.

To characterize the asymptotic growth rates independently of the initial orientation of the perturbation vector, one invokes Oseledec's multiplicative ergodic theorem [155]. The theorem states that, for almost every initial condition, the limit

$$\Lambda(\mathbf{x}_0) = \lim_{n\to\infty} \left[J_n^T(\mathbf{x}_0)J_n(\mathbf{x}_0)\right]^{1/2n} \tag{3.9}$$

exists, where $\Lambda(\mathbf{x}_0)$ is a symmetric positive-definite matrix. The logarithms of its eigenvalues define the Lyapunov exponents

$$\lambda_1 \geq \lambda_2 \geq \cdots \geq \lambda_d, \tag{3.10}$$

which quantify the exponential rates of stretching or contraction along the corresponding invariant directions.

Therefore, an d-dimensional system has d characteristic Lyapunov exponents, and we say that the system is chaotic if at least one of them is positive. Moreover, the sum of all Lyapunov exponents is the negative of the phase space contraction rate [203]. For conservative Hamiltonian systems, this sum must be equal to zero. Hence, for systems with a two-dimensional phase space ($d = 2$), there are two exponents and they satisfy $\lambda_1 = -\lambda_2$. In this case, all periodic and quasiperiodic orbits have zero Lyapunov exponents, while chaotic orbits exhibit $\lambda_1 > 0$. In contrast, for dissipative systems the sum of the Lyapunov exponents is negative, reflecting the contraction of phase space volumes. In this case, stable fixed points are characterized by all exponents being negative, while periodic orbits (limit cycles) have one zero exponent, associated with the motion along the orbit, and the remaining exponents negative, indicating stability. Chaotic attractors, on the other hand, are characterized by at least one positive exponent, with the sum of all exponents remaining negative.

Although Eqs. (3.9) and (3.10) are conceptually beatiful, their direct implementation via repeated multiplication of the Jacobian matrices $J_n(\mathbf{x}_0)$ is numerically problematic. In practice, this product quickly becomes dominated by the most rapidly expanding direction of phase space, which leads to loss of information about subdominant directions and prevents reliable estimation of the full Lyapunov spectrum. To address this issue, a variety of numerical strategies have been developed for computing Lyapunov exponents [12, 51, 180, 212].

Here we focus on the QR-based method, which is now widely used in numerical studies. The central idea is to propagate a set of orthonormal tangent vectors while periodically re-orthonormalizing them using a QR decomposition [30]. Given an initial orthonormal matrix $Q_0 \in \mathbb{R}^{d\times d}$, i.e., a matrix satisfying $Q_0 Q_0^T = I$, where each column of Q_0 is a tangent vector, the evolution of Q_0 according to the linearized dynamics is

$$A_1 = J_1 Q_0. \tag{3.11}$$

We now perform a QR decomposition on A_1: $A_1 = Q_1 R_1$, where $Q_1 \in \mathbb{R}^{d\times d}$ is an orthonormal

matrix and $R_1 \in \mathbb{R}^{d\times d}$ is an upper triangular matrix. From this decomposition one can express

$$J_1 = Q_1 R_1 Q_0^{-1}. \tag{3.12}$$

Repeating the same procedure at each step yields $J_2 = Q_2 R_2 Q_1^{-1}$, and in general the recursion leads to

$$J_n = Q_n R_n Q_{n-1}^{-1}. \tag{3.13}$$

where J_n Jacobian matrix at each time n.

This procedure can be interpreted geometrically as follows. At each iteration, the Jacobian matrix J_n evolves the orthonormal basis Q_{n-1} into a new set of tangent vectors $A_n = J_n Q_{n-1}$. These vectors typically lose orthogonality and, if iterated without correction, progressively align with the most unstable direction of the dynamics. This alignment suppresses all other directions and makes it impossible to resolve the full spectrum of expansion rates. The QR decomposition is introduced to avoid this collapse. By writing $A_n = Q_n R_n$, the matrix Q_n provides a new orthonormal basis spanning the same subspace, aligned with the principal directions of local deformation, while R_n records how the previous basis vectors are stretched and recombined during the step. In this sense, R_n contains the local expansion and contraction information expressed in the coordinates defined by Q_{n-1} and Q_n. The diagonal entries $\left|r_{ii}^{(n)}\right|$ quantify instantaneous growth rates along each orthogonal direction. Consequently, Lyapunov exponents can be obtained as time averages of their logarithms:

$$\lambda_i = \lim_{n\to\infty} \frac{1}{n} \sum_{j=1}^{n} \ln \left|r_{ii}^{(j)}\right|. \tag{3.14}$$

Beyond its computational role, the QR algorithm also connects directly to the structure described by Oseledec's theorem [Eq. (3.9)]. Substituting the QR factorization of each Jacobian into the product in Eq. (3.8), one obtains

$$J_n = \left(Q_n R_n Q_{n-1}^{-1}\right)\left(Q_{n-1} R_{n-1} Q_{n-2}^{-1}\right) \ldots \left(Q_1 R_1 Q_0^{-1}\right). \tag{3.15}$$

All of the Q_k^{-1} and Q_k cancel due to the orthogonality of the matrices and the expression simplifies to

$$J_n = Q_n (R_n R_{n-1} \ldots R_1) Q_0^{-1} = Q_n \mathcal{R}_n Q_0^{-1}, \tag{3.16}$$

where $\mathcal{R}_n = R_n R_{n-1} \ldots R_1$. Now, we compute the product $J_n^T J_n$:

$$\begin{aligned} J_n^T J_n &= (Q_0^{-1})^T \mathcal{R}_n^T Q_n^T Q_n \mathcal{R}_n Q_0^{-1}, \\ &= Q_0^{-T} \mathcal{R}_n^T \mathcal{R}_n Q_0^{-1}. \end{aligned} \tag{3.17}$$

This approach produces a similarity transformation, meaning that the matrix $\mathcal{R}_n^T \mathcal{R}_n$ is similar to $J_n^T J_n$, and thus both share the same eigenvalues. As $n \to \infty$, the eigenvalues of the matrix $J_n^T J_n$ converge to those of the limiting matrix $\Lambda(\mathbf{x}_0)$ [Eq. (3.9)], whose eigenvalues define the Lyapunov exponents. Therefore, the eigenvalues of $\mathcal{R}_n^T \mathcal{R}_n$ serve as a numerical estimate of those of $J_n^T J_n$, giving the same Lyapunov exponents in the long-time limit [Eq. (3.14)].

Two-dimensional maps

For two-dimensional systems, the QR procedure can be written in a more explicit recursive form. Then, essentialy, to compute the Lyapunov exponents, we need the diagonal elements of the upper-triangular matrix R_n, because they encode the stretching or contraction along the orthonormal directions. Starting from the QR decomposition we have that from Eq. (3.13), the matrix R_n can be isolated as

$$R_n = Q_n^{-1} J_n Q_{n-1}. \tag{3.18}$$

Since orthogonal matrices preserve inner products, they also preserve lengths and angles. Consequently, they represent isometries of Euclidean space, including rotations, reflections, or combinations of both. Moreover, every orthogonal matrix satisfies $\det(Q) = \pm 1$, where $\det(Q) = 1$ corresponds to orientation-preserving transformations and $\det(Q) = -1$ to orientation-reversing transformations. For two-dimensional systems, it is convenient to parameterize the orthogonal factor Q of the QR decomposition as a rotation matrix, since every orientation-preserving orthogonal transformation in $\mathbb{R}^2$ is a rotation. Accordingly, we write

$$Q_n = \begin{pmatrix} \cos\beta_n & -\sin\beta_n \\ \sin\beta_n & \cos\beta_n \end{pmatrix}, \tag{3.19}$$

where β_n is the rotation angle. Thus, Eq. (3.18) becomes

$$R_n = \begin{pmatrix} r_n^{(11)} & r_n^{(12)} \\ 0 & r_n^{(22)} \end{pmatrix} = \begin{pmatrix} \cos\beta_n & \sin\beta_n \\ -\sin\beta_n & \cos\beta_n \end{pmatrix} \begin{pmatrix} J_n^{(11)} & J_n^{(12)} \\ J_n^{(21)} & J_n^{(22)} \end{pmatrix} \begin{pmatrix} \cos\beta_{n-1} & -\sin\beta_{n-1} \\ \sin\beta_{n-1} & \cos\beta_{n-1} \end{pmatrix}. \tag{3.20}$$

Expanding the matrix element by element, we have

$$r_n^{(11)} = \cos\beta_n(J_n^{(11)}\cos\beta_{n-1} + J_n^{(12)}\sin\beta_{n-1}) + \sin\beta_n(J_n^{(21)}\cos\beta_{n-1} + J_n^{(22)}\sin\beta_{n-1}), \quad (3.21)$$

$$r_n^{(22)} = -\sin\beta_n(-J_n^{(11)}\sin\beta_{n-1} + J_n^{(12)}\cos\beta_{n-1}) + \cos\beta_n(-J_n^{(21)}\sin\beta_{n-1} + J_n^{(22)}\cos\beta_{n-1}), \quad (3.22)$$

$$r_n^{(12)} = \cos\beta_n(-J_n^{(11)}\sin\beta_{n-1} + J_n^{(12)}\cos\beta_{n-1}) + \sin\beta_n(-J_n^{(21)}\sin\beta_{n-1} + J_n^{(22)}\cos\beta_{n-1}), \quad (3.23)$$

$$0 = -\sin\beta_n(J_n^{(11)}\cos\beta_{n-1} + J_n^{(12)}\sin\beta_{n-1}) + \cos\beta_n(J_n^{(21)}\cos\beta_{n-1} + J_n^{(22)}\sin\beta_{n-1}). \quad (3.24)$$

From Eq. (3.24) we obtain an expression for the angle β in terms of its previous value,

$$\tan\beta_n = \frac{J_n^{(21)}\cos\beta_{n-1} + J_n^{(22)}\sin\beta_{n-1}}{J_n^{(11)}\cos\beta_{n-1} + J_n^{(12)}\sin\beta_{n-1}}. \quad (3.25)$$

Consequently, starting from an initial angle β_0 (typically $\beta_0 = 0$), we first compute β_1 using Eq. (3.25). Next, the diagonal elements of the matrix R_n are determined via Eqs. (3.21)–(3.22). By iterating this procedure, the Lyapunov exponent can then be evaluated using Eq. (3.14).

In the next section, we analyze some two-dimensional discrete-time systems and characterize their dynamics using the Lyapunov exponent.

3.3 Some chaotic discrete-time models

Discrete-time dynamical systems, commonly referred to as maps, play a central role in the study of nonlinear dynamics and chaos [3, 189]. In many physical situations, such systems arise naturally either from the stroboscopic observation of time-periodic continuous systems or as simplified models that capture the essential mechanisms responsible for complex behavior [116]. Despite their relatively simple mathematical structure, low-dimensional maps are capable of exhibiting a wide variety of dynamical regimes, including periodic motion, quasiperiodicity, and chaos.

In this section, we explore prominent examples of two-dimensional chaotic discrete-time models. We begin with the Standard Map, a cornerstone model for understanding Hamiltonian chaos, which is derived from the physics of a periodically kicked rotor. Following this, we examine the Bouncer Model, a classic mechanical system used to study Fermi acceleration and the complex dynamics of a particle interacting with an oscillating boundary. Finally, we introduce the Kicked Harper Model, a time-dependent generalization of electron dynamics in a

crystalline lattice under a magnetic field. For each case, we outline the derivation of the mapping and discuss its main dynamical properties.

3.3.1 Standard Map

One of the most widely used models in the study of chaos in Hamiltonian systems is the kicked rotor. Through this model, we can explicitly construct the so-called standard map.

The system consists of a point mass m attached to a massless, inextensible rod of length R, which rotates freely and without friction about a fixed point O (see Fig. 3.1).

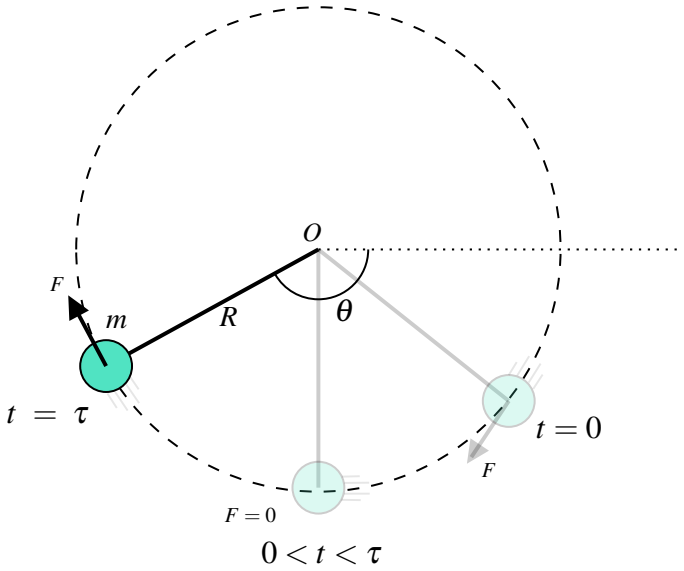


Figure 3.1 – Schematic representation of the kicked rotator, where the system receives impulsive kicks at discrete time intervals.
Source: By the author

The motion takes place in a horizontal plane, so gravitational effects can be neglected. The kinetic energy of the rotor is given by:

$$T(\dot{\theta}) = \frac{1}{2} m R^2 \dot{\theta}^2 \tag{3.26}$$

If the rotor were free, it would rotate around the origin with a constant angular velocity. The system, however, is subjected to periodic impulsive perturbations (the "kicks") such that the intensity of the perturbation depends on the angular position of the rotor. At the mass location, impulsive forces of intensity N_0/R are applied periodically at time instants $t = 0, \pm\tau, \pm 2\tau, \ldots, \pm n\tau$, with a period τ. The resulting torque is time-dependent and can be represented by a sequence of Dirac delta function pulses:

$$N(\theta, t) = N_0 \sin\theta \sum_{n=-\infty}^{\infty} \delta(t - n\tau) \tag{3.27}$$

This is associated with a time-dependent potential energy, neglecting an additive constant:

$$U(\theta,t) = N_0 \cos\theta \sum_{n=-\infty}^{\infty} \delta(t - n\tau) \tag{3.28}$$

Thus, the Lagrangian of the system is:

$$L = \frac{1}{2} mR^2 \dot{\theta}^2 - N_0 \cos\theta \sum_{n=-\infty}^{\infty} \delta(t - n\tau) \tag{3.29}$$

The canonical momentum conjugate to θ is

$$p_\theta = \frac{\partial L}{\partial \dot{\theta}} = mR^2 \dot{\theta}. \tag{3.30}$$

The Hamiltonian then follows from a Legendre transformation:

$$H(p_\theta, \theta, t) = \frac{p_\theta^2}{2mR^2} + N_0 \cos\theta \sum_{n=-\infty}^{\infty} \delta(t - n\tau). \tag{3.31}$$

Since the Hamiltonian depends explicitly on time, it is not conserved; therefore, it is not equal to the total energy of the system.

It is convenient to introduce the dimensionless variables

$$I = \frac{p_\theta}{mR^2}, \qquad K = \frac{N_0}{mR^2}, \tag{3.32}$$

so that Hamilton's equations become

$$\frac{dI}{dt} = K \sin\theta \sum_{n=-\infty}^{\infty} \delta(t - n\tau), \tag{3.33}$$

$$\frac{d\theta}{dt} = I. \tag{3.34}$$

Between two successive kicks, the delta term vanishes and the dynamics is trivial:

$$\frac{dI}{dt} = 0, \qquad \frac{d\theta}{dt} = I. \tag{3.35}$$

leading to:

$$I = \text{const} \tag{3.36}$$

$$\theta = It + \text{const} \tag{3.37}$$

Therefore, the state of the system can be described by sampling it at times separated by one period τ. To construct the corresponding Poincaré map, define the discrete variables immediately before and after the nth kick as (see Fig. 3.2)

$$I_n = \lim_{\varepsilon \to 0} I(n\tau - \varepsilon), \qquad I_n^+ = \lim_{\varepsilon \to 0} I(n\tau + \varepsilon), \tag{3.38}$$

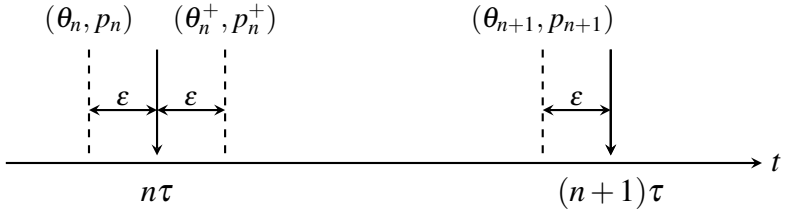


Figure 3.2 – Definition of discrete variables for the periodically forced rotor.
Source: By the author

and

$$\theta_n = \lim_{\varepsilon\to 0} \theta(n\tau-\varepsilon), \qquad \theta_n^+ = \lim_{\varepsilon\to 0} \theta(n\tau+\varepsilon). \tag{3.39}$$

Let us first analyze the dynamics across the nth kick. Integrating the equation for I [Eq. (3.33)] over the interval $[n\tau-\varepsilon, n\tau+\varepsilon]$, we obtain

$$\int_{n\tau-\varepsilon}^{n\tau+\varepsilon} \frac{dI}{dt}\,dt = K\int_{n\tau-\varepsilon}^{n\tau+\varepsilon} \sin\theta \sum_{k=-\infty}^{\infty} \delta(t-k\tau)\,dt. \tag{3.40}$$

Using the sifting property of the Dirac delta function, only the contribution at $t = n\tau$ survives, so

$$I(n\tau+\varepsilon) - I(n\tau-\varepsilon) = K\sin\theta(n\tau). \tag{3.41}$$

Taking the limit $\varepsilon \to 0$, we find

$$I_n^+ = I_n + K\sin\theta_n. \tag{3.42}$$

The angular variable θ remains continuous through the kick. Indeed, integrating the equation for θ [Eq. (3.34)] over the same interval gives

$$\int_{n\tau-\varepsilon}^{n\tau+\varepsilon} \frac{d\theta}{dt}\,dt = \int_{n\tau-\varepsilon}^{n\tau+\varepsilon} I\,dt. \implies \theta(n\tau+\varepsilon) - \theta(n\tau-\varepsilon) = \int_{n\tau-\varepsilon}^{n\tau+\varepsilon} I\,dt. \tag{3.43}$$

Taking the limit $\varepsilon \to 0$, we obtain

$$\theta(n\tau+\varepsilon) = \theta(n\tau-\varepsilon) + \lim_{\varepsilon\to 0}\int_{n\tau-\varepsilon}^{n\tau+\varepsilon} I\,dt. \tag{3.44}$$

Let us rigorously investigate this integral. By taking its absolute value and noting that I is bounded over this interval, we have:

$$\left|\int_{n\tau-\varepsilon}^{n\tau+\varepsilon} I\,dt\right| \le \sup_{t\in[n\tau-\varepsilon,n\tau+\varepsilon]} |I(t)| \cdot [(n\tau+\varepsilon) - (n\tau-\varepsilon)] = \sup_{t\in[n\tau-\varepsilon,n\tau+\varepsilon]} |I(t)| \cdot 2\varepsilon \tag{3.45}$$

Taking the limit as $\varepsilon \to 0$, the 2ε term vanishes, leading to

$$\lim_{\varepsilon\to 0}\left|\int_{n\tau-\varepsilon}^{n\tau+\varepsilon} I\,dt\right| = 0 \tag{3.46}$$

Therefore, by the Squeeze Theorem, the integral term in Eq. (3.44) vanishes, and the equation reduces to

$$\theta_n^+ = \theta_n \tag{3.47}$$

Let us now turn our attention to the dynamics between two successive pulses, where $n\tau+\varepsilon < t < (n+1)\tau-\varepsilon$. As previously established (Eq.(3.36)), in this region there is no impulsive force, so I is constant:

$$I(n\tau+\varepsilon) = I((n+1)\tau-\varepsilon). \tag{3.48}$$

Hence, in the limit $\varepsilon \to 0$,

$$I_n^+ = I_{n+1}. \tag{3.49}$$

For the angular variable, we integrate the equation of motion for θ [Eq. (3.34)] between two successive pulses:

$$\int_{n\tau+\varepsilon}^{(n+1)\tau-\varepsilon} \frac{d\theta}{dt}\,dt = \int_{n\tau+\varepsilon}^{(n+1)\tau-\varepsilon} I\,dt \implies \theta((n+1)\tau-\varepsilon) - \theta(n\tau+\varepsilon) = \int_{n\tau+\varepsilon}^{(n+1)\tau-\varepsilon} I\,dt. \tag{3.50}$$

Since I is constant between kicks [Eq (3.48)], the integral reduces to

$$\theta((n+1)\tau-\varepsilon) - \theta(n\tau+\varepsilon) = I((n+1)\tau-\varepsilon)\cdot\left[(n+1)\tau-\varepsilon-(n\tau+\varepsilon)\right]. \tag{3.51}$$

Taking the limit $\varepsilon \to 0$ and rescaling time so that $\tau = 1$, we obtain

$$\theta_{n+1} = \theta_n^+ + I_{n+1}. \tag{3.52}$$

Therefore, we can summarize the results by the following equations:

$$I_n^+ = I_n + K\sin(\theta_n) \tag{3.53}$$

$$\theta_n^+ = \theta_n \tag{3.54}$$

$$I_{n+1} = I_n^+ \tag{3.55}$$

$$\theta_{n+1} = \theta_n^+ + I_{n+1} \tag{3.56}$$

Combining them, we arrive at the standard map:

$$\begin{aligned} I_{n+1} &= I_n + K\sin(\theta_n) \pmod{2\pi} \\ \theta_{n+1} &= \theta_n + I_{n+1} \pmod{2\pi} \end{aligned} \tag{3.57}$$

The modulo 2π is included because θ is an angular variable and must be identified within the interval $[0, 2\pi)$. Any value outside this interval is reduced by adding or subtracting integer

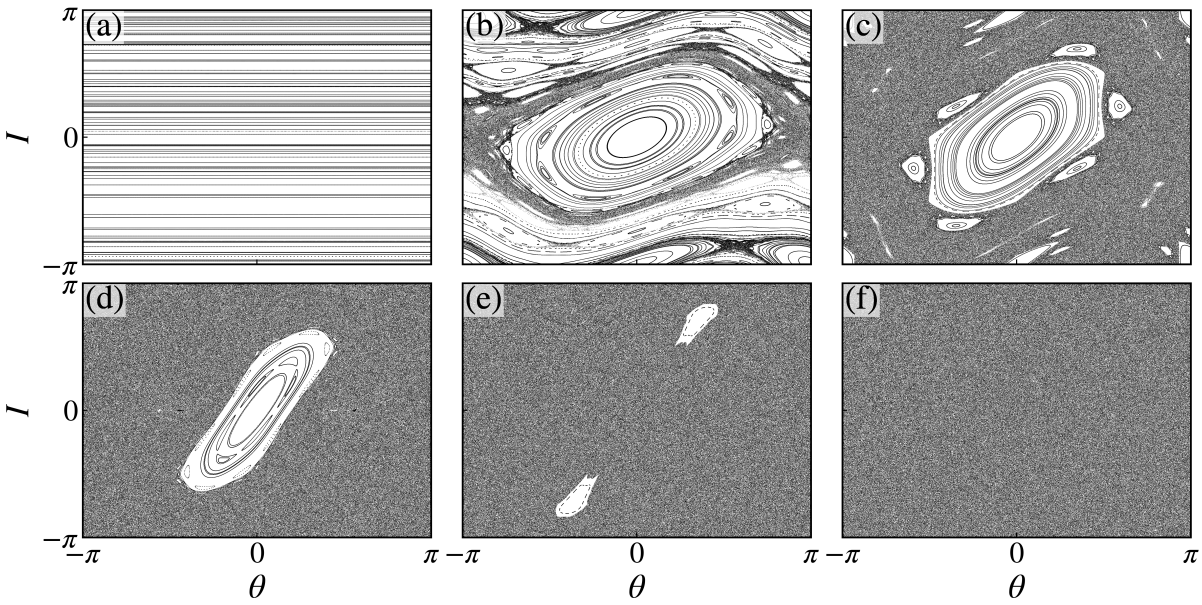


Figure 3.3 – Phase space of the standard map for 100 randomly chosen initial conditions iterated for $N = 1 \times 10^4$ steps, shown for different values of K: (a) $K = 0.0$, (b) $K = 0.9$, (c) $K = 1.6$, (d) $K = 3.2$, (e) $K = 5$, and (f) $K = 10.0$.
Source: By the author

multiples of 2π. In addition, by applying I mod 2π, the dynamics is confined to a toroidal phase space $[-\pi,\pi]\times[-\pi,\pi]$. If this reduction is not performed, the system evolves on a cylindrical phase space $[-\pi,\pi]\times(-\infty,\infty)$. This map is obtained by observing the system at equal time intervals, and for this reason it is called a stroboscopic map.

To illustrate the dynamical behavior of the standard map, Fig. 3.3 presents the phase space of the system for different values of the control parameter K. For $K = 0$, the system exhibits completely regular motion. In this limit, the dynamics is integrable, the momentum p_n remains constant, and trajectories evolve on invariant rotational tori, as shown in Fig. 3.3(a).

As the nonlinearity parameter K increases, part of this regular structure is preserved. According to the Kolmogorov–Arnold–Moser (KAM) theorem, invariant tori associated with sufficiently irrational winding numbers survive as smooth invariant curves, as shown in Fig. 3.3(b). In contrast, resonant tori are progressively destroyed, giving rise to regions of chaotic motion for suitable initial conditions.

At the critical value $K = K_c \approx 0.971635$ [73], the last invariant rotational torus breaks down. Beyond this point, the phase space becomes largely chaotic, and trajectories can move across large regions. For intermediate values of K, regions of regular motion still exist as islands inside the chaotic sea [see Figs. 3.3(c)–3.1(e)]. As K increases further, these islands shrink and eventually become negligible, so that for sufficiently large K the phase space is dominated almost

entirely by chaotic trajectories [Fig. 3.3(f)].

The fixed points of period one can be obtained by imposing

$$\theta_{n+1} = \theta_n, \qquad I_{n+1} = I_n. \tag{3.58}$$

Using Eq. (3.3), this leads to

$$I_n - K\sin\theta_n = 0, \qquad K\sin\theta_n = 0. \tag{3.59}$$

From the second condition, we obtain $\theta_n = m\pi$, with $m \in \mathbb{Z}$. Substituting into the first equation gives $I_n = 0$. Therefore, within the interval $\theta \in [0, 2\pi)$, there are two fixed points of period one, namely

$$(\theta_1^*, I_1^*) = (0,0) \quad \text{and} \quad (\theta_2^*, I_2^*) = (\pi, 0). \tag{3.60}$$

To determine their stability, we consider the Jacobian matrix. For the standard map, the Jacobian matrix takes the form

$$J = \begin{pmatrix} 1 - K\cos\theta_n & 1 \\ -K\cos\theta_n & 1 \end{pmatrix}. \tag{3.61}$$

The determinant of J describes how phase space volumes are transformed under the map. For the present system,

$$\det J = 1, \tag{3.62}$$

which confirms that the map preserves area in phase space.

The stability of periodic orbits in area-preserving maps can be characterized through the residue [72, 74]

$$R_i = \frac{1}{4}\left[2 - \mathrm{Tr}(J_i^n)\right], \tag{3.63}$$

where Tr denotes the trace and J_i^n is the Jacobian matrix evaluated along the orbit of period n.

The nature of the orbit depends on the value of R_i: it is elliptic if $0 < R_i < 1$, parabolic if $R_i = 0$ or 1, and hyperbolic otherwise. For the fixed point $(0,0)$, the residue is $R_1 = K/4$, which corresponds to elliptic behavior for $0 < K < 4$. In contrast, for the fixed point $(\pi, 0)$, one finds $R_2 = -K/4$, implying that this orbit is hyperbolic for any $K > 0$. Summarizing

$$\begin{aligned} (\theta_1^*, I_1^*) = (0,0) \implies R_1 = K/4 \implies \text{elliptic point for } 0 < K < 4 \\ (\theta_2^*, I_2^*) = (\pi, 0) \implies R_1 = -K/4 \implies \text{hyperbolic for any } K > 0 \end{aligned} \tag{3.64}$$

The Lyapunov exponents of the system are now analyzed. To better understand their time evolution, two different initial conditions are considered for $K = 1.6$ [see phase space in Fig. 3.4-(a)]: one located inside a periodic island (green) and another in the chaotic sea (pink). The two

Lyapunov exponents associated with each initial condition are computed, where the darker curve represents the largest exponent and the lighter one the smallest, as shown in Fig. 3.4-(b).

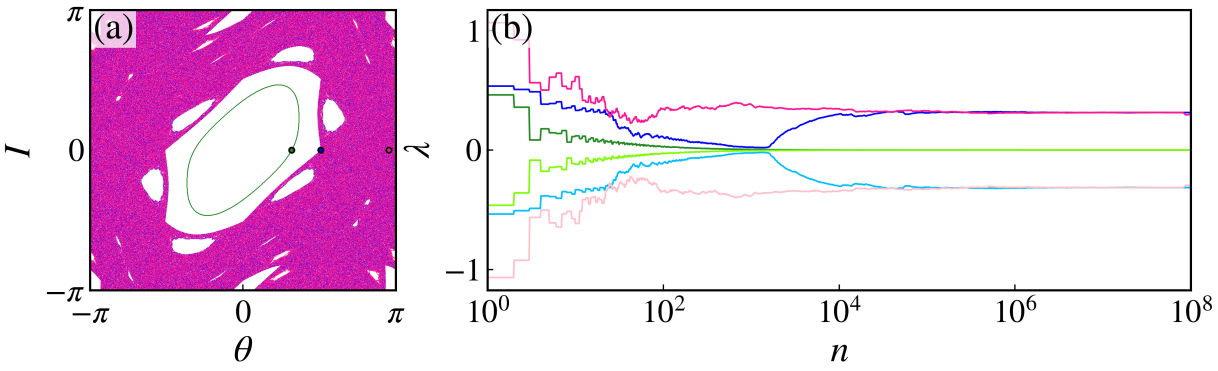


Figure 3.4 – (a) Phase space and (b) time series of the Lyapunov exponents (darker colors denote the largest Lyapunov exponent, while lighter colors denote the smallest) for the standard map with $k = 1.6$. The initial conditions are (green) $(x_0, p_0) = (1.6, 0.0)$, (pink) $(x_0, p_0) = (3.0, 0.0)$, and (blue) $(x_0, p_0) = (1.0, 0.0)$, indicated by bullets in the phase space.
Source: By the author

For the initial condition inside the periodic island, both Lyapunov exponents converge to zero as time increases, which is consistent with regular motion. In contrast, for the initial condition in the chaotic sea, the largest Lyapunov exponent converges to a positive value, indicating chaotic dynamics. In addition, the sum of the exponents satisfies $\lambda_1 + \lambda_2 = 0$, which is expected for an area-preserving map.

Next, an initial condition in the chaotic region but very close to the boundary of the main island (blue) is considered. In this case, the largest Lyapunov exponent initially approaches zero and remains close to this value for a finite time (of the order of 10^3 iterations). After this transient, it increases and eventually reaches the typical value observed for chaotic motion (pink curve).

This behavior can be understood as follows. Chaotic trajectories that pass near regular islands may remain trapped in their vicinity for long, but finite, times. During this stage, the motion resembles quasi-periodic behavior before the trajectory escapes back to the chaotic sea. This effect leads to intermittent dynamics, characterized by alternating intervals of regular-like and chaotic motion, and is commonly known as stickiness [4–5, 35, 39, 93, 145, 218–219]. A more detailed analysis of this phenomenon will be presented in Sec. 4.3.

These trapping events cause temporary decreases in the value of λ_1, which makes the Lyapunov exponent less efficient for identifying chaotic behavior, since a long time is required to reach its asymptotic value.

For this reason, it is useful to compute finite-time Lyapunov exponents (FTLEs) over windows of size m along a trajectory of total length n,

$$\left\{\lambda_1^{(j)}(m)\right\}_{j=1,2,\ldots,n/m},$$

and analyze their probability distribution, $P\big(\lambda_1(m)\big)$.

Szezech et al. [191] showed that, for parameter values where the standard map presents stickiness (for example, $k = 1.5$), the FTLE distribution becomes bimodal [see Fig. 3.5]. The peak at larger values of $\lambda_1(m)$ corresponds to time intervals in which the trajectory is in the chaotic sea, while the secondary peak near zero is associated with trapping near regular islands.

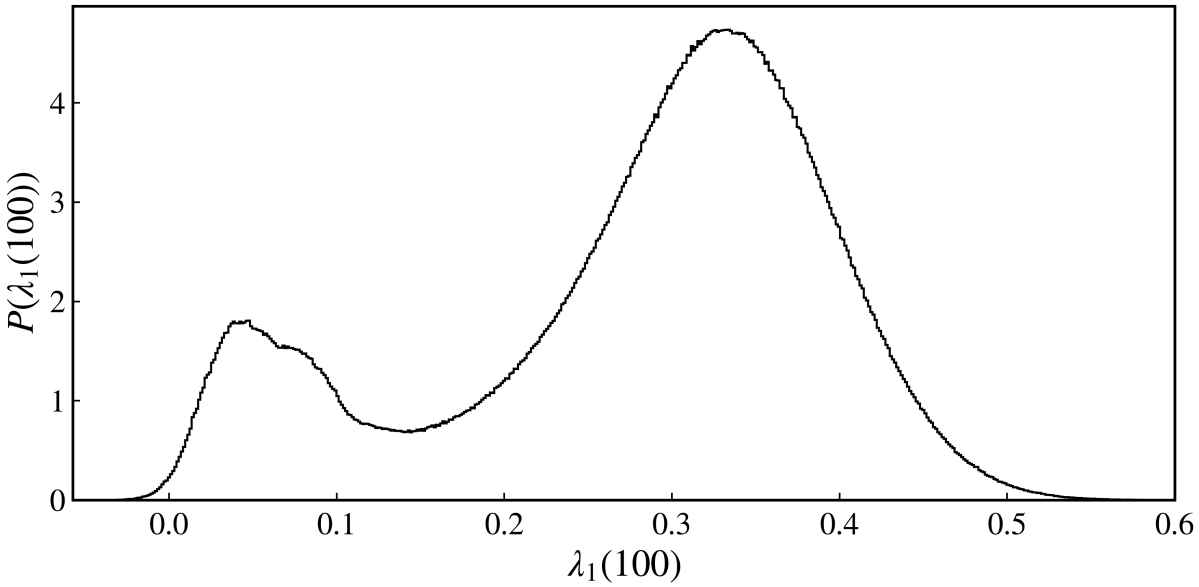


Figure 3.5 – FTLE probability distribution of the standard map with $k = 1.5$ for a single chaotic orbit with initial condition $(I_0, \theta_0) = (1.6, 0)$, with $m = 100$, $n = 10^9$.
Source: By the author

3.3.2 The Bouncer Model

In the study of dynamical systems, especially those exhibiting Fermi acceleration [119], the bouncer model provides an insightful and accessible alternative to the classic Fermi-Ulam model [116]. This model is motivated by the original concept of Fermi acceleration, introduced by Enrico Fermi in 1949 [62] while studying how high-energy cosmic rays interact with oscillating magnetic fields. Fermi proposed that high-energy particles could gain energy through repeated interactions with moving magnetic fields, leading to their acceleration over successive encounters [62]. In the context of time-dependent dynamical systems, Fermi acceleration generally refers to the unbounded growth of a particle's energy (usually the kinetic energy, or equivalently the

velocity) resulting from repeated interactions with a moving boundary or other time-dependent driving mechanism. The bouncer model [100, 167–168] captures the essence of this phenomenon in a simplified setting. It consists of a particle of mass m constrained to move along the vertical axis under a constant gravitational field $\vec{g}$, which acts as a mechanism to return the particle to the collision zone. The particle gains or loses energy through collisions with a wall that oscillates periodically in time, with vertical position given by $y_w(t) = \varepsilon\cos(\omega t)$, where ε is the amplitude and ω is the angular frequency. In this analogy, the particle represents high-energy cosmic rays, the gravitational field simulates reinjection into the collision region, and the moving wall mimics the effect of the oscillating magnetic fields. Figure 3.6 illustrates the bouncer model.

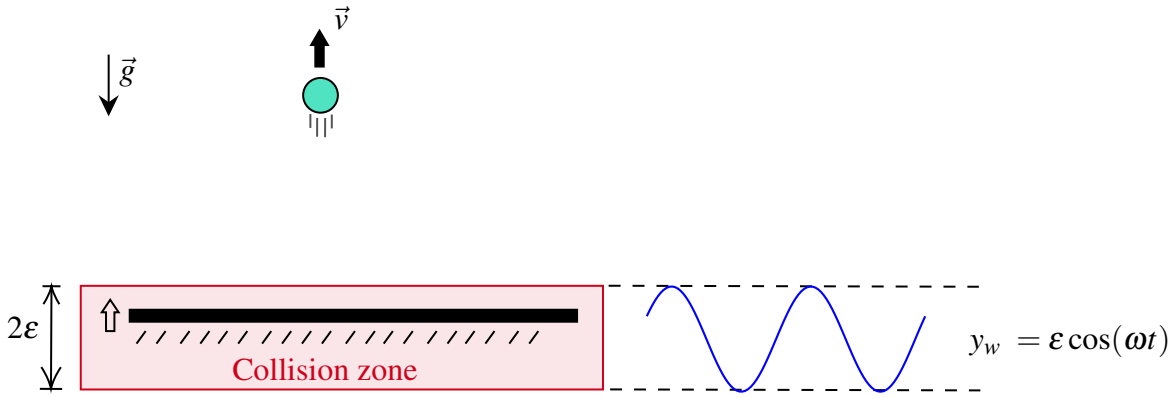


Figure 3.6 – Schematic representation of the bouncer model. A particle with velocity $\vec{v}$ moves along the vertical axis under the influence of a constant gravitational field $\vec{g}$. Energy exchange occurs via collisions with a periodically oscillating wall, whose macroscopic motion is represented by the harmonic function $y_w(t) = \varepsilon\cos(\omega t)$ shown on the right. The shaded area highlights the collision zone, which spans the vertical interval $y \in [-\varepsilon, \varepsilon]$, resulting in a total spatial width of 2ε corresponding to the peak-to-peak amplitude of the wall's oscillation.
Source: By the author

Unlike the Fermi-Ulam model, which uses a secondary fixed wall to push the particle back down, the bouncer model relies on gravity to return the particle. Because of this, when the particle reaches higher velocities, it spends a longer time flying in the gravitational field before returning to the platform. This loss of correlation between successive impacts at high velocities causes diffusion in the velocity phase space, a mechanism directly tied to unlimited energy growth [120].

Complete Version of the Bouncer Model

The dynamics of the bouncer model is described by a two-dimensional discrete map that relates the particle's velocity and time at the n-th collision to those at the $(n+1)$-th collision.

Assume that at time $t = t_n$, the particle leaves the moving wall with an upward velocity $v_n > 0$

from the position:

$$y_p(t_n) = y_w(t_n) = \varepsilon \cos(\omega t_n). \tag{3.65}$$

A "collision zone" is defined in the vertical interval $y \in [-\varepsilon, \varepsilon]$. The dynamics is divided into two cases, depending on whether the particle has enough initial velocity to exit this collision zone before falling back.

Successive Collisions

The position of the particle over a time interval Δt is given by:

$$y_p(t_n + \Delta t) = y_p(t_n) + v_n \Delta t - \frac{1}{2} g (\Delta t)^2.$$

where v_n and $y_p(t_n)$ are the velocity and position, respectively, immediately after a collision.

If the particle's velocity v_n is low, it will not exit the collision zone before hitting the platform again. This event is called a *successive collision*. The time of the next impact, t_c, is determined by equating the position of the particle to the position of the wall: $y_p(t_n + t_c) = y_w(t_n + t_c)$.

This yields the transcendental equation:

$$G(t_c) = \varepsilon \cos[\omega(t_n + t_c)] - \varepsilon \cos(\omega t_n) - v_n t_c + \frac{1}{2} g t_c^2 = 0.$$

Solving for the smallest positive root t_c gives the flight time. The exact time of the next impact is $t_{n+1} = t_n + t_c$, and the particle's velocity just before the impact is

$$v_p(t_{n+1}) = v_n - g t_c \tag{3.66}$$

To calculate the velocity after the collision, it is necessary to change from the inertial reference frame (the laboratory) to the non-inertial reference frame of the moving wall. This change of reference frames is illustrated in Figure 3.7. The inertial frame is represented by (x, y) and the non-inertial frame by (x', y').

At the instant of collision (point P in Figure 3.7), let $\vec{r}$ be the particle's position in the inertial frame, $\vec{R}$ be the wall's position in the inertial frame, and $\vec{r'}$ be the particle's position in the non-inertial frame. This relation among these vectors can be written as:

$$\vec{r} = \vec{r'} + \vec{R}. \tag{3.67}$$

Taking the time derivative of Eq. (3.67) gives the relationship between the velocities:

$$\vec{v}_p = \vec{v}'_p + \vec{v}_w, \tag{3.68}$$

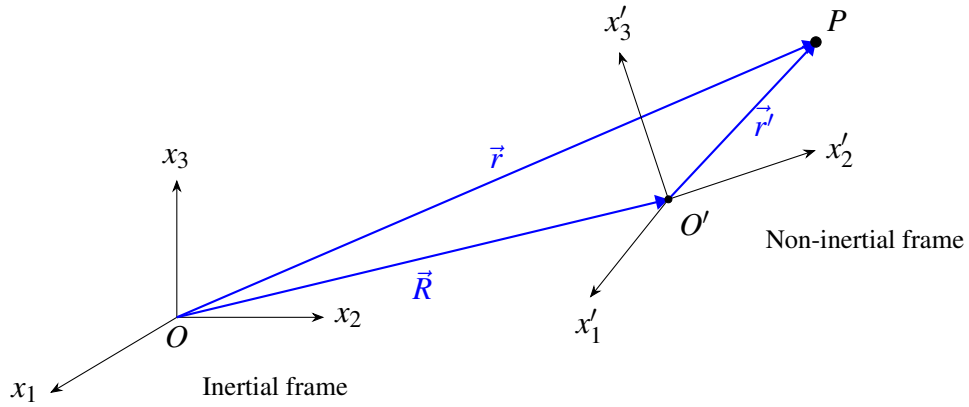


Figure 3.7 – Position vectors in inertial and non-inertial reference frames. The particle position $\vec{r}$ in the inertial frame is expressed as the sum of the position of the moving origin $\vec{R}$ and the relative position $\vec{r'}$ in the non-inertial frame.
Source: By the author

where the subscripts p and w represent the particle and the moving wall, respectively.

Thus, immediately before the collision (t_{n+1}), the relative velocity is:

$$\vec{v}'_{p,\text{before}} = \vec{v}_p(t_{n+1}) - \vec{v}_w(t_{n+1}). \tag{3.69}$$

Assuming a perfectly elastic collision, the *law of reflection* states that the particle's relative velocity reverses direction:

$$\vec{v}'_{p,\text{after}} = -\vec{v}'_{p,\text{before}} \overset{\text{Eq.(3.69)}}{=} -\left(\vec{v}_p(t_{n+1}) - \vec{v}_w(t_{n+1})\right). \tag{3.70}$$

Returning to the inertial reference frame, the particle's velocity immediately after the collision is:

$$\vec{v}_{n+1} = \vec{v}'_{p,\text{after}} + \vec{v}_w(t_{n+1}) \overset{\text{Eq.(3.70)}}{=} -\vec{v}_p(t_{n+1}) + 2\vec{v}_w(t_{n+1}). \tag{3.71}$$

Because the motion is one-dimensional, and noting that the wall velocity is given by $v_w(t) = -\omega\varepsilon\sin(\omega t)$ and $v_p(t_{n+1})$ is defined by Eq. (3.66), the exact mapping between successive collisions is given by:

$$\begin{aligned} t_{n+1} &= t_n + t_c, \\ v_{n+1} &= -[v_n - gt_c] - 2\varepsilon\omega\sin(\omega t_{n+1}). \end{aligned}$$

Indirect Collisions

On the other hand, if the particle's velocity is high enough to leave the collision zone ($y > \varepsilon$), its flight is divided into three parts: the time going up (t_s), the time falling back down to the collision zone (t_d), and the time from re-entering the zone until the impact (t_c). The Figure 3.8 illustrates these phases.

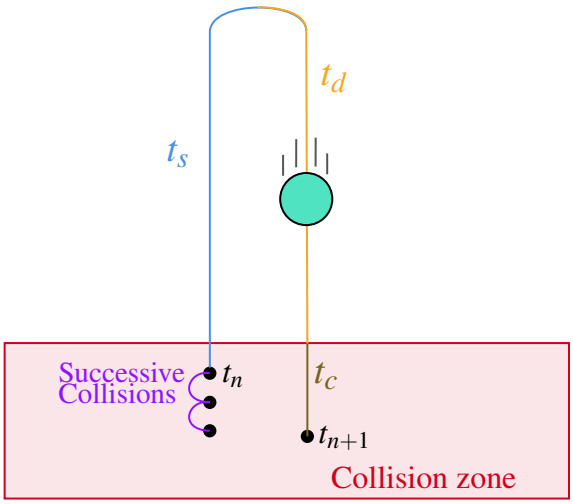


Figure 3.8 – Schematic representation of a particle trajectory. The violet path shows successive collisions within the zone, with the last collision occurring at t_n. The particle then exits the collision zone, following the blue curve upward until it reaches its maximum height during t_s. It then begins to fall back, following the orange curve downward during t_d, until it re-enters the collision zone. The final segment, shown in brown, represents the motion within the collision zone (t_c) until impact, with the instant of impact marked by t_{n+1}, which corresponds to the sum of the previous time intervals. The red-shaded rectangle represents the collision zone.
Source: By the author

1. **Motion upwards:** The particle travels upward until its velocity is zero. The time it takes to reach the maximum height is:

$$t_s = \frac{v_n}{g}.$$

The maximum height reached is:

$$y_{max} = \varepsilon \cos(\omega t_n) + \frac{v_n^2}{2g}.$$

2. **Return to collision zone:** To find the time it takes to fall back to the collision zone boundary ($y = \varepsilon$), Torricelli's equation is applied:

$$v_f^2 = v_0^2 + 2g\,\Delta y.$$

The fall distance is $\Delta y = \varepsilon - y_{\max}$. Starting from zero velocity at the top ($v_0 = 0$), the particle's velocity v_e when re-entering the collision zone is:

$$v_e = -\sqrt{v_n^2 + 2g\varepsilon[\cos(\omega t_n) - 1]}.$$

Using the equation $v_f = v_0 - gt_d$, the descent time t_d is evaluated as:

$$t_d = \frac{v_e}{-g} \quad \Longrightarrow \quad t_d = \frac{\sqrt{v_n^2 + 2g\varepsilon\,[\cos(\omega t_n) - 1]}}{g}.$$

3. **Impact time:** The particle re-enters the collision zone at time $t' = t_n + t_s + t_d$. The remaining time until impact, t_c, is found by matching the position of the falling particle to the position of the wall:

$$y_p(t' + t_c) = y_w(t' + t_c).$$

This provides the transcendental equation:

$$F(t_c) = \varepsilon \cos(\omega(t_n + t_s + t_d + t_c)) - \varepsilon - v_e t_c + \frac{1}{2} g t_c^2 = 0.$$

The full time of the next collision is $t_{n+1} = t_n + t_s + t_d + t_c$. Applying the transformation from the inertial frame to the non-inertial frame, following the same procedure used for successive collisions described in Fig. 3.7, the mapping for indirect collisions becomes

$$\begin{aligned} t_{n+1} &= t_n + t_s + t_d + t_c, \\ v_{n+1} &= \left[\sqrt{v_n^2 + 2g\varepsilon[\cos(\omega t_n) - 1]} + g t_c \right] - 2\varepsilon\omega \sin(\omega t_{n+1}). \end{aligned}$$

Dimensionless Mapping

Analyzing these equations, three main control parameters can be identified: ε (the wall's amplitude), g (gravity), and ω (the wall's frequency). To study the phase space more easily, the equations are simplified by making them dimensionless.

The phase $\phi = \omega t$, the dimensionless velocity $V = \frac{v\omega}{g}$, and a nonlinearity parameter $\varepsilon = \frac{\varepsilon\omega^2}{g}$ are defined. This parameter ε represents the ratio between the wall's maximum acceleration and the acceleration of gravity.

This approach gives the dimensionless Bouncer map:

$$\begin{cases} V_{n+1} = -V_n^* + \phi_c - 2\varepsilon \sin(\phi_{n+1}), \\ \phi_{n+1} = [\phi_n + \Delta T_n] \mod (2\pi), \end{cases} \tag{3.8}$$

where V_n^* is the velocity just before impact and ΔT_n is the total flight time. These depend on the type of collision.

1. For **successive collisions**, $V_n^* = V_n$ and $\Delta T_n = \phi_c$. The time $\phi_c \in (0, 2\pi]$ is found by solving:

$$G(\phi_c) = \varepsilon \cos(\phi_n + \phi_c) - \varepsilon \cos(\phi_n) - V_n \phi_c + \frac{1}{2}\phi_c^2 = 0. \tag{3.72}$$

2. For **indirect collisions**, the velocity before impact is:

$$V_n^* = -\sqrt{V_n^2 + 2\varepsilon(\cos(\phi_n) - 1)},$$

and the total flight time is

$$\Delta T_n = \phi_s + \phi_d + \phi_c.$$

The ascent time is $\phi_s = V_n$, and the descent time is:

$$\phi_d = \sqrt{V_n^2 + 2\varepsilon(\cos(\phi_n) - 1)}.$$

The remaining time $\phi_c \in [0, 2\pi)$ is found numerically by solving:

$$F(\phi_c) = \varepsilon\cos(\phi_n + \phi_s + \phi_d + \phi_c) - \varepsilon - V_n^*\phi_c + \frac{1}{2}\phi_c^2 = 0. \tag{3.73}$$

A Simplified Version: The Static Wall Approximation

Simulating the complete version demands significant computational time because the transcendental equations ($G(\phi_c) = 0$ or $F(\phi_c) = 0$) must be solved at every discrete step. To avoid this, a simplified model called the *static wall approximation* [120] is utilized.

In this approximation, the macroscopic movement of the wall is ignored and the wall is considered fixed at $y = 0$. This makes the flight time very easy to calculate analytically. A particle leaving the fixed platform at $y = 0$ with velocity v_n simply takes a total flight time of $\Delta t = \frac{2v_n}{g}$ to return to the origin.

However, to preserve the non-linear behavior of the system, it is assumed that at the exact moment of impact, the particle exchanges momentum *as if* the wall were moving. The exact time-dependent velocity of the wall is used to calculate the new velocity.

Using the dimensionless variables (ϕ, V, ε), the total flight time is $T_n = 2V_n$. Because the flight is symmetric, the particle hits the wall with the exact opposite of its initial velocity ($V_n^* = -V_n$). Substituting this into the momentum exchange equation gives the simplified mapping:

$$\begin{cases} V_{n+1} = \left|V_n - 2\varepsilon\sin(\phi_{n+1})\right|, \\ \phi_{n+1} = [\phi_n + 2V_n] \mod (2\pi). \end{cases} \tag{3.74}$$

Fig 3.9 illustrates the structure of the phase space associated with Eq. (3.74) as a function of the control parameter ε. As ε increases, the stable regions, primarily associated with periodic fixed points, gradually shrink, leading to the emergence of increasingly large unstable regions in phase space.

Additionally, the phase space exhibits a repeating structure with period π along the velocity axis [124]. Therefore, in this work we restrict the dynamics by considering the mapping modulo

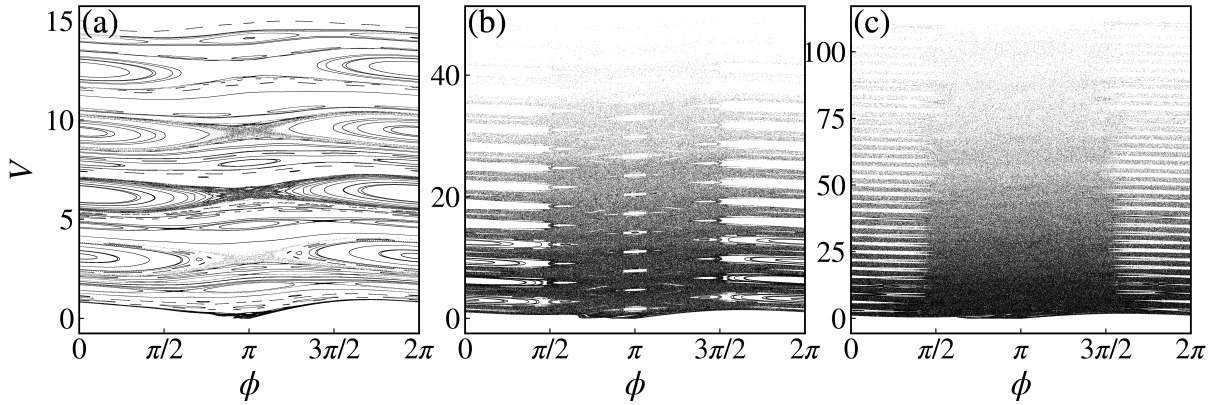


Figure 3.9 – Phase space of the Eq. (3.74) for 100 randomly chosen initial conditions iterated for $N = 1 \times 10^4$ steps, shown for different values of ε: (a) $\varepsilon = 0.2$, (b) $\varepsilon = 0.4$, and (c) $\varepsilon = 0.6$.
Source: By the author

π for the velocity variable. The map then becomes

$$\begin{cases} V_{n+1} = (V_n - 2\varepsilon \sin(\phi_{n+1})) \mod (\pi), \\ \phi_{n+1} = (\phi_n + 2V_n) \mod (2\pi). \end{cases} \tag{3.75}$$

To illustrate how the dynamics of the bouncer map changes, Fig. 3.10 shows the phase space for different values of the control parameter ε. For $\varepsilon = 0$, the motion is completely regular. In this case, the system is integrable, and trajectories lie on invariant curves, as shown in Fig. 3.10(a).

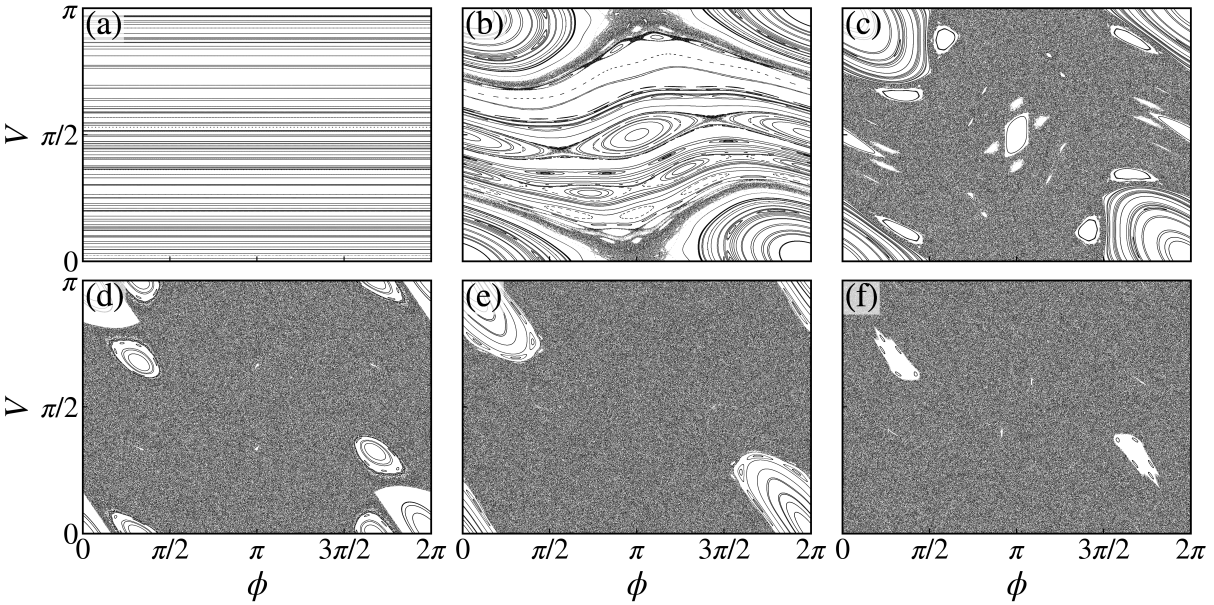


Figure 3.10 – Phase space of the Bouncer Model [Eq. (3.75)] for 100 randomly chosen initial conditions iterated for $N = 1 \times 10^4$ steps, shown for different values of ε: (a) $\varepsilon = 0$, (b) $\varepsilon = 0.2$, (c) $\varepsilon = 0.4$, (d) $\varepsilon = 0.6$, (e) $\varepsilon = 0.8$, and (f) $\varepsilon = 1.2$.
Source: By the author

As the nonlinearity parameter ε increases, the phase space is no longer completely regular,

although part of its structure is still preserved. According to the Kolmogorov–Arnold–Moser (KAM) theorem, invariant tori with sufficiently irrational winding numbers persist as smooth curves, as shown in Fig. 3.10(b). In contrast, resonant tori are gradually destroyed, and regions of chaotic motion appear for appropriate initial conditions.

It is also possible to establish a connection between the bouncer model and the standard map. By introducing the variables $I_n = 2V_n$, $K = 4\varepsilon$, and $\theta_n = \phi_{n+1} + \pi$, the bouncer model can be written in the form of the standard map. In this way, increasing the control parameter ε drives the system from a regime with local chaos to one with global chaotic motion, in agreement with what is observed in the standard map. In particular, at the critical value $\varepsilon_c = K_c/4 \approx 0.971635/4 \approx 0.242909$, the invariant spanning curves (invariant tori) are destroyed. For $\varepsilon > \varepsilon_c$, the phase space becomes mostly chaotic, and trajectories can move through large regions [see Fig. 3.10(c)]. For intermediate values of ε, regular islands are still present inside the chaotic region [Figs. 3.10(d)–(e)]. As ε increases further, these islands become smaller, and for sufficiently large ε the dynamics is almost entirely chaotic [Fig. 3.3(f)].

The period-one fixed points are obtained by setting

$$\phi_{n+1} = \phi_n, \qquad V_{n+1} = V_n. \tag{3.76}$$

Using the definition of the map, we obtain

$$\phi_n + 2V_n = \phi_n, \qquad V_n - 2\varepsilon \sin\phi_n = V_n. \tag{3.77}$$

The first condition gives $2V_n = 0$, which leads to $V_n = 0$. The second condition implies $\sin\phi_n = 0$, resulting in $\phi_n = m\pi$, where $m \in \mathbb{Z}$. Therefore, the fixed points are located at

$$(\phi^*, V^*) = (m\pi, 0), \tag{3.78}$$

within the domain of the map.

To study their stability, we evaluate the Jacobian matrix of the transformation, which in this case is given by

$$J = \begin{pmatrix} 1 & 2 \\ -2\varepsilon\cos\phi_{n+1} & 1 - 4\varepsilon\cos\phi_{n+1} \end{pmatrix}. \tag{3.79}$$

For this system, the determinant of J is

$$\det J = 1, \tag{3.80}$$

which shows that the map preserves area in phase space.

The stability of the fixed points can be analyzed using the residue [72, 74]

$$R = \frac{1}{4}\left[2 - \mathrm{Tr}(J)\right]. \tag{3.81}$$

Since $\mathrm{Tr}(J) = 2 - 4\varepsilon\cos\phi^*$, we obtain

$$R = \varepsilon\cos\phi^*. \tag{3.82}$$

Thus, the type of each fixed point depends on the value of ϕ^*. For $\phi^* = 0$, we have $R = \varepsilon$, so the fixed point is elliptic for $0 < \varepsilon < 1$. For $\phi^* = \pi$, we obtain $R = -\varepsilon$, which implies that this fixed point is hyperbolic for any $\varepsilon > 0$. For larger multiples of π, the values repeat these two cases due to the 2π-periodicity. In summary,

$$\begin{aligned} (\phi^*, V^*) = (0,0) &\implies R = \varepsilon \implies \text{elliptic point for } 0 < k < 1 \\ (\phi^*, V^*) = (\pi,0) &\implies R = -\varepsilon \implies \text{hyperbolic for any } k > 0 \end{aligned} \tag{3.83}$$

The Lyapunov exponents of the bouncer map are now analyzed. To examine their time evolution, two initial conditions are selected for a representative value of the control parameter $\varepsilon = 0.4$ (see phase space in Fig. 3.11-(a)): one inside a regular island (green) and another in the chaotic sea (pink). The corresponding Lyapunov exponents are computed, with the darker curve denoting the largest exponent and the lighter curve the smallest one [Fig. 3.11-(b)].

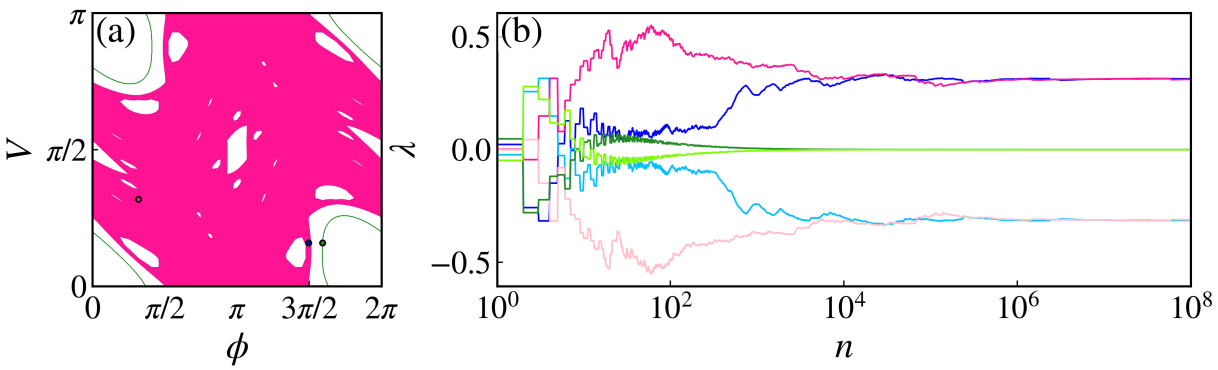


Figure 3.11 – (a) Phase space and (b) time series of the Lyapunov exponents (darker colors denote the largest Lyapunov exponent, while lighter colors denote the smallest) for the bouncer map with $\varepsilon = 0.4$. The initial conditions are (green) $(\phi_0, V_0) = (4.7, 0.5)$, (pink) $(\phi_0, V_0) = (1.0, 1.0)$, and (blue) $(\phi_0, V_0) = (5.0, 0.5)$, indicated by bullets in the phase space.
Source: By the author

For the initial condition chosen inside the regular island, both exponents decrease and tend to zero as time grows, which is consistent with regular motion. On the other hand, when the initial condition is placed in the chaotic sea, the largest exponent approaches a positive value,

indicating chaotic behavior. In addition, the sum of the two exponents is zero, $\lambda_1 + \lambda_2 = 0$, as expected for an area-preserving map.

A second initial condition is then considered in the chaotic region, but close to the boundary of the main island. In this case, the largest Lyapunov exponent first remains close to zero for a long transient time, of the order of 10^2 iterations, before increasing and reaching the usual value associated with chaotic trajectories. This delay is related to the fact that chaotic orbits can spend long finite times near regular islands, during which their motion resembles quasi-periodic dynamics before escaping back to the chaotic sea.

To investigate these transient regimes, finite-time Lyapunov exponents (FTLEs) are computed over windows of size m along a trajectory of total length n,

$$\left\{\lambda_1^{(j)}(m)\right\}_{j=1,2,\ldots,n/m},$$

and their probability distribution, $P\big(\lambda_1(m)\big)$, is analyzed.

Livorati et al. [124] showed that, for the bouncer map, the FTLE distribution may be bimodal when sticky regions are present [Fig. 3.12]. The larger peak corresponds to time intervals in which the orbit explores the chaotic sea, while the secondary peak near zero is associated with temporary trapping near regular islands.

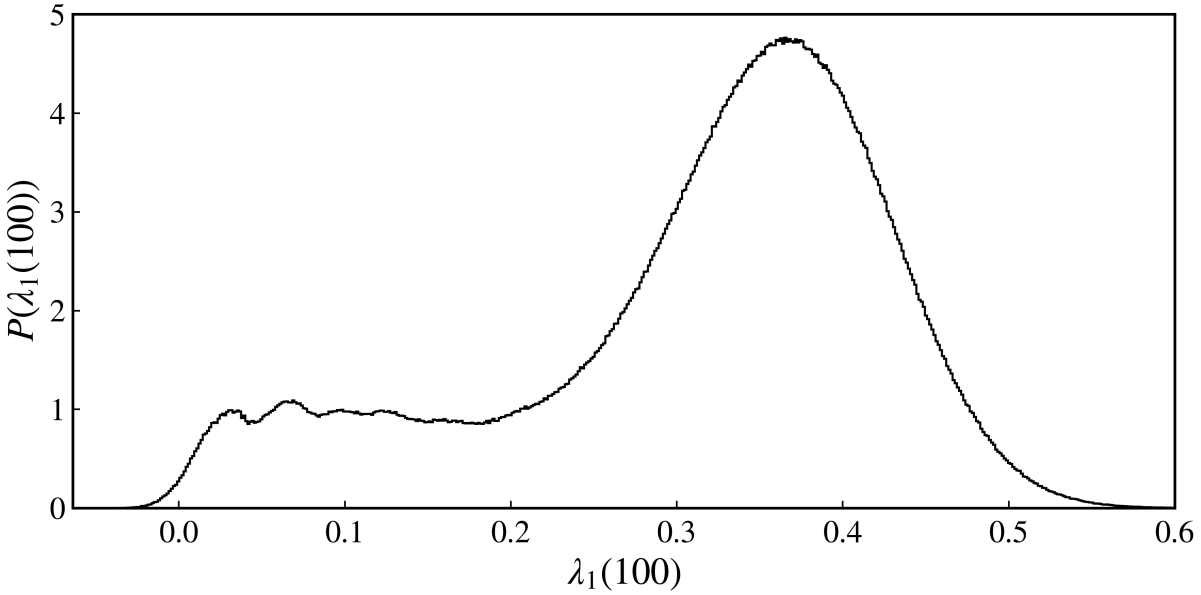


Figure 3.12 – FTLE probability distribution of the bouncer map with $\varepsilon = 0.4$ for a single chaotic orbit with initial condition $(\phi_0, V_0) = (1,1)$, with $m = 100$, $n = 10^9$.
Source: By the author

3.3.3 Kicked Harper Model

The Harper model, originally proposed in [79], was developed to describe the behavior of electrons in a crystalline lattice subjected to a magnetic field. In this framework, the system is treated within a tight-binding approximation, typically applied to symmetric cubic lattices, allowing one to capture the influence of a uniform magnetic field on conduction-band electrons. Its semiclassical formulation leads to an effective one-dimensional Hamiltonian of the form [112]:

$$H_{HM}(q,p,t) = -V_2\cos(2\pi p) - V_1\cos(2\pi q). \tag{3.84}$$

Although this Hamiltonian has been extensively analyzed in the literature [61, 67, 84, 210], its dynamics remain integrable, which limits the range of behaviors that can be observed. To overcome this restriction and explore more complex dynamical regimes, a time-dependent generalization known as the kicked Harper model was introduced. This extension incorporates periodic impulsive perturbations and is given by [107, 109]:

$$H_{KHM}(q,p,t) = -V_2\cos(2\pi p) - V_1\cos(2\pi q)\,K(t), \tag{3.85}$$

where the kicking function is defined as

$$K(t) = \tau\sum_n \delta(t-n\tau),$$

with τ representing the time interval between successive kicks, and V_1, V_2 being control parameters.

By integrating the equations of motion from one kick to the next, one obtains a discrete-time mapping that describes the system evolution [122, 181, 205]:

$$\begin{cases} p_{n+1} = p_n - \gamma_1\sin(2\pi q_n) \pmod 1, \\ q_{n+1} = q_n + \gamma_2\sin(2\pi p_{n+1}) \pmod 1, \end{cases} \tag{3.86}$$

where the parameters are defined as $\gamma_i = 2\pi V_i\tau$. The phase space is limited, with $(q,p) \in [0,1)\times[0,1)$, implying motion on a torus.

An alternative route to obtain a map of the same class is through the kicked oscillator model, described by the Hamiltonian [220, 223]:

$$H_{KOM}(u,v,t) = \frac{1}{2}(u^2+v^2) - K\cos(q)\,\tau\sum_n \delta(t-n\tau), \tag{3.87}$$

where u and v denote dimensionless momentum and position variables, respectively, α represents the rotation angle between kicks, and K controls the perturbation strength. This Hamiltonian

represents the motion of a particle at a given frequency in a constant magnetic field and in the field of an electric wave packet of arbitrary amplitude, propagating perpendicular to the magnetic field [220]. The corresponding discrete dynamics can be written as [117, 159]:

$$u_{n+1} = (u_n + K \sin v_n)\cos\alpha + v_n \sin\alpha, \tag{3.88}$$

$$v_{n+1} = -(u_n + K \sin v_n)\sin\alpha + v_n \cos\alpha. \tag{3.89}$$

When the resonance condition $\alpha = \frac{2\pi}{q}$ is satisfied [217], the system experiences q kicks during one full oscillation period. In the particular case $q = 4$, and considering only the leading-order contribution in K, iterating the map four times yields a simplified representation [118]:

$$\begin{cases} v_{n+1} = v_n - 2K \sin(u_n), \\ u_{n+1} = u_n + 2K \sin(v_{n+1}). \end{cases} \tag{3.90}$$

This expression is equivalent to the mapping in Eq. (3.86) when $\gamma_1 = \gamma_2 = 2K$. For this reason, in the present work we restrict the analysis to the symmetric case $\gamma_1 = \gamma_2 \equiv \gamma$.

The kicked Harper model appears in a variety of physical contexts. Examples include the dynamics of charged particles interacting with electrostatic waves in the presence of a transverse magnetic field [44, 94, 220], electron transport in two-dimensional periodic structures under magnetic fields [107–108], and certain flow configurations in ideal incompressible fluids [161, 216].

To demonstrate the evolution of the dynamical behavior of the kicked Harper map, Fig. 3.13 shows the phase space of the system for different values of the control parameter γ. For $\gamma = 0$, all initial conditions correspond to fixed points; therefore, no nontrivial dynamics is observed.

For small but nonzero values of γ, regular structures are formed, as illustrated in Fig. 3.13(a). As γ increases, according to the Kolmogorov–Arnold–Moser (KAM) theorem, invariant tori associated with sufficiently irrational winding numbers persist as smooth invariant curves, as seen in Fig. 3.13(b-c). In contrast, resonant tori are progressively destroyed, giving rise to chaotic regions for appropriate initial conditions. With further increase of γ, the island around $(0.5, 0.5)$ is destroyed [Fig. 3.13(d)], while other islands shrink and eventually become negligible [Fig. 3.13(e)]. For sufficiently large γ, the phase space becomes almost entirely dominated by chaotic trajectories [Fig. 3.13(f)].

The period-one fixed points are obtained by requiring

$$q_{n+1} = q_n, \qquad p_{n+1} = p_n. \tag{3.91}$$

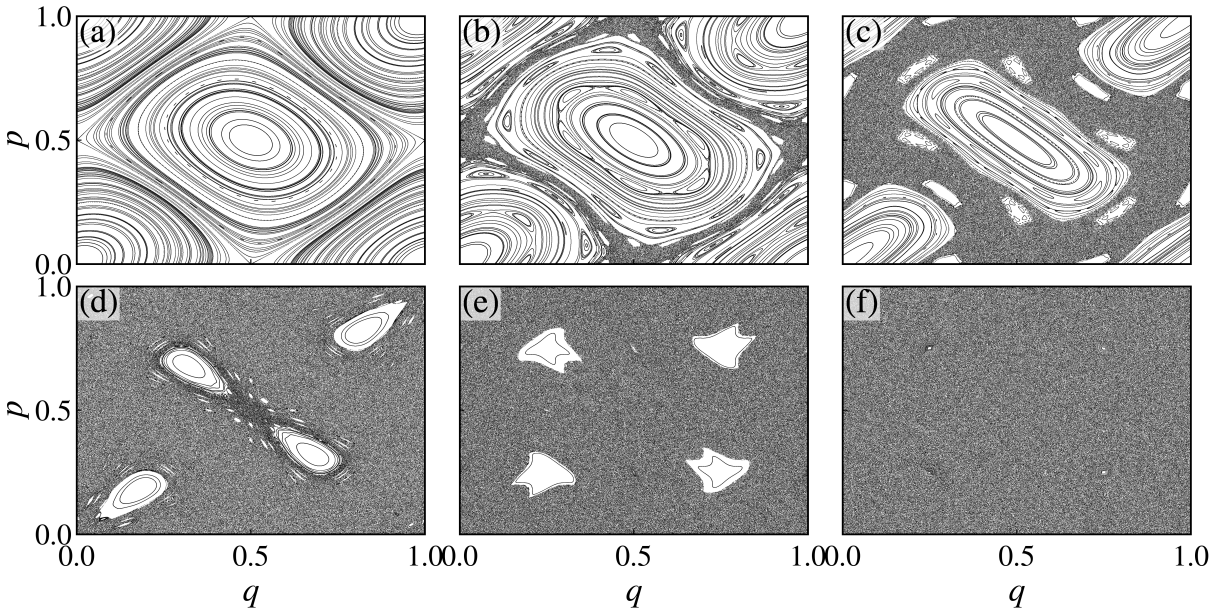


Figure 3.13 – Phase space of the kicked Harper map for 100 randomly chosen initial conditions iterated for $N = 1 \times 10^4$ steps, shown for different values of γ: (a) $\gamma = 0.1$, (b) $\gamma = 0.2$, (c) $\gamma = 0.3$, (d) $\gamma = 0.4$, (e) $\gamma = 0.5$, and (f) $\gamma = 1$.
Source: By the author

From the first equation of the map, we have

$$\gamma \sin(2\pi q_n) = 0, \tag{3.92}$$

and from the second one,

$$\gamma \sin(2\pi p_n) = 0. \tag{3.93}$$

Thus, the fixed points satisfy

$$q^* \in \left\{0, \frac{1}{2}\right\}, \qquad p^* \in \left\{0, \frac{1}{2}\right\}, \tag{3.94}$$

so there are four period-one fixed points in the interval $[0,1)$:

$$(0,0), \quad \left(0, \frac{1}{2}\right), \quad \left(\frac{1}{2}, 0\right), \quad \left(\frac{1}{2}, \frac{1}{2}\right). \tag{3.95}$$

To study their stability, we compute the Jacobian matrix. Writing

$$a = 2\pi\gamma, \tag{3.96}$$

the Jacobian takes the form

$$J = \begin{pmatrix} 1 - a^2 \cos(2\pi x_n)\cos(2\pi y_{n+1}) & a\cos(2\pi y_{n+1}) \\ -a\cos(2\pi x_n) & 1 \end{pmatrix}. \tag{3.97}$$

The determinant of this matrix is

$$\det J = 1, \tag{3.98}$$

confirming area preservation in the phase space.

The stability of periodic orbits in area-preserving maps can also be studied using the residue [72, 74]

$$R = \frac{1}{4}\left[2 - \mathrm{Tr}(J)\right]. \tag{3.99}$$

For the fixed points $(0,0)$ and $\left(\frac{1}{2},\frac{1}{2}\right)$, we obtain

$$R = \pi^2\gamma^2, \tag{3.100}$$

while for $\left(0,\frac{1}{2}\right)$ and $\left(\frac{1}{2},0\right)$, we find

$$R = -\pi^2\gamma^2. \tag{3.101}$$

Using the condition $0 < R < 1$ for elliptic motion, we see that the first pair is elliptic for

$$0 < \pi^2\gamma^2 < 1 \quad \Rightarrow \quad 0 < \gamma < \frac{1}{\pi}. \tag{3.102}$$

For $\gamma > \frac{1}{\pi}$, these points become hyperbolic. On the other hand, since $R < 0$ for the second pair, they are hyperbolic for any $\gamma > 0$. Summarizing,

$$\begin{array}{l} (0,0), \left(\frac{1}{2},\frac{1}{2}\right) \implies R = \pi^2\gamma^2 \implies \text{elliptic for } 0 < \gamma < \frac{1}{\pi}, \text{ hyperbolic for } \gamma > \frac{1}{\pi} \\ \left(0,\frac{1}{2}\right), \left(\frac{1}{2},0\right) \implies R = -\pi^2\gamma^2 \implies \text{hyperbolic for any } \gamma > 0 \end{array} \tag{3.103}$$

The Lyapunov exponents of the kicked Harper map are now analyzed. To examine their time evolution, two initial conditions are chosen for a fixed value of the control parameter $\gamma = 0.25$ (see phase space in Fig. 3.14-(a)): one inside a regular region (green) and another in the chaotic sea (pink). The corresponding Lyapunov exponents are computed, with the darker curve representing the largest exponent and the lighter curve the smallest one, as shown in Fig. 3.14-(b).

For the initial condition inside the regular region, both exponents decrease and tend to zero as time increases, which is consistent with regular motion. In contrast, for the initial condition in the chaotic sea, the largest exponent converges to a positive value, indicating chaotic behavior. Since the kicked Harper map is area preserving, the two exponents also satisfy $\lambda_1 + \lambda_2 = 0$.

A second initial condition is selected in the chaotic sea, very close to the boundary of a regular island. In this case, the largest Lyapunov exponent stays close to zero for an extended transient interval, of the order of 10^3 iterations, before rising to the typical value observed for

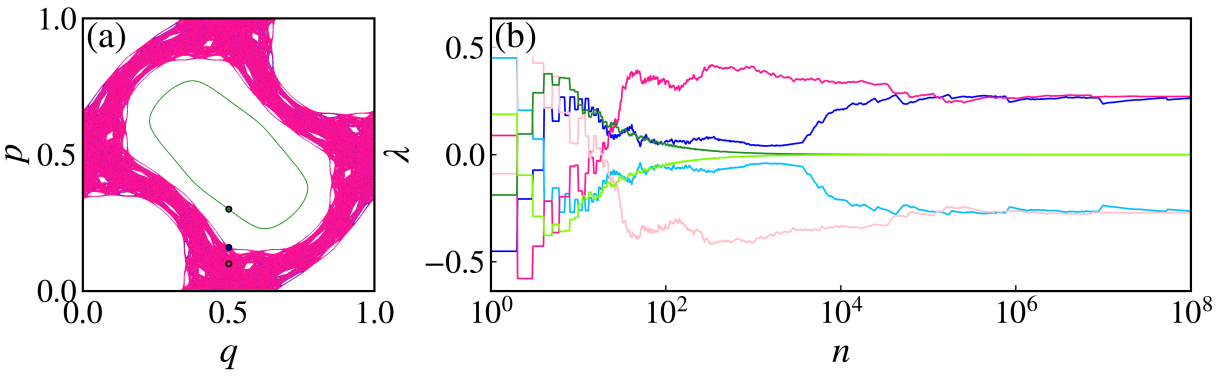


Figure 3.14 – (a) Phase space and (b) time series of the Lyapunov exponents (darker colors denote the largest Lyapunov exponent, while lighter colors denote the smallest) for the kicked Harper map with $\gamma = 0.25$. The initial conditions are (green) $(q_0, p_0) = (0.5, 0.16)$, (pink) $(q_0, p_0) = (0.5, 0.1)$, and (blue) $(q_0, p_0) = (0.5, 0.3)$, indicated by bullets in (a).
Source: By the author

chaotic trajectories. This behavior is associated with the temporary trapping of chaotic orbits near regular islands. Such trapping events generate an intermittent pattern, in which the trajectory alternates between motion that is almost regular and motion that is clearly chaotic.

To better understand these intermittent patterns, finite-time Lyapunov exponents (FTLEs) are computed over windows of size m along a trajectory of total length n, and the corresponding probability distribution, $P(\lambda_1(m))$, is then examined in Fig. 3.15.

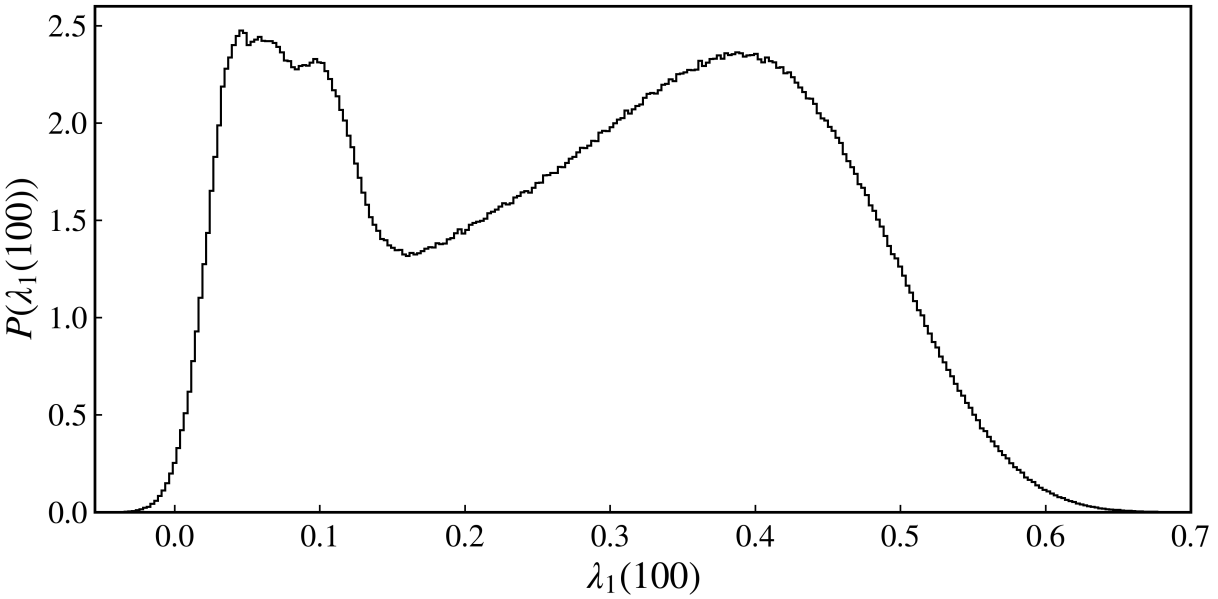


Figure 3.15 – FTLE probability distribution of the kicked Harper map with $\gamma = 0.25$ for a single chaotic orbit with initial condition $(q_0, p_0) = (0.5, 0.1)$, with $m = 100$, $n = 10^9$.
Source: By the author

For this map, the FTLE distribution appears bimodal, as observed in the Fig 3.15. Both peaks have comparable heights: one is associated with orbit segments evolving in the chaotic sea, while the other, located near zero, corresponds to intervals during which the orbit remains temporarily

trapped close to a regular island.

This section examines the dynamics of mixed phase spaces, where regular and chaotic regions coexist and trajectories can alternate between chaotic motion and long-lasting trapping near regular structures. This trapping, known as stickiness, plays an important role in the long-time dynamics because the hierarchical organization of islands and their surrounding structures affects the temporal correlations of trajectories.

For the finite-time Lyapunov exponent, stickiness appears as a characteristic bimodal distribution. The main peak corresponds to motion in the chaotic sea, while a secondary peak at lower values corresponds to episodes of trapping near regular islands. As shown throughout this section, this behavior occurs in three different dynamical models, making the bimodal distribution a useful indicator of chaotic and sticky dynamics.

The bimodal distribution, however, does not resolve the internal structure of the sticky component. In the next chapter, we use the Hurst exponent to further characterize the sticky dynamics through long-range temporal correlations. Unlike the Lyapunov exponent, which produces a single secondary peak for the sticky component, the Hurst exponent reveals a multimodal structure. These peaks are associated with different levels of trapping and provide signatures of the hierarchical organization of the phase space. Thus, the Hurst exponent offers a finer characterization of sticky dynamics and resolves structures that remain hidden in the Lyapunov-exponent distribution.

CHAPTER

4 Hurst Exponent: A New Indicator of Chaos

In dynamical systems, a dynamical trap refers to a region of phase space where a trajectory can remain for a long, yet finite, time while exhibiting nearly regular behavior, even though the overall dynamics is chaotic [219]. One important example of such traps is the phenomenon known as *stickiness* [1, 4–5, 41, 145, 179, 218].

Stickiness occurs when chaotic orbits spend extended periods in the vicinity of regular structures in phase space, such as stability islands. During these intervals, the trajectories behave almost like quasiperiodic orbits, becoming temporarily trapped near these structures. This behavior has a strong impact on global properties of the system, including the decay of correlations [35, 93, 145] and transport processes [218].

Before escaping, trajectories are often confined within regions bounded by cantori [60], which are Cantor-like remnants of destroyed invariant tori. These structures act as partial barriers to transport in phase space. Once inside a cantorus, a chaotic orbit may penetrate deeper into inner cantori, leading to a hierarchical process that continues to increasingly smaller scales within the well-known islands-around-islands structure [133].

Another example of a dynamical trap is the behavior known as cascade of bifurcations type trajectories (CBTT), reported in the fractional dynamics literature. To the best of our knowledge, this behavior has so far been reported exclusively in fractional dynamical systems. In this phenomenon, a single trajectory undergoes a sequence of qualitative changes in its temporal evolution, alternating between periods of confinement to progressively smaller regions of phase space and excursions into larger regions. Although referred to as a cascade of bifurcations in the fractional dynamics literature, these changes do not correspond to conventional bifurcations

induced by variations of a system parameter. Rather, the term describes the successive changes in the dynamical behavior observed along the temporal evolution of a single trajectory.

A common approach to quantify these trapping effects is through the finite-time Lyapunov exponent (FTLE) [152, 191], which measures the exponential rate of separation of nearby trajectories over finite time intervals. The FTLE can provide a useful signature of stickiness by distinguishing chaotic motion from episodes of trapping near regular structures. However, its description of sticky dynamics remains limited, as different trapping regimes can be grouped within the same low-FTLE component. In addition, its computation requires explicit knowledge of the governing equations, which may not be available in experimental or natural systems. For fractional systems, the situation is even more complex, as the definition of the Jacobian must be extended to incorporate memory effects [114, 214]. These limitations motivate the use of complementary measures that can characterize the temporal structure of sticky dynamics without relying directly on the equations of motion.

In this chapter, we introduce the Hurst exponent [85] as an alternative measure to identify regular motion, chaotic dynamics, and dynamical traps. The Hurst exponent quantifies the long-term memory of a time series and can be computed with minimal assumptions about the underlying system. We show that it allows a clear distinction between regular regions and transitions to chaos as system parameters vary. Furthermore, the finite-time Hurst exponent (FTH) reveals a multimodal distribution associated with the hierarchical structure of phase space.

4.1 Historical Origins

After the Second World War, rapid urban growth in Europe and in other regions led to a sharp increase in the demand for electricity. At that time, much of this energy was produced from hydropower, which in turn required the construction of large artificial reservoirs for both power generation and irrigation. This practical need, together with the availability of longer historical records, stimulated the study of hydrological time series and gave rise to the development of reservoir design theory, which relies fundamentally on historical river-flow data.

The conceptual foundations of reservoir design go back to the pioneering work of the Austrian engineer Rippl [170], however, a major contribution came from the British hydrologist Harold Edwin Hurst. Hurst worked in Egypt for over 60 years, mainly on projects to control the Nile River. By analyzing long records of Nile flows, Hurst identified the phenomenon now known as the *Hurst effect*, which has often been associated with the presence of long-range dependence in

the data.

Hurst's problem was to determine the ideal storage capacity for a reservoir fed by a given annual inflow sequence $x_1, x_2, \ldots, x_N$ and required to release a constant amount $\bar{x}$ (including losses) each year. Under these conditions, Hurst introduced the adjusted range R as being the required reservoir capacity. This quantity is defined as the difference between the maximum d_N^+ and the minimum d_N^- of the cumulative departures from the mean:

$$R = \max_{1\leq i\leq N}(x_1 + x_2 + \cdots + x_i - i\bar{x}) - \min_{1\leq i\leq N}(x_1 + x_2 + \cdots + x_i - i\bar{x}) = d_N^+ + \left|d_N^-\right|. \tag{4.1}$$

Understanding how this adjusted range grows with the sample size N is essential for reservoir design. Since observed flow records are often limited in length, Hurst compared records from different geophysical contexts by normalizing the range with the standard deviation S of the data,

Understanding how R behaves is central to choosing the right reservoir volume. Because most of his river flow records were shorter than 100 years, he looked at many other kinds of natural records to get longer series. To compare records of different types and sizes, he divided R by the sample standard deviation S,

$$S = \left[\frac{1}{N-1}\sum_{i=1}^{N}(x_i - \bar{x})^2\right]^{\frac{1}{2}}. \tag{4.2}$$

This led to the *rescaled range* statistic R/S, a dimensionless quantity that allows different time series to be compared on the same basis. Hurst applied this procedure to river flows, rainfall, temperature, lake levels, atmospheric pressure, tree-ring growth, and several other records, covering more than 800 time series with observation intervals ranging from 40 to 2000 years [88]. He discovered a remarkably consistent simple power-law relationship.

$$\frac{R}{S} \propto N^H. \tag{4.3}$$

where H is the *Hurst exponent*. In his data, Hurst reported values of H between 0.46 and 0.93, with an average close to 0.73 and a standard deviation of about 0.09 [85]. This finding directly contradicted his own earlier result [86]: for sequences of independent, identically distributed normal variables, the asymptotic value of H must be 0.5.

The observation that many natural time series exhibit $H > 0.5$, while uncorrelated random sequences lead to $H = 0.5$, became known as the *Hurst phenomenon* or *Hurst effect*. The

exponent H is therefore commonly used as a measure of persistence in a time series. In practical terms, Hurst's result for the Nile River, $H \approx 0.72$, implied that any reservoir regulating that river would have to be substantially larger than what classical theory would predict.

The initial interpretations of the Hurst Effect were developed based on empirical findings [87, 143]. In fact, the first attempts to theoretically explain the Hurst phenomenon failed and were eloquently summarized by Lloyd [126] in the following statement:

> "We are, then, in one of those situations, so salutary to theoreticians, in which empirical discoveries stubbornly refuse to accord with theory.... We are forced to the conclusion that either the theorists' interpretation of their own work was inadequate or their theories are falsely based; possibly both conclusions apply."

The first successful theoretical explanation emerged when leading statisticians, among them Moran [147], conjectured that the Hurst effect might stem from an unusual form of serial dependence. Building on this idea, Mandelbrot [136] and Mandelbrot and Van Ness [138] introduced Fractional Gaussian Noises (FGNs), a class of processes that yield $H > 0.5$ even in the limit of infinite record length. Unlike short-memory processes, which fall within the domain of attraction of ordinary Brownian motion, FGNs are derived from a Fractional Brownian Motion whose increments are weighted averages of all past increments of a standard Brownian motion. The key distinction lies in the dependence structure: for short-memory processes the integral of the autocorrelation function from lag zero to infinity remains finite, whereas for FGNs it diverges. This property implies that the process retains a memory of all past events, producing epochs of persistently high or low values, a characteristic Mandelbrot and co-workers termed the Joseph effect [139].

Later, Mandelbrot and Wallis [141] argued that long-memory could explain Hurst's findings in geophysical records, and they reported that many such records display substantial long-range statistical dependence, that is, they concluded that "the strength of long-range statistical dependence in geophysical records is considerable". Even so, the hydrological community was not fully convinced. A major concern was the lack of a clear physical mechanism capable of sustaining correlations over such long time scales. This skepticism led other authors, including O'Connell [151] and Wallis and O'Connell [209], to suggest that the observed effect might instead arise from strong short-term dependence. However, from a theoretical point of view, Mandelbrot [137] and Siddiqui [182] showed that processes within the domain of attraction of Brownian motion must satisfy $H \to 0.5$ asymptotically. Therefore, short-memory dynamics

can reproduce the Hurst effect only as a finite-sample or pre-asymptotic phenomenon, but not as a genuine asymptotic property. This result ruled out short-range dependence as a complete explanation for values of $H > 0.5$.

However, the hydrologic community is still not convinced. Vit Klemeš [98] also raised doubts in his paper about the possible presence of long memory in hydrologic time series and wondered, "By what sort of physical mechanism can the influence of, say, the mean temperature of this year at a particular geographic location be transmitted over decades and centuries?" In his opinion, in geophysics, memory should manifest itself through the Markovian property: the past influences the future only through its effects on the present. "Once a certain state of the process has been reached, it matters little for the future development how it was arrived at." He then postulated that the Hurst effect can be induced by the infinite complexity of hydrological processes, which may exhibit different statistical features across different timescales and different orders of magnitude of the output, thus making the assumption of stationarity not always suitable for hydrological time series. He further indicated the crossing theory and the broken-line process suggested by Ignacio Rodríguez-Iturbe et al. [171] as powerful tools for modeling and providing a sound physical explanation of the Hurst phenomenon.

Later, Rabindra N. Bhattacharya et al. [16] provided a clear mathematical demonstration of the existence of the Hurst effect for weakly dependent processes perturbed by small monotonic trends. This result was of significant interest. On the one hand, long memory was no longer the only theoretically grounded explanation for the Hurst effect. On the other hand, the estimation problem became very important, since even very small trends could be responsible for the Hurst phenomenon. This provided some theoretical support for Klemeš's interpretation. In a similar direction, Teverovsky and Taqqu [204] developed a variance-type estimator for H that is relatively insensitive to certain kinds of nonstationarity, including monotonic trends.

As a result, several mechanisms have been proposed to explain the Hurst phenomenon, and the debate remains open. In the literature, the observed behavior of hydrological records has been attributed to three main causes: long-range dependence, pre-asymptotic effects, and nonstationarity of the underlying process [50].

Although the original discussion arose in hydrology, the broader lesson is highly relevant for the study of dynamical systems. For the analysis developed in this thesis, the absence of a universally accepted exact interpretation is not a limitation. In systems with weak chaos, long episodes of slow evolution or intermittent motion can generate persistent behavior that differs

from the faster decorrelation typical of strongly chaotic dynamics, thereby affecting the rescaled range statistic of the orbit. For this reason, the Hurst exponent is a suitable tool for detecting weakly chaotic behavior and for quantifying the degree of persistence present in the dynamics.

4.2 The method

The Hurst exponent was introduced by H. E. Hurst [85] in 1951 to model the long-term behavior of Nile River floods. It is a statistical measure that quantifies the presence of long-term correlations in time series. One of its main advantages is that it can be computed with minimal assumptions about the underlying system, which makes it widely applicable in different contexts. Applications include financial time series [32, 40, 71, 144], biomedical signals such as electrocardiograms [102], climate data [172], and experimental measurements [103].

Several numerical methods have been proposed to estimate the Hurst exponent [225], including Detrended Fluctuation Analysis (DFA) [162], Detrended Moving Average (DMA) [2], and the Periodogram method (PM) [68]. Among these, the rescaled range (R/S) analysis is the oldest and most widely used approach [85], later popularized by Mandelbrot [139–140].

In the R/S approach, consider a time series $\vec{x} = (x_1, x_2, \ldots, x_N)$ of length N. The procedure is defined as follows:

1. Divide the time series into κ non-overlapping subseries (chunks) of length ℓ, such that $\kappa = N/\ell$. Each subseries is defined as

$$P_{k,\ell} = [x_{(k-1)\ell+1}, \ldots, x_{k\ell}], \quad k = 1, 2, \ldots, \kappa.$$

   where k indexes the subseries.

2. For each subseries, compute the mean $\mu_{k,\ell}$ and the standard deviation $S_{k,\ell}$. Then define the deviations from the mean as

$$D_{i,k,\ell} = x_{(k-1)\ell+i} - \mu_{k,\ell}, \quad i = 1, \ldots, \ell.$$

   where i indexes the elements within each subseries.

3. Construct the cumulative deviation series:

$$Z_{i,k,\ell} = \sum_{j=1}^{i} D_{j,k,\ell}, \quad i = 1, \ldots, \ell.$$

4. Compute the range of the cumulative deviations, also knows as the adjusted range:

$$R_{k,\ell} = \max_{1 \le i \le \ell} Z_{i,k,\ell} - \min_{1 \le i \le \ell} Z_{i,k,\ell}.$$

5. Calculate the rescaled range and its average over all subseries:

$$(R/S)_\ell = \left\langle \frac{R_{k,\ell}}{S_{k,\ell}} \right\rangle_k = \frac{1}{\kappa} \sum_{k=1}^{\kappa} \frac{R_{k,\ell}}{S_{k,\ell}}.$$

6. Repeat the procedure for different values of ℓ.
7. Estimate the Hurst exponent H from the scaling relation:

$$(R/S)_\ell = C\ell^H,$$

where H and C are obtained from a linear regression in log-log scale.

Although the R/S method is naturally defined for one-dimensional time series, it can be extended to two-dimensional data by modifying the construction of the subseries. In this setting, consider a sequence (X_n, Y_n), and define each subseries as

$$P_k = (X_{(k-1)\ell+1}, Y_{(k-1)\ell+1}, \ldots, X_{k\ell}, Y_{k\ell}).$$

The procedure then follows the same steps as in the one-dimensional case, with each subseries having length 2ℓ.

A schematic representation of this adapted R/S method for two-dimensional time series is shown in Fig. 4.1. For notational convenience, we define $\ell_k := (k-1)\ell$ and $\ell_K := (K-1)\ell$.

It is worth noting that alternative approaches for extending the Hurst exponent to two-dimensional data have been proposed in the literature. In particular, in the Python library *pynamicalsys* [175], the Hurst exponent is computed independently for each component of the trajectory, and the final value is defined as the average of the exponents obtained for each dimension.

4.3 Characterizing Stickiness in Hamiltonian Systems

Stickiness occurs when chaotic orbits spend long intervals near specific regions of phase space, typically around stability islands, where they become temporarily trapped and behave, for a finite time, almost as quasiperiodic orbits. This transient confinement does not change the chaotic nature of the orbit, but it strongly affects the observed dynamics. Stickiness is commonly characterized through Lyapunov exponents [43]. However, this approach has limitations: its computation requires a well-defined dynamical law, which is not always available for natural systems, and the convergence of the largest Lyapunov exponent may be slow when the orbit spends long times near trapping regions.

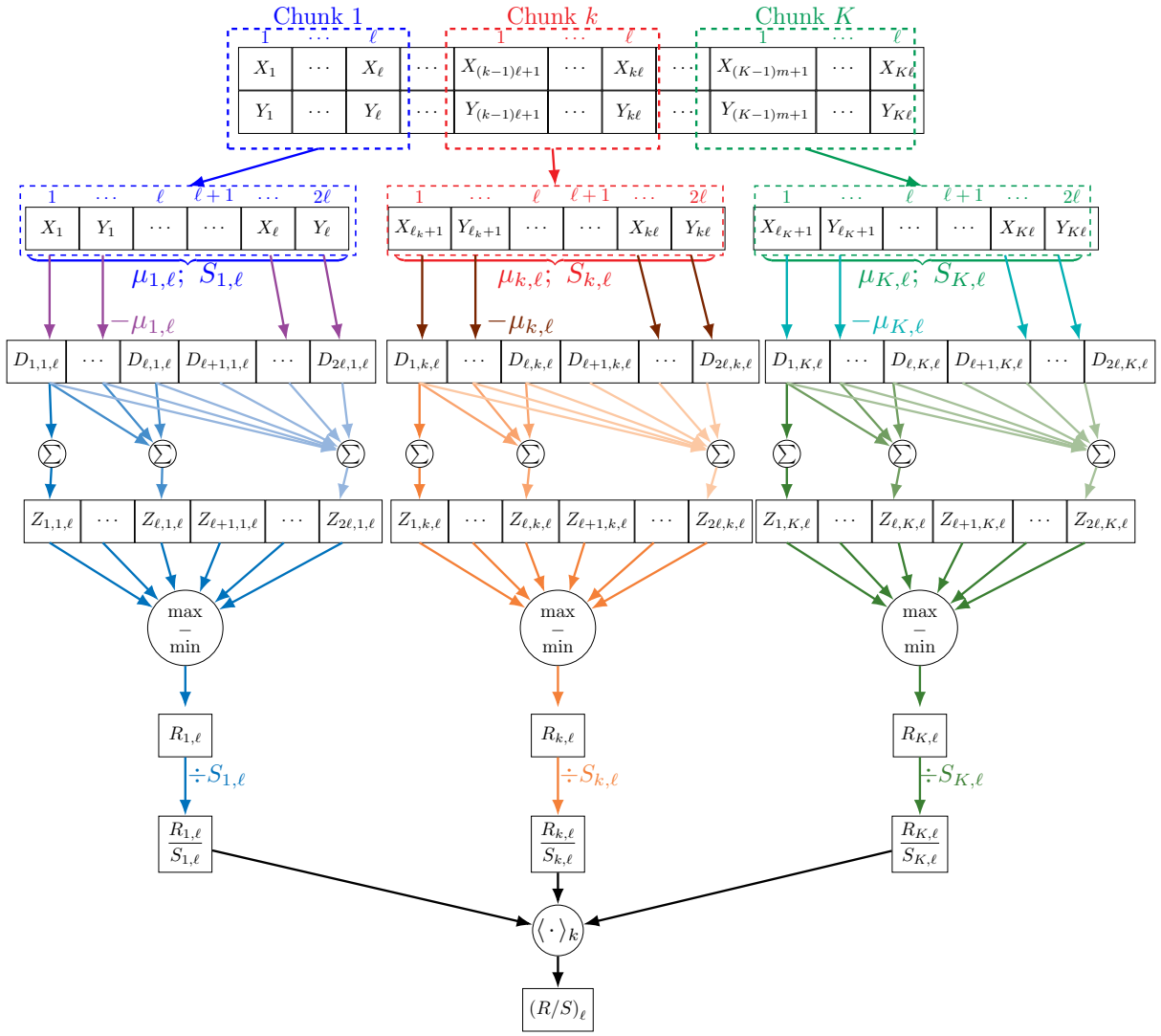


Figure 4.1 – Scheme evidencing the construction of the partition of a two-dimensional time series and the structure of the cumulative sequence for R/S analysis. Note that $\ell_k := (k-1)\ell$ and $\ell_K := (K-1)\ell$.
Source: By the author

To illustrate these ideas, we consider the Chirikov standard map [36],

$$\begin{cases} p_{n+1} = p_n - K\sin(x_n) & \mod 2\pi \\ x_{n+1} = x_n + p_{n+1} & \mod 2\pi \end{cases} \tag{4.4}$$

where K is the nonlinearity parameter and x_n and p_n denote the position and momentum at discrete time $n \in \mathbb{N}$.

The most widely used tool to characterize the dynamics of a system is the Lyapunov exponent [12, 177, 212], which measures the average exponential rate of divergence or convergence of nearby trajectories. As discussed in Section 3.2, the two-dimensional conservative map has two Lyapunov exponents, $\lambda_1 \geq \lambda_2$, with $\lambda_1 + \lambda_2 = 0$. Here, the maximum Lyapunov exponent,

$\lambda_{\max} := \lambda_1$, is used to quantify the average exponential separation rate of nearby trajectories. Chaotic trajectories exhibiting stickiness spend long periods in the vicinity of dynamical islands, which affects their average exponential separation rate and generally leads to smaller values of $\lambda_{\max}$. Thus, sticky and strongly chaotic trajectories may both exhibit positive $\lambda_{\max}$, but sticky trajectories typically yield lower values.

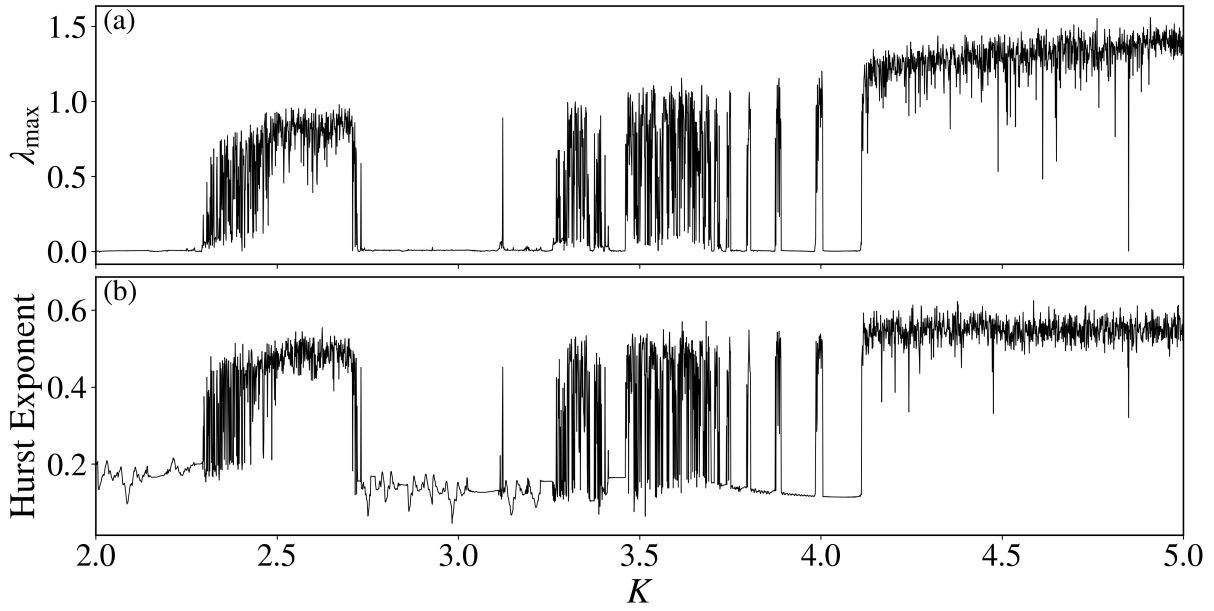


Figure 4.2 – (a) The maximum Lyapunov exponent λ_{max} and (b) the Hurst exponent H for the standard map, plotted as functions of the parameter K with the initial condition $(x_0, p_0) = (0.0, 1.3)$. Source: By the author

We now compare the maximum Lyapunov exponent with the Hurst exponent. Figure 4.2 shows $\lambda_{\max}$ and H for the standard map as functions of the nonlinearity parameter K, with the initial condition $(x_0, p_0) = (0.0, 1.3)$ iterated for $N = 2^{10} = 1024$ interations. The figure reveals windows of regularity, where $\lambda_{\max}$ is close to zero and H assumes low values. Although $\lambda_{\max}$ approaches zero more rapidly near elliptic points [135], it does not distinguish periodic from quasiperiodic motion in two-dimensional Hamiltonian systems. Another interesting aspect is observed for $K >> 4$, where the maximum Lyapunov exponent exhibits an increasing trend, whereas the Hurst exponent remains approximately constant, fluctuating around $H \approx 0.55$. This difference can be understood from the distinct properties measured by these quantities. For two-dimensional area-preserving maps, under the conditions of Pesin's theorem, the Kolmogorov-Sinai entropy is equal to the maximum Lyapunov exponent. Thus, the increase in $\lambda_{\max}$ is associated with a higher rate of information production and a faster exponential separation of nearby trajectories. In contrast, the Hurst exponent characterizes the scaling properties and

temporal correlations of the time series. Therefore, an increase in the rate of information production does not necessarily lead to a corresponding change in the Hurst exponent. The observed behavior indicates that the strength of chaotic separation increases with K, while the scaling properties quantified by H remain approximately unchanged.

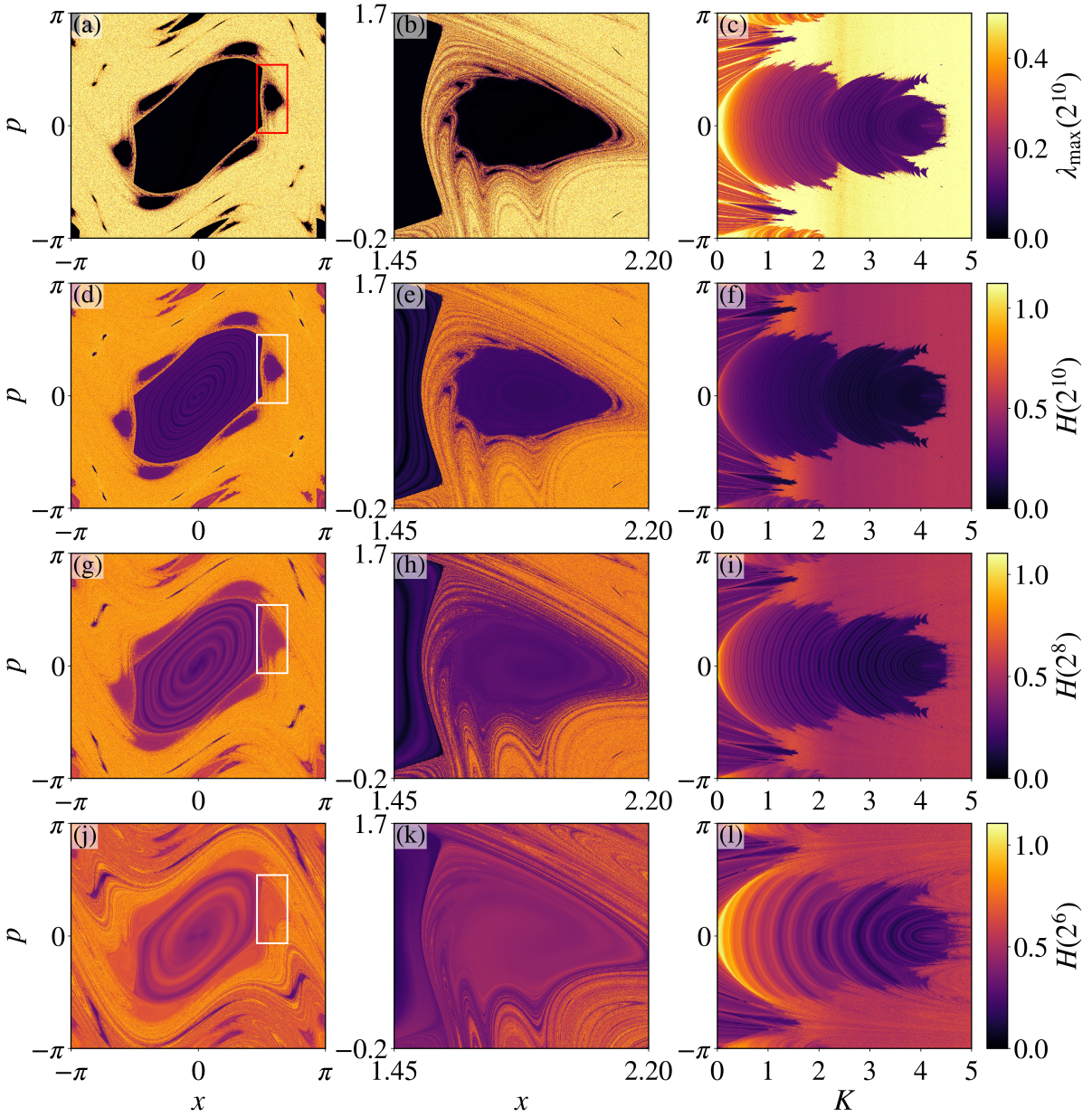


Figure 4.3 – Maximum Lyapunov exponent $\lambda_{\max}$ (a)–(c) and Hurst exponent H (d)–(f) for the standard map with $K = 1.6$, using $N = 2^{10}$ iterations. Panels (g)–(i) and (j)–(l) show the corresponding results for $N = 2^8$ and $N = 2^6$, respectively. The left column shows the results in phase space (x, p), the middle column presents magnified views of the regions marked by white rectangles in the left column, and the right column shows the corresponding results in parameter space (K, p) for $x_0 = 0$. All calculations use a $2^{10} \times 2^{10}$ grid of uniformly distributed initial conditions in phase space.
Source: By the author.

Directing our attention to the phase space, Figure 4.3(a)-(f) displays the values of λ_{max} and H for a grid of $2^{10} \times 2^{10}$ initial conditions uniformly distributed in the phase space (x, p) with $K = 1.6$, where each initial condition was iterated for $N = 2^{10} = 1024$. The figure also includes a zoom into one of the six-period satellite islands and the conservative generalized bifurcation diagram (CGBD) [42, 135].

Directing our attention to the phase space, Figure 4.3 displays the maximum Lyapunov exponent and the Hurst exponent evaluated over a grid of $2^{10} \times 2^{10}$ initial conditions uniformly distributed in the phase space (x, p), for $K = 1.6$. The calculations are performed using different time-series lengths, namely $N = 2^{10}$, 2^8, and 2^6, allowing us to examine how the number of iterations affects the identification of the main dynamical structures. The figure also includes magnified views of one of the six-period satellite islands and the conservative generalized bifurcation diagram (CGBD) [42, 135].

The Hurst exponent reproduces the main trends observed for the Lyapunov exponent and goes beyond them. In the chaotic sea, where $\lambda_{\max}$ is large, H is also large. Inside the islands, where $\lambda_{\max}$ is small, H is also reduced. In addition, in regions where the rotation number approaches a rational value, H decreases, as seen in the transition from purple to black in Figure 4.3(d), which is characteristic of trapped regions [45–46]. Figure 4.3(f) also displays the transition from regular to chaotic behavior, as well as bifurcations as K varies. The results obtained with shorter time series, shown in Figures 4.3(g)–(l), indicate that the main dynamical structures remain identifiable even when the number of iterations is reduced. However, the regions associated with low values of H become larger as the time-series length decreases. Despite this effect, the orbits crossing the main islands remain clearly distinguishable.

This behavior persists for other values of K. Figure 4.4 presents the phase-space analysis for $K = 2.5$, with a magnification of one of the four-period satellite islands. The Hurst exponent continues to distinguish the different dynamical regimes, confirming that the method remains robust for different values of the nonlinear parameter, as further illustrated in Figure 4.5.

After these analyses, it is clear that the Hurst exponent is an effective indicator for distinguishing periodicity, weak chaos, and strong chaos. It is also computationally efficient, and it provides robust results even when only short time series are available.

A different way to quantify dynamical trapping is through the finite-time Lyapunov exponent (FTLE), which has also been used to characterize stickiness in high-dimensional Hamiltonian systems [43]. Szezech et al. [191] showed that, in phase spaces with sticky regions, the

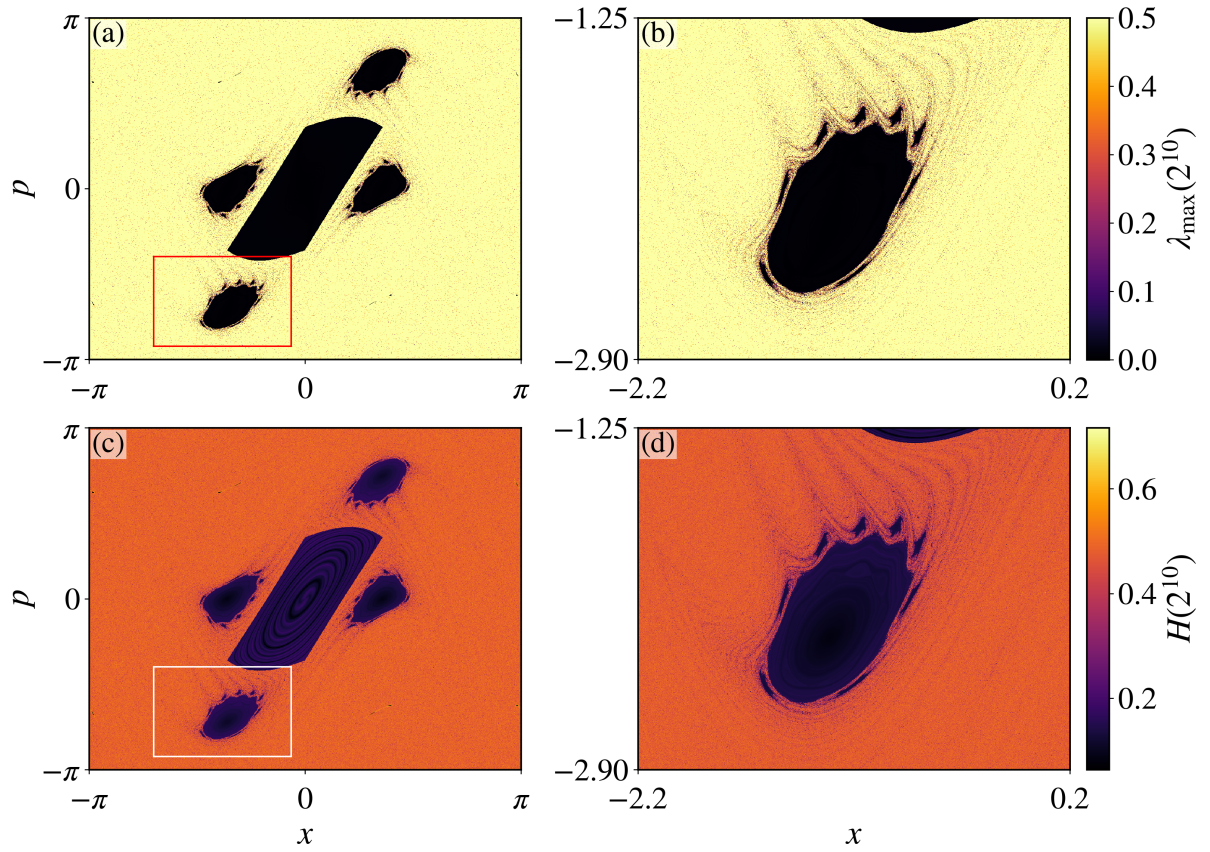


Figure 4.4 – (a) The maximum Lyapunov exponent λ_{max} and (b) the Hurst Exponent H for the standard map with $K = 2.5$, evaluated on a $2^{10} \times 2^{10}$ grid of uniformly distributed points in the phase space (x, p). Magnified views of the regions delineated by the red rectangle in (a) and white rectangle in (c), are shown in (b) and (d), respectively.
Source: By the author

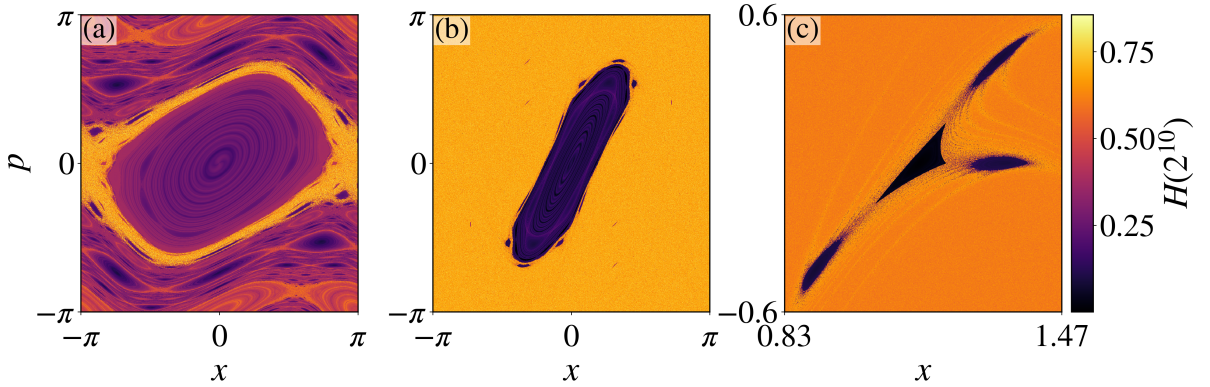


Figure 4.5 – The Hurst Exponent H for the standard map, evaluated on a $2^{10} \times 2^{10}$ grid of uniformly distributed points in the phase space (x, p) considering the nonlinear parameter as (a) $K = 0.9$, (b) $K = 3.4$ and (c) $K = 6.908745$.
Source: By the author

distribution of finite-time Lyapunov exponents is bimodal. However, Harle and Feudel [78] argued that the minor peak may actually be composed of multiple peaks, and Sales et al. [176] confirmed this behavior using recurrence time entropy.

The importance of a finite-time approach becomes clear when one follows a single chaotic orbit over long times. Although the orbit remains in the chaotic sea, it may approach periodic regions repeatedly and become trapped for long intervals before eventually returning to the chaotic sea. For this reason, finite-time analysis is essential for accurately detecting transitions between dynamical regimes along a trajectory.

To perform this analysis, an initial condition (x_0, p_0) is chosen in the chaotic sea and iterated to generate a time series of length N. This series is then divided into windows of size T, and the Hurst exponent H is computed in each window, yielding $FTH_T(N)$. An alternative procedure consists of computing H over successive time intervals of length T and restarting the orbit at the end of each window, repeating the process $M = N/T$ times. Fig. 4.6 presents a schematic representation of the finite-window procedure employed to estimate the local Hurst exponent along the trajectory.

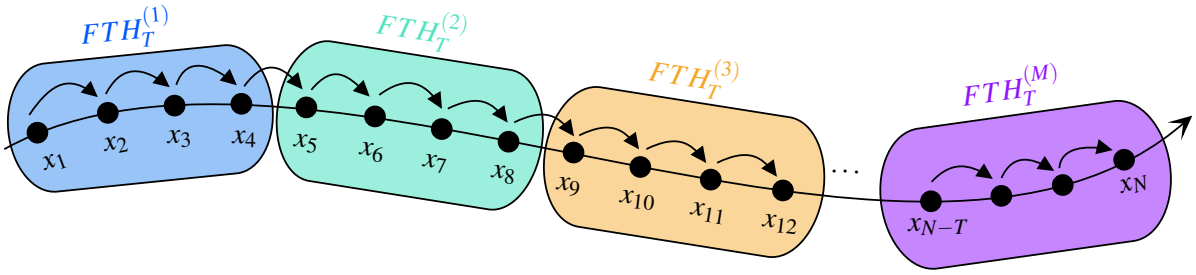


Figure 4.6 – Diagram of the finite-window method used to calculate the local Hurst exponent along a trajectory. The series $X = (x_1, \ldots, x_N)$ is divided into M segments of length T, and the finite-time Hurst exponent FTH_T is computed for each segment.
Source: By the author

The probability distribution $P(FTH_T(N))$ is obtained from a histogram of the finite-time values. Figure 4.7(a)–(c) shows this distribution for $N = 2^{30} \approx 1.074 \cdot 10^9$, the initial condition $(x_0, p_0) = (-3, 0)$, and $K = 2.5$.

Such distributions can be understood as follows: when the orbit is in the chaotic region, the distribution tends to exhibit values near the larger maximum. However, when the trajectory remains trapped for some time, small values for the Hurst exponent are registered. When the orbit is confined near an island, it may enter a deeper level within the hierarchical structure, resulting in a multi-modal distribution. Therefore, the infinite hierarchical islands-around-islands structure is responsible for the multiple small peaks in the distribution.

To identify the regions associated with these peaks, the corresponding phase-space points are plotted in Figure 4.7 using the Hurst exponent values obtained 2^6, 2^7, and 2^8 partitions (64,

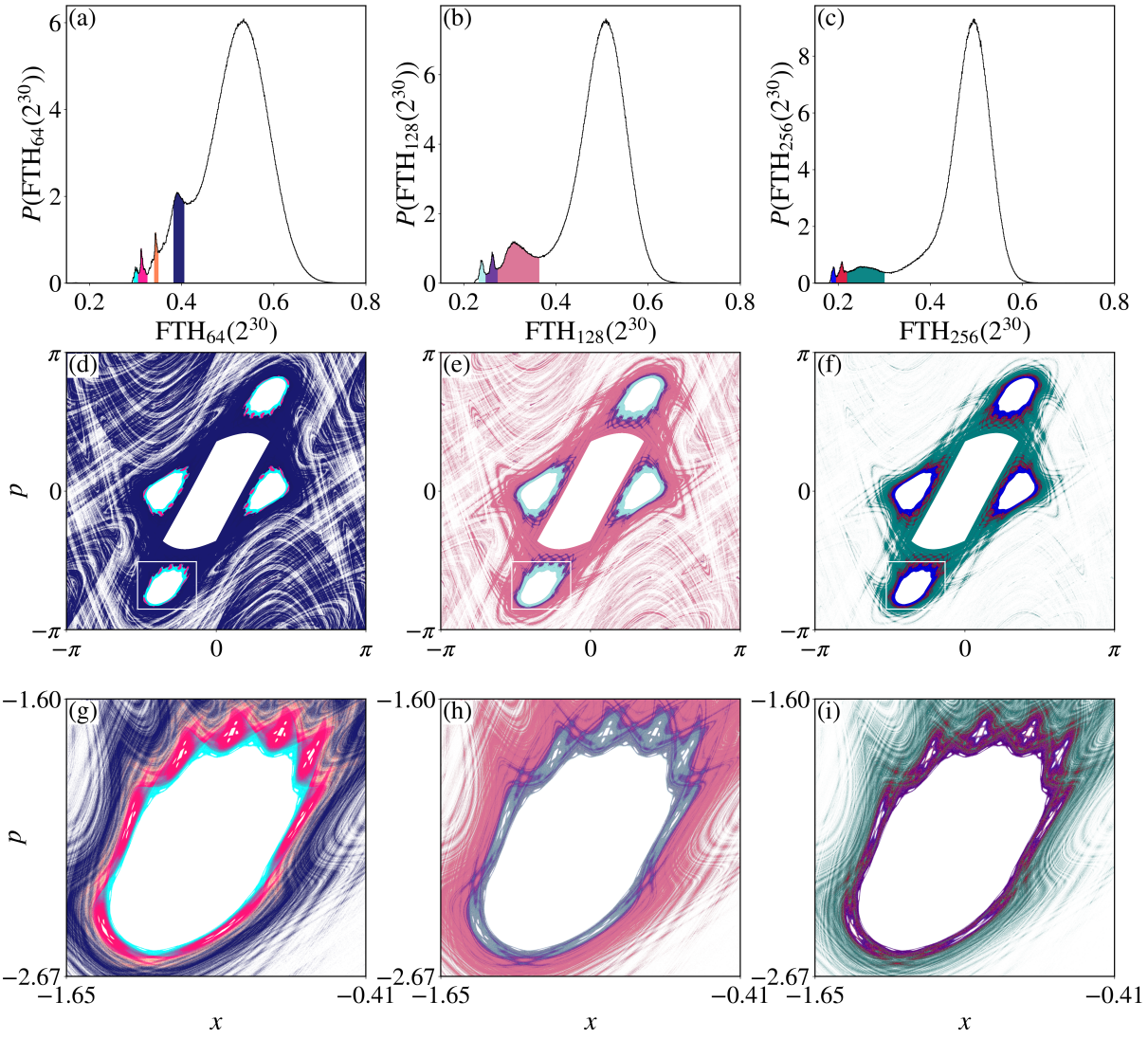


Figure 4.7 – The finite-time Hurst exponent distribution for a single chaotic orbit, with $N = 2^{30}$, $K = 2.5$, and $(x_0, y_0) = (-3, 0)$, for (a) $T = 2^6$, (b) 2^7, and (c) $T = 2^8$ partitions; (d)-(f) the phase space points that generate the minor peaks in (a)-(c), respectively; and (g)-(i) is a magnification of one of the four-period satellite islands of (d)-(f), respectively, indicated by the white rectangles. The colors in (d)-(i) match the filling colors of the distribution in (a)-(c).
Source: By the author

128, and 256, respectively). Each peak in the distribution is represented by a distinct color in phase space, revealing different hierarchical levels within structure. Note that the Figures 4.7(d)–(f) show the manifolds associated with trajectories that escape from sticky regions without being trapped [101]. These structures reveal the presence of nonhyperbolic dynamics, where tangencies between stable and unstable manifolds may prevent chaotic orbits from exploring some regions of phase space [6]. Figures 4.7(g)–(i) display the hierarchical levels around the four-period island, and the island chains remain clearly visible even when the time window is

changed.

A relevant question when using finite-time Hurst exponents is whether the results depend strongly on the total orbit length. To address this issue, Fig. 4.7(a)–(c) illustrates the FTH distribution for three distinct time windows, while Fig. 4.8 presents results for three different trajectory lengths N at a $K = 2.5$. Remarkably, the findings indicate insensitivity to the total duration of the system iteration. This behavior is expected in Hamiltonian systems, since longer trajectories increase the probability of visiting trapping regions and spending extended times near them. Nevertheless, the results exhibit a weak dependence on the chosen time window. For shorter windows, the multiple peaks become sharper and additional structures emerge, representing a finer resolution of the dynamics. For slightly larger time windows, however, these peaks become more stable and robust. Therefore, finite-time Hurst exponents provide a robust statistical description of sticky regions across phase space.

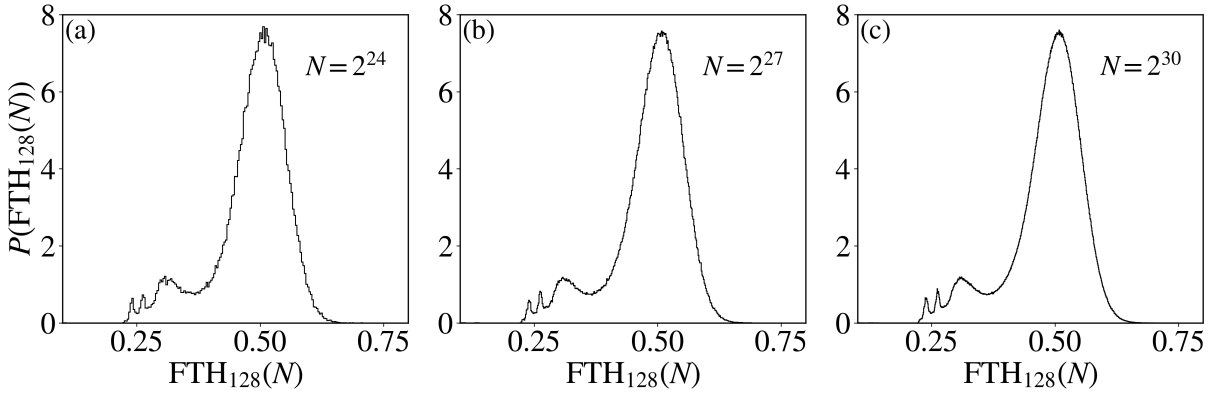


Figure 4.8 – Behavior of the finite-time Hurst exponent for different sizes of time series.
Source: By the author

To further validate the use of the Hurst exponent in the characterization of dynamical traps in Hamiltonian systems, the formalism is applied to two additional systems: the bouncer model and the kicked Harper map.

The bouncer model, previously introduced in Sec. 3.3.2, is considered here in its static-wall approximation. In this representation, the canonical variables are the particle velocity and the phase of the wall, while the periodic structure of the phase space allows the velocity to be taken modulo π [124]. The resulting map is given by [110, 124–125]:

$$\begin{cases} V_{n+1} = V_n - 2\varepsilon \sin(\phi_{n+1}) & \mod \pi \\ \phi_{n+1} = \phi_n + 2V_n & \mod 2\pi \end{cases} \tag{4.5}$$

where the dimensionless variables are defined as $\varepsilon = \varepsilon\omega^2/g$, $V_n = v_n\omega/g$ and $\phi = \omega t$. In this

context, v_n is the particle's velocity, g is the gravitational constant, and ε and ω are the amplitude and frequency of the wall's oscillation, respectively.

Applying the Hurst exponent to detect dynamical traps, Figure 4.9(a) shows the values of H for a grid of initial conditions uniformly distributed in phase space for $\varepsilon = 0.4$, with orbits iterated for $N = 2^{10} = 1024$. In the chaotic sea, H assumes high values, whereas inside the islands it takes smaller values. To quantify this behavior further, a finite-time analysis is performed for a single chaotic orbit with initial condition $(x_0, y_0) = (1,1)$, using $N = 2^{30} \approx 1.074 \cdot 10^9$ iterations and a window size $T = 128$. Figure 4.9(b) shows the distribution $P(FTH_{128}(2^{30}))$ for $\varepsilon = 0.4$. Livoratti et al. [124] reported that the corresponding finite-time Lyapunov distribution is bimodal; however, Figure 4.9(b) shows that the minor peak is actually composed of multiple peaks. Figure 4.9(c) maps these peaks to their associated phase-space regions, with each color corresponding to a different sticky structure. The results indicate that the distinct peaks in the distribution are associated with different hierarchical levels of the phase space, as revealed by the Hurst analysis.

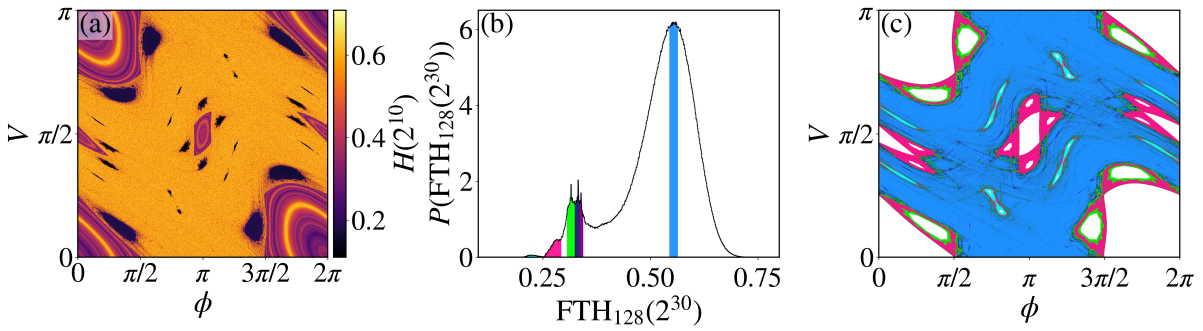


Figure 4.9 – Application of the methodology to the Bouncer map with $\varepsilon = 0.4$. In (a), the Hurst exponent is calculated on a $2^{10} \times 2^{10}$ grid of uniformly distributed points in the phase space, considering an orbit of length 2^{10}. In (b), the finite-time Hurst exponent distribution for a single chaotic orbit is shown, with $N = 2^{30}$, initial conditions $(x_0, y_0) = (1,1)$, and a time window $T = 2^7$. In (c), the phase space points associated with the colored peaks in (b) are shown.
Source: By the author

The second system considered for the validation of the proposed formalism is the kicked Harper model, previously introduced in Sec. 3.3.3. Here, we consider its two-dimensional area-preserving map, given by [118]

$$\begin{cases} v_{n+1} = v_n - 2\gamma \sin(u_n), \\ u_{n+1} = u_n + 2\gamma \sin(v_{n+1}) \end{cases} \tag{4.6}$$

where u and v are the dimensionless momentum and position, and γ is the kick strength.

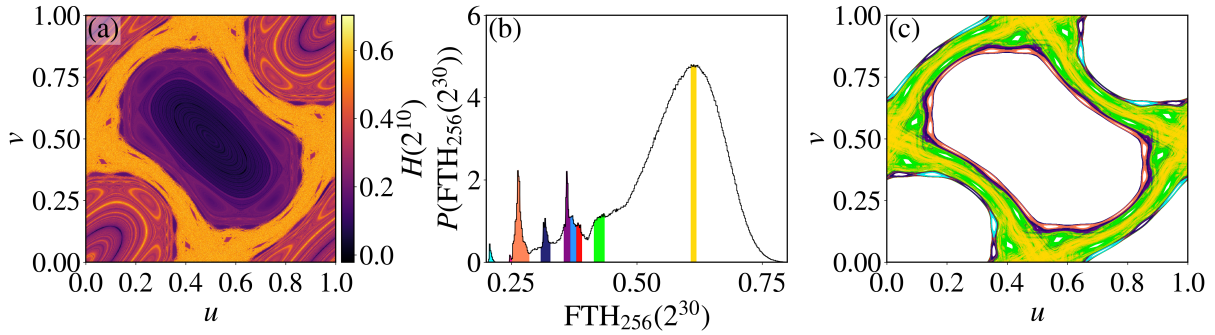


Figure 4.10 – Analysis of stickiness in the Kicked Harper map with $\gamma = 0.25$. In (a), the Hurst exponent is evaluated on a $2^{10} \times 2^{10}$ grid of initial conditions in phase space, using an orbit length of 2^{10}. In (b), the distribution of the finite-time Hurst exponent for a single chaotic trajectory is shown, with $N = 2^{30}$, initial conditions $(x_0, y_0) = (0.5, 0.1)$, and a time window $T = 2^8$. In (c), the phase space points responsible for the colored peaks in the distribution from (b) are depicted.
Source: By the author

Performing a Hurst Exponent analysis to detect dynamical traps, Figure 4.10-(a) illustrates the values of H across a grid of initial conditions uniformly distributed within the phase space for $\gamma = 0.25$, with orbits iterated up to $N = 2^{10} = 1024$. As in the previous examples, H is larger in chaotic regions and smaller inside the islands. To study this behavior in finite time, a single chaotic orbit with initial condition $(x_0, y_0) = (0.5, 0.1)$ is considered, with $N = 2^{30} \approx 1.074 \cdot 10^9$ iterations and a time window $T = 256$. Figure 4.10-(b) presents the probability distribution $P(FTH_{256}(2^{30}))$ for $\gamma = 0.25$ reveal a multi-modal distribution where the largest maximum corresponding to chaotic sea regions and the different minor peaks are due to the hierarchical islands-around-islands structure embedded in the phase space. Figure 4.10-(c) correlates these multiple peaks with specific regions in the phase space, each represented by a different color. Note that the area in the distribution represented by the green points indicates chaotic orbits that are restricted from accessing specific regions due to the tangency of stable and unstable manifolds. [192]. This peak reflects the influence of these manifolds. The yellow regions, on the other hand, represent the chaotic seas that exist among the islands. Additionally, the other smaller peaks correspond to various hierarchical levels around the islands.

4.4 Characterizing Weak Chaos in Fractional Dynamics

Fractional dynamical systems (FDS) are a class of systems governed by fractional differential or difference equations (FDEs), which incorporate derivatives or differences of non-integer order in time [111, 130, 206]. In recent years, the study of nonlinear fractional dynamical systems has advanced significantly[49, 55–56, 95, 129, 169]. Many of these studies are based on fractional

maps that describe periodically kicked systems [153, 156, 194–195, 199–201].

A characteristic property of fractional systems is the presence of memory effects, which can lead to unusual dynamical features [53–54, 57]. As a consequence, trajectories may intersect in the projected phase space, and attractors may overlap in this representation.[1] Furthermore, attractors may exist only in an asymptotic sense, with limiting points that do not necessarily belong to their basins of attraction. In this context, fractional systems exhibit a special type of behavior known as cascade of bifurcations type trajectories (CBTT) [53]. In a CBTT, a sequence of bifurcations occurs not as a result of parameter variation, as in classical dynamical systems, but along a single trajectory during its temporal evolution. During certain time intervals, the trajectory becomes confined to progressively smaller regions of phase space, as if it were temporarily trapped. It may subsequently leave these regions and explore a larger portion of phase space, repeating this process several times. This intermittent behavior is analogous to the stickiness effect [1, 4–5, 39, 41, 145, 179, 218], also referred to as weak chaos, which is one of the main features of two-dimensional area-preserving maps. As discussed in Section 4.2, the Hurst exponent provides an effective way to characterize this type of trapping behavior.

This section extends the use of the Hurst exponent to provide a refined characterization of CBTT in fractional systems. The approach is applied to a generalization of the standard map that incorporates the Riemann–Liouville fractional derivative into the equations of motion.

4.4.1 The Riemann-Liouville fractional standard map and CBTT

The standard map, also known as the Chirikov-Taylor map or the kicked rotator map, is a two-dimensional area-preserving map introduced independently by Bryan Taylor [202] and Boris Chirikov [36]. It is written as

$$\begin{aligned} p_{n+1} &= p_n - K\sin x_n, \\ x_{n+1} &= x_n + p_{n+1} \qquad \mod 2\pi, \end{aligned} \tag{4.7}$$

where x_n and p_n are the canonical position and momentum at discrete times $n = 1, 2, \ldots, N$, and K controls the nonlinearity of the map. As seen in Sec. 3.3.1, this map represents the Poincaré surface of section of the kicked rotator, where x_n and p_n denote the angular position and angular

[1] In fractional systems, the evolution depends on the entire history of the system rather than only on its instantaneous coordinates. Therefore, the usual phase-space representation, constructed from the instantaneous variables, does not fully describe the system's state and can be regarded as a projection of a higher-dimensional, history-dependent state space. Consequently, distinct trajectories or invariant structures may appear to overlap in this projected representation, even when they correspond to different states in the complete description of the system.

momentum, respectively, while K quantifies the intensity of the periodic kicks applied to the rotator [116, 222], with the corresponding differential equation given by

$$\ddot{x} + K\sin(x)\sum_{n=0}^{\infty}\delta\Big(t-n\Big) = 0, \tag{4.8}$$

and the map in Eq. (4.7) is obtained by considering the variables just after the nth kick.

In the standard map, the next iteration depends only on the current state. This limits its ability to describe systems with a strong dependence on past states. To overcome this limitation, fractional differential equations (FDEs) [97, 146] have been employed. These equations generalize the usual differential-equation framework by incorporating fractional derivatives, which account for memory effects and nonlocal interactions [18, 196–198]. This framework has been used in several areas, including biology [92, 134], electrodynamics [148, 183–184, 186–187], and quantum mechanics [10, 105–106, 121].

To obtain a fractional equation of motion for the kicked rotator, the second-order time derivative in Eq. (4.8) is replaced by the Riemann–Liouville derivative ${}_0D_t^{\alpha}$ [97, 146], yielding

$${}_0D_t^{\alpha}x + K\sin(x)\sum_{n=0}^{\infty}\delta\Big(t-n\Big) = 0, \tag{4.9}$$

where

$${}_0D_t^{\alpha}x(t) = \frac{1}{\Gamma(2-\alpha)}\frac{\mathrm{d}^2}{\mathrm{d}t^2}\int_0^t \frac{x(\tau)}{(t-\tau)^{\alpha-1}}\mathrm{d}\tau. \tag{4.10}$$

By integrating Eq. (4.9) with $\alpha \in (1,2]$, the Riemann–Liouville fractional standard map (RLFSM) is obtained [52, 59]:

$$\begin{aligned} p_{n+1} &= p_n - K\sin x_n, \\ x_{n+1} &= \frac{1}{\Gamma(\alpha)}\sum_{i=0}^{n} p_{i+1}V_{\alpha}(n-i+1) \mod 2\pi, \end{aligned} \tag{4.11}$$

where

$$V_{\alpha}(m) = m^{\alpha-1} - (m-1)^{\alpha-1}. \tag{4.12}$$

In the limiting case $\alpha = 2$, the RLFSM reduces to the standard map under the condition $x_0 = 0$. For $\alpha < 2$, however, memory effects begin to emerge in the system and modify the dynamics.

To investigate the influence of α on the RLFSM, the phase space of the model is analyzed for several values of α and K in Figure 4.11. For $\alpha = 2$ and $K = 2$ [Figure 4.11(a)], the phase space coincides with that of the standard map. The central stability island is surrounded by smaller islands, and all regular structures are embedded in the chaotic sea. For values of α

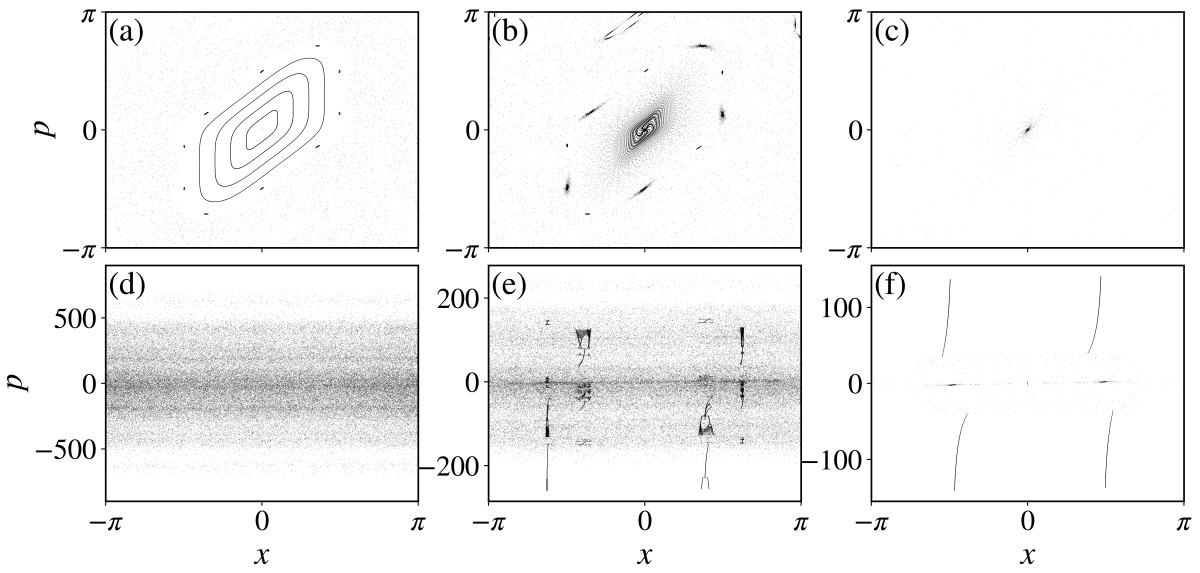


Figure 4.11 – Phase space of the RLFSM for the first 5000 iterations of 20 initial conditions, uniformly distributed along $x = 0$ and $p \in [-\pi, \pi]$, with fixed $K = 2$ for (a) $\alpha = 2$, (b) $\alpha = 1.999$, and (c) $\alpha = 1.9$; and with fixed $\alpha = 1.65$ for (d) $K = 7$, (e) $K = 4.5$, and (f) $K = 4$.
Source: By the author

close to, but different from, 2 [Figures 4.11(b) and 4.11(c)], the effect of α is similar to a weak damping in the standard map [63]: the centers of the islands become attracting periodic orbits. For smaller values such as $\alpha = 1.65$ [Figures 4.11(d)–4.11(f)], different values of K produce qualitatively distinct behaviors. Edelman and collaborators [53–54, 57–58] have shown that the RLFSM can generate attracting asymptotically periodic orbits, attracting slow-diverging trajectories, attracting accelerator-mode trajectories, and chaotic attractors. They also identified a characteristic type of trajectory known as a cascade of bifurcations type trajectory (CBTT) [Figure 4.11(e)].

Figure 4.12 shows an example of an intermittent CBTT for the initial condition $(x_0, p_0) = (0.0, 0.3)$ after 10^5 iterations with $\alpha = 1.65$ and $K = 4.5$. This type of trajectory behaves similarly to a typical chaotic orbit in a two-dimensional area-preserving map, but it intermittently becomes confined to a specific region of phase space where it behaves in a less chaotic manner. In this sense, the largest Lyapunov exponent [191] and the Hurst exponent [20] decrease, for example. The term weak chaos is therefore appropriate, since the orbit exhibits a trapping-like behavior analogous to the stickiness effect observed in Hamiltonian maps. In the fractional setting, however, these trappings occur over specific time intervals, and the portion of phase space occupied by the orbit becomes significantly smaller during those intervals.

In the next section, the Hurst exponent is used to characterize the dynamics of orbits that

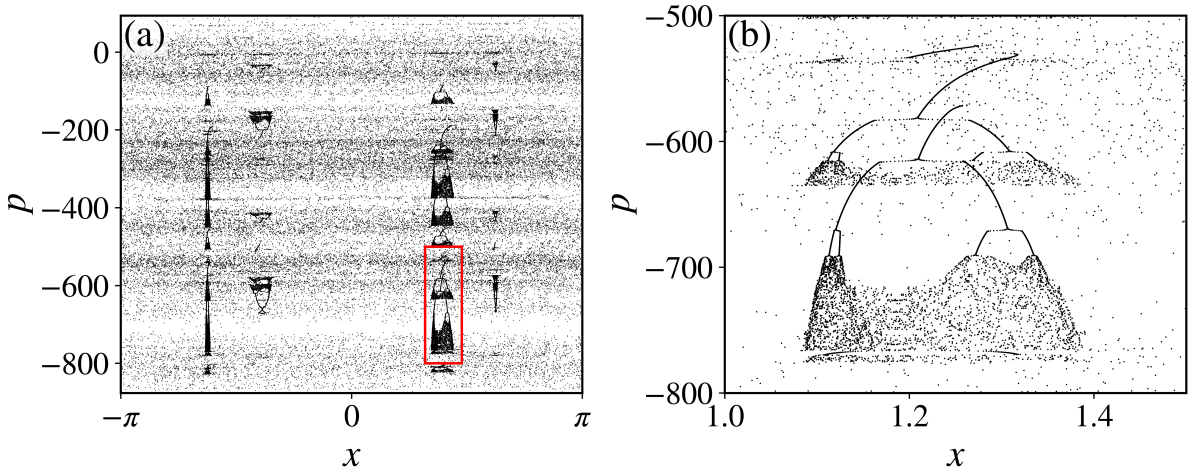


Figure 4.12 – The RLFSM phase space for $K = 4.5$ and $\alpha = 1.65$, considering 10^5 iterations of a single trajectory with $(x_0, p_0) = (0, 0.3)$. (b) Magnification of one CBTT region indicated by the red rectangle in (a).
Source: By the author

follow a CBTT.

4.4.2 Quantifying the CBTT

A dynamical trap is a region in phase space where an orbit can remain for arbitrarily long finite times, behaving similarly to a quasiperiodic orbit even though the global motion remains chaotic [219]. This leads to the stickiness effect, which is commonly characterized using Lyapunov exponents [43, 152, 191]. In fractional systems, however, the calculation of Lyapunov exponents requires an extension of the Jacobian formalism to include fractional derivatives and memory effects [114, 214].

As discussed in Section 4.2, the Hurst exponent provides an alternative approach for detecting dynamical trapping, since it relies only on the time series of the system and does not require knowledge of the equations of motion. Based on these considerations, the Hurst exponent becomes a natural candidate for the analysis of cascade of bifurcations type trajectories (CBTT) in fractional maps. In particular, its ability to capture changes in the temporal correlations of a trajectory makes it well suited to detect transitions between strongly chaotic, weakly chaotic, and nearly periodic behavior along a single orbit.

A commonly used technique in these methods is finite-time analysis, which provides precise detection of transitions between different dynamical regimes in the orbit. The procedure begins by choosing an initial condition (x_0, p_0) and iterating it to generate a time series of length N. The time series is then divided into windows of size T, and the quantifier of interest is computed

in each window.

The following analysis is performed to quantify CBTTs along a single trajectory of the RLFSM [Eq. (4.11)] using the time series of the variable x. An orbit with initial condition $(x_0, p_0) = (0, 0.3)$ and length $N = 10^5$ [as in Fig. 4.12] is considered, and the corresponding time series of x is shown in Fig. 4.14(a). The series $X = (x_1, \ldots, x_N)$ is divided into $M = 2^{12}$ partitions. For the ith window, the first and last elements correspond to iT and $(i+1)T$, respectively. The midpoint of each window is given by

$$n_{\text{mid}}^{(i)} = \frac{(i+1)T + iT}{2} = \left(i + \frac{1}{2}\right) T, \tag{4.13}$$

and the Hurst exponent H^i is computed for that window. This process is repeated across all partitions and is illustrated schematically in Fig. 4.13.

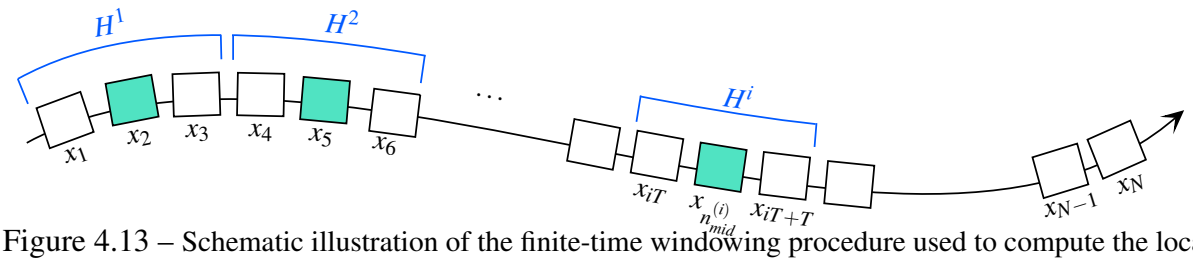


Figure 4.13 – Schematic illustration of the finite-time windowing procedure used to compute the local Hurst exponent along a trajectory. The time series $X = (x_1, \ldots, x_N)$ is partitioned into windows of length T. For the ith window, the interval spans from x_{iT} to $x_{(i+1)T}$, and its midpoint is $x_{n_{\text{mid}}^{(i)}}$, shown in teal. The Hurst exponent $H^{(i)}$ is evaluated within each window, producing a sequence of finite-time estimates associated with the corresponding midpoints. Source: By the author

The resulting finite-time Hurst exponent as a function of the midpoint n_{mid} is shown in Fig. 4.14(b). The intermittent nature of the CBTT becomes clear in the time series of x [Fig. 4.14(a)], where the orbit changes abruptly from strong chaotic motion, in which it fills the full x domain, to apparently periodic motion, and then to weaker chaotic motion, where the orbit occupies a smaller region before becoming strongly chaotic again. The transition from periodic to weakly chaotic dynamics resembles the period-doubling route to chaos observed in dissipative systems such as the logistic map.

During the chaotic regime, the Hurst exponent [Fig. 4.14(b)] takes larger values. In contrast, when the orbit enters the periodic-like regime, the quantifier drops sharply toward zero. After this period-doubling-like stage, the orbit reaches a weakly chaotic regime, in which the Hurst exponent is larger than in the periodic regime but smaller than in the strongly chaotic regime. Therefore, the Hurst exponent successfully identifies the intermittent behavior and captures the

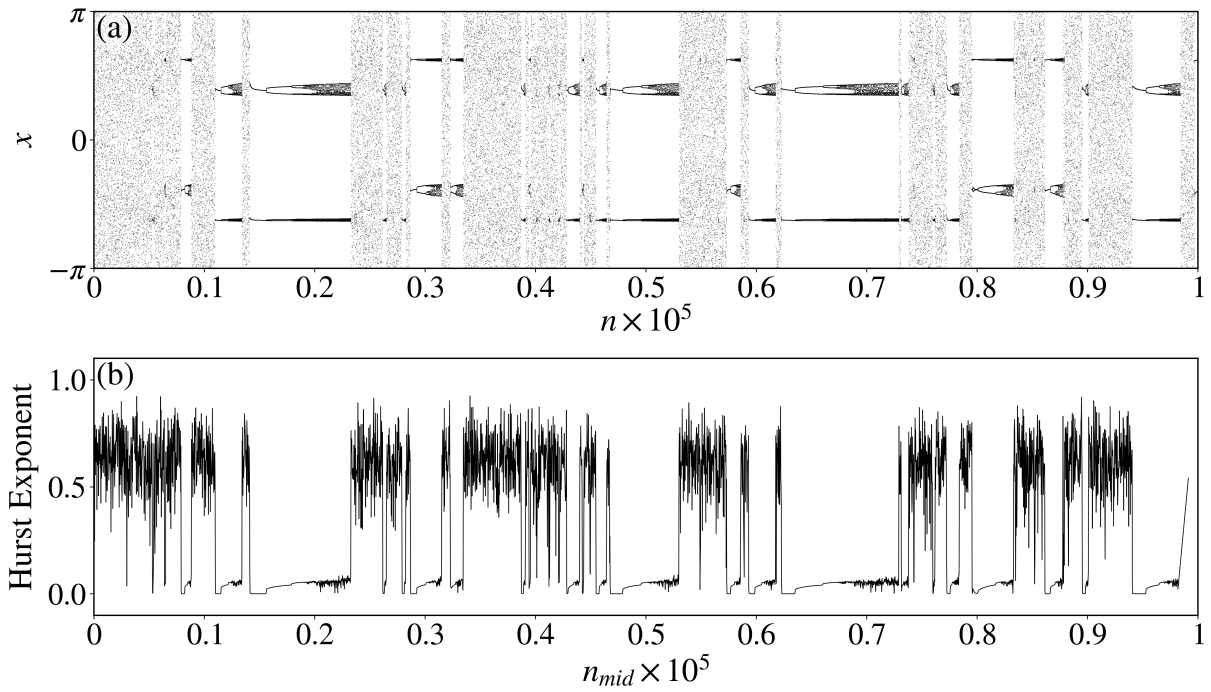


Figure 4.14 – (a) Time series of the variable x for the trajectory shown in Fig. 4.12. (b) Hurst exponent as a function of the midpoint of each window.
Source: By the author

weak-chaos-like intervals associated with CBTT, when the orbit occupies a much smaller region in x than in the strongly chaotic regime.

Since finite-time results depend on the chosen window size, it is important to examine how the window length affects the analysis. Figures 4.15(a)–4.15(c) show the finite-time Hurst exponent for 2^8, 2^{10}, and 2^{12} partitions, respectively. The results show that the distinction between chaotic and CBTT regimes remains robust across these different choices. As expected, smaller windows introduce more noise, since the quantifier becomes less stable when applied to shorter data sets. Even so, the Hurst exponent remains a reliable measure for identifying weak chaos in area-preserving dynamical systems and provides a meaningful statistical description of the CBTT effect.

To locate where the trapping occurs in phase space, the finite-time analysis described above is performed and each point is colored according to the finite-time Hurst exponent associated with its window [Fig. 4.16(a)]. In the adopted color scale, black corresponds to periodic dynamics, blue to yellow corresponds to chaotic dynamics, and red identifies weak chaotic dynamics, that is, the CBTT regime. During the CBTT intervals, the Hurst exponent values and colors are clearly distinct from those observed in the large chaotic regions. This representation reveals the cascading character of the dynamics and provides a detailed visual description of the trapping

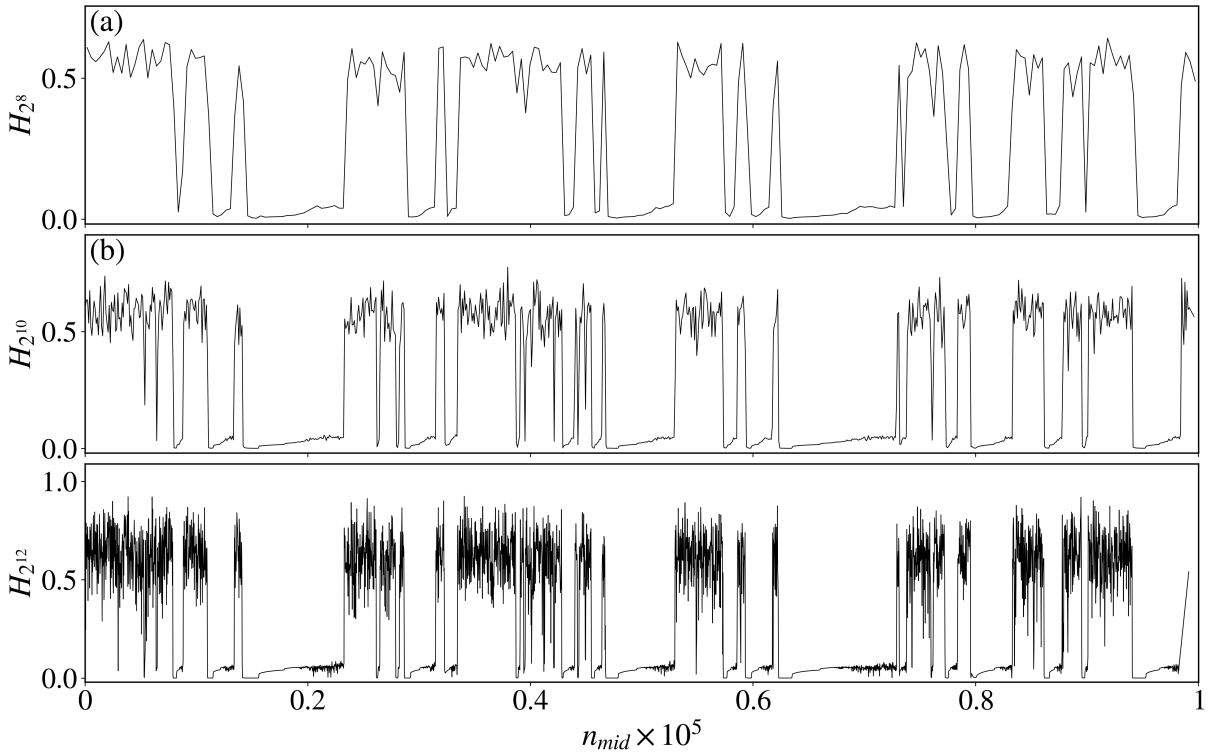


Figure 4.15 – Finite-time Hurst exponent for (a) 2^8, (b) 2^{10}, and (c) 2^{12} partitions.
Source: By the author

regions.

In dynamical systems exhibiting the stickiness effect, transitions from fully chaotic motion to different hierarchical levels in the islands-around-islands structure lead to finite-time distributions of the Hurst exponent [20] with multiple peaks. Figure 4.16(b) shows that fractional dynamics also produce multimodal distributions. To compute these distributions, a finite-time analysis of H is performed along the evolution of 10^3 chaotic orbits of length $N = 10^5$, with initial conditions chosen on the line $x = 0$ and $p \in (-\pi, \pi)$. We use $M = 2^{12}$ partitions in the x coordinate. From the values of H_M, the probability distributions $P(H_M)$ are constructed by means of frequency histograms.

The Hurst distribution $P(H_{2^8})$ [Fig. 4.16(b)] exhibits three main peaks. When the orbit lies in the chaotic region, the distribution concentrates around the largest values of H_{2^8}. When the trajectory enters the CBTT regime, a second peak appears at intermediate values. Finally, when the dynamics become periodic, the Hurst exponent takes values associated with the smallest peak, located closest to zero.

In this chapter, we have demonstrated the power and versatility of the Hurst exponent as a tool for characterizing chaotic dynamics, particularly in the elusive regime of weak chaos. We

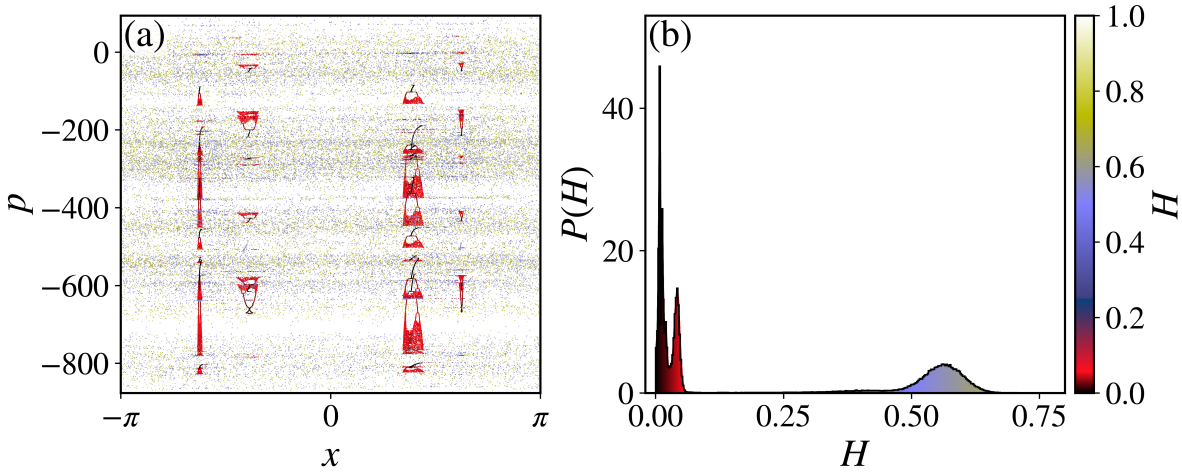


Figure 4.16 – (a) Single trajectory shown in Fig. 4.12, colored according to the finite-time Hurst exponent in the corresponding time window. (b) Probability distributions of the finite-time Hurst exponent computed with $M = 2^{12}$ partitions along the x coordinate for 10^3 chaotic orbits of length $N = 10^5$, with initial conditions on the line $x = 0$ and $p \in (-\pi, \pi)$ for the RLFSM with $K = 4.5$ and $\alpha = 1.65$. Both distributions exhibit multiple peaks, reflecting transitions between chaotic, CBTT, and periodic regimes.
Source: By the author

began by revisiting the origins of the Hurst exponent in hydrological studies and its subsequent development as a measure of long-term dependence in time series. We then adapted the classical R/S analysis to two-dimensional, discrete-time dynamical systems.

Our comparison with the Lyapunov exponent showed that, although both indicators can distinguish regular from chaotic motion, the Hurst exponent provides a more detailed view of the underlying dynamics. In particular, through finite-time Hurst analysis, we found that the probability distribution of H is not simply bimodal, as has been reported for Lyapunov exponents, but can exhibit multiple distinct peaks. Our results indicate that these peaks are associated with different hierarchical levels of the complex, self-similar "islands-around-islands" structure of phase space. This behavior was observed consistently in several Hamiltonian systems, including the standard map, the bouncer model, and the kicked Harper map.

We further extended the FTH approach to fractional dynamical systems, where the definition and interpretation of Lyapunov exponents become particularly challenging because of memory effects. For the Riemann–Liouville fractional standard map, the FTH analysis allowed us to identify and quantify the intermittent dynamics of Cascade of Bifurcations Type Trajectories (CBTT), clearly distinguishing their strongly chaotic, weakly chaotic, and periodic-like phases.

Taken together, these results show that the Hurst exponent is not simply an alternative to the Lyapunov exponent. In several situations, it provides a more practical and informative way

to characterize complex dynamics in both Hamiltonian and fractional systems. Its statistical behavior offers valuable information about the hierarchical organization of phase space, while its reliance only on time-series data makes it especially useful for experimental systems in which the underlying governing equations are unknown. Thus, the Hurst exponent provides a promising and accessible approach for investigating complex dynamical behavior across a broad range of systems.

CHAPTER

5 Conclusion

We have reached the end of our journey, dear reader. Throughout this thesis, we have investigated the use of the Hurst exponent as a tool to characterize weak chaos in Hamiltonian systems, with particular emphasis on its ability to detect dynamical traps such as stickiness and cascade of bifurcations type trajectories (CBTT). The central motivation arose from the limitations of traditional chaos indicators, most notably the Lyapunov exponent, which, while effective in distinguishing regular from strongly chaotic motion, converges slowly in the presence of stickiness and requires knowledge of the system's equations of motion.

We began by reviewing the fundamental concepts of Hamiltonian dynamics and the characterization of chaos, introducing the Lyapunov exponent as the standard measure of sensitivity to initial conditions. Through numerical experiments with the standard map, the bouncer model, and the kicked Harper map, we demonstrated that chaotic orbits near regular islands exhibit long transient periods during which the largest Lyapunov exponent remains close to zero, thereby masking their chaotic nature. This intermittent behavior, known as stickiness, leads to anomalous transport and algebraic decay of correlations, properties that define weakly chaotic systems.

In response to these challenges, we introduced the Hurst exponent, originally developed in hydrology by Harold Hurst to quantify long-range dependence in time series. Unlike the Lyapunov exponent, the Hurst exponent is computed solely from the time series of the system, requiring no knowledge of the underlying equations. We showed that for regular motion, the Hurst exponent assumes low values, while for strongly chaotic motion it becomes significantly larger. More importantly, in regions of stickiness, the Hurst exponent captures the reduced persistence associated with temporary trapping near islands.

A key contribution of this work was the extension to finite-time analysis. By computing the finite-time Hurst exponent (FTH) over sliding windows along a single chaotic orbit, we obtained

probability distributions that are multimodal. Each peak in the distribution corresponds to a distinct hierarchical level of the islands-around-islands structure, revealing the nested organization of phase space. This result goes beyond what is achievable with finite-time Lyapunov exponents, which typically yield only bimodal distributions. We further validated this methodology across the three Hamiltonian maps, confirming its robustness with respect to both the total orbit length and the choice of window size.

We then extended the Hurst exponent analysis to fractional dynamical systems, specifically the Riemann-Liouville fractional standard map (RLFSM). Fractional systems exhibit memory effects that give rise to a unique type of dynamical trap known as the cascade of bifurcations type trajectory (CBTT). In a CBTT, a single trajectory undergoes a sequence of bifurcations during its temporal evolution, alternating between strongly chaotic, weakly chaotic, and periodic-like regimes. By applying the finite-time Hurst exponent to such trajectories, we were able to identify these transitions quantitatively: strongly chaotic intervals yield high Hurst values, periodic intervals yield values near zero, and CBTT intervals produce intermediate values. The resulting distributions again exhibited multiple peaks, corresponding to the different dynamical regimes visited by the trajectory. This analysis demonstrated that the Hurst exponent is equally effective in fractional systems, where the definition of Lyapunov exponents is complicated by memory effects.

The research presented in this thesis has been published in peer-reviewed journals, including Physical Review E [20], Chaos, Solitons & Fractals [27], attesting to the validity and impact of our findings. The Python toolkit pynamicalsys [175], developed as part of this work, makes these methods freely available to the scientific community. Throughout the full period of the doctorate, we also developed several other studies, resulting in additional publications [18, 20–27, 123, 173–175] (see Appendix A).

In summary, we have established the Hurst exponent as a practical, robust, and computationally efficient indicator for characterizing weak chaos. Its ability to operate on time series alone, to distinguish regular, weakly chaotic, and strongly chaotic motion, and to reveal the hierarchical structure of phase space through finite-time analysis makes it a valuable addition to the nonlinear dynamicist's toolbox. Future work may extend this approach to higher-dimensional systems, to experimental time series from natural or laboratory systems, to other fractional maps where memory effects play a central role, as well as to billiard and dissipative systems. These directions remain open for further investigation.

APPENDIX A
Published Papers

The scientific articles published throughout the PhD are listed below, from the most recent to the oldest.

[13] D. Borin and D. F. M. Oliveira *Self-similar shrimp structures and bifurcation hierarchies in the Gumowski–Mira map*, Physica A: Statistical Mechanics and its Applications **700**, 131892 (2026). DOI: `https://doi.org/10.1016/j.physa.2026.131892`

Physica A 700 (2026) 131892

Contents lists available at ScienceDirect

Physica A

journal homepage: www.elsevier.com/locate/physa

Self-similar shrimp structures and bifurcation hierarchies in the Gumowski–Mira map

Daniel Borin [a,b,*], Diego F.M. Oliveira [a]

[a] University of North Dakota, School of Electrical Engineering and Computer Science, Grand Forks, ND 58202, USA
[b] São Paulo State University (UNESP), IGCE - Physics Department, 13506-900, Rio Claro, SP, Brazil

ARTICLE INFO

Dataset link: https://gumowskimira.streamlit.app

ABSTRACT

Mainly related to the aesthetic complexity of its attractors, the Gumowski–Mira map has attracted long-standing interest in nonlinear dynamics. Although the Gumowski–Mira map has been extensively studied in terms of its attractor properties, its global organization in the two-parameter space, including the arrangement and hierarchical organization of different stability structures associated with periodic and chaotic dynamics, has not been systematically investigated. In this work, we investigate the two-parameter space of the Gumowski–Mira map by combining Lyapunov exponent calculations with a systematic identification of the attractor period. We identify shrimp-shaped stability regions composed of a main periodic core followed by cascades of period-doubling bifurcations leading to chaos. Stability regions with irregularly shaped geometries but identical internal bifurcation organization are also observed. In addition, tongue-like periodic domains organized along paths of increasing period are detected. Both monotonic period-adding sequences and sequences involving skipped tongues are found, indicating that different mechanisms of period organization coexist.

1. Introduction

Nonlinear dynamical systems are extensively used to model countless phenomena across diverse scientific and technological domains, exhibiting a rich spectrum of dynamic states that range from steady states and regular (periodic or quasi-periodic) oscillations to chaotic fluctuations [1]. To obtain a comprehensive perspective of the long-range dynamics of systems and transitional structures and cascades that go beyond the scope of traditional single-parameter analysis, the exploration of two-parameter spaces is essential. This approach, which involves the simultaneous variation of two control parameters, allows for the use of tools such as isoperiodic diagrams and Lyapunov exponents to monitor and discriminate dynamic behaviors.

In the context of two-parameter space analysis, regions of regularity frequently emerge as islands within chaotic regimes. Among these structures, the term "shrimp" was coined by J. A. C. Gallas in 1993, while investigating the parameter space of the Hénon map [2], to describe stability islands with a characteristic shape, consisting of a central head and four narrow antennae [3–7]. The shrimp typically arises from the intersection of two parabolic arcs of superposition and has two distinct bifurcation lines surrounding the arcs [8]. Although it was only coined as a shrimp in 1993, these structures began to appear in the early 1980s [9–11] and were given various names, such as the fishbook [12], swallow [13], crossroads [14], and compound window [15].

The study of these structures is crucial for understanding the complex behavior of systems, as they represent regions of regularity (periodic or quasi-periodic oscillations) embedded within a chaotic sea. While periodic shrimps are the most prevalent and

* Corresponding author.
E-mail address: d.borin@hotmail.com (D. Borin).
URL: https://danielborin.github.io/ (D. Borin).

https://doi.org/10.1016/j.physa.2026.131892
Received 28 May 2026; Received in revised form 9 July 2026
Available online 11 August 2026
0378-4371/© 2026 Published by Elsevier B.V.

[12] D. Borin, E. D. Leonel, and D. F. M. de Oliveira *Survival probability of particles inside the lemon billiard*, Physical Review E **114**, 014224 (2026). DOI: `https://doi.org/10.1103/md5j-ggyd`

Survival probability of particles inside the lemon billiard

Daniel Borin [1,2] Edson Denis Leonel [2] and Diego Fregolent Mendes de Oliveira [1]
[1]*School of Electrical Engineering and Computer Science, University of North Dakota, Grand Forks, North Dakota 58202, USA*
[2]*Institute of Geosciences and Exact Sciences, São Paulo State University (UNESP), Rio Claro, São Paulo 13506-900, Brazil*

(Received 22 December 2025; accepted 19 May 2026; published 28 July 2026)

We study the escape of particles in the lemon billiard, a two-parameter family of billiard systems defined by the intersection of two identical circles. Using numerical simulations, we explore how the survival probability depends on the position and size of the hole, as well as on the billiard shape parameter. We find that the survival probability exhibits a two-stage decay pattern: an initial exponential regime followed by a long-time power-law tail, a signature of the stickiness effect. Our results show that the short-time exponential decay rate follows a power-law dependence on the hole size, with different scaling exponents for holes placed in chaotic regions versus mixed phase-space regions. For holes located in mixed phase-space regions, the decay exponent of the long-time power-law tail remains approximately constant, while the amplitude follows a power-law scaling with hole size. We also examine the dependence of short-time exponential decay rate on the billiard shape parameter and observe scaling behavior for small values of this parameter, which breaks down as the parameter increases.

DOI: 10.1103/md5j-ggyd

I. INTRODUCTION

Billiard systems are a type of dynamical system that originally emerged from statistical mechanics. In these systems, a particle moves freely along straight paths (or under the influence of potential forces) within a confined region on a plane [1]. When the particle hits the boundary of the billiard, it reflects elastically, changing its velocity according to the reflection law. Essentially, billiards serve as idealized models for situations where particles or waves are restricted to cavities or other uniform regions.

With advances in scientific computation, billiard systems have attracted considerable attention due to their intuitive nature and broad applicability. They provide useful frameworks for addressing complex problems across various scientific disciplines. Applications include biology [2,3], celestial mechanics [4,5], applied mathematics [6,7], plasma physics [8], waveguides [9], microwave billiards [10], dispersal of microorganisms in porous media [11], and superconductivity experiments [12].

The dynamics of billiard systems depend strongly on the billiard boundary's geometry, ranging from completely integrable (regular) to chaotic behaviors. A classic example is the circular billiard, whose dynamics are integrable because energy and angular momentum are conserved [1]. In this case, the phase space consists of periodic orbits (represented by straight lines). On the other hand, the Bunimovich stadium billiard is characterized by chaotic dynamics. Bunimovich originally studied a stadium billiard formed by two semicircles of radius R connected by two straight segments of length $2a > 0$. When $a = 0$, the system reduces to the circular billiard [13]. More recently [14,15], systems with $a < 0$ have been studied, where straight segments disappear and the boundary forms two circular sectors resembling a lens or lemon shape. This configuration leads to a mixed phase space, characterized by Kolmogorov-Arnold-Moser (KAM) islands embedded within a chaotic sea.

In this paper, we investigate the survival probability of the lemon billiard with holes of varying sizes placed at different positions on the billiard's boundary. Our focus is on understanding whether this observable exhibits scaling invariance when varying key parameters such as the hole size h and the billiard shape parameter B. We analyze the behavior of both the exponential decay at short times and the power-law tails at long times, revealing distinct dynamics depending on the hole's location in chaotic or mixed regions of phase space.

This paper is organized as follows. In Sec. II, we introduce the lemon billiard model and discuss the equations governing the system's dynamics. Section III investigates the survival probability of particles escaping through a hole at two different positions, highlighting scaling behaviors under variations of the system parameters. Finally, Sec. IV presents our conclusions.

II. LEMON BILLIARD

Introduced by Heller and Tomsovic in 1993 [16], the family of lemon billiards has since been the subject of extensive research [17–21], including more recent studies [22–24]. These systems are defined by a boundary formed from the intersection of two identical circles of radius R, with their centers separated by a distance $2B$, where $2B < 2R$. The circles are positioned symmetrically along the horizontal axis: One is shifted left by B, the other right by B, so the centers of the circles lie at $x = \pm B$, with $B \in [0, 1)$. Figure 1 illustrates this configuration: the blue and red curves represent the left- and right-shifted circles, respectively, and the cyan region highlights their intersection, which defines the billiard domain.

The boundary of the billiard is described implicitly in Cartesian coordinates by the equations

$$(x + B)^2 + y^2 = R^2, \quad x > 0,$$
$$(x - B)^2 + y^2 = R^2, \quad x < 0.$$

 ©2026 American Physical Society

[11] D. Borin, D. S. Rando, E. D. Leonel, and D. F. M. Oliveira. *Convergence dynamics and scaling laws in the dissipative relativistic kicked rotator*. European Physical Journal Special Topics (2026). DOI: https://doi.org/10.1140/epjs/s11734-026-02325-8

Eur. Phys. J. Spec. Top.
https://doi.org/10.1140/epjs/s11734-026-02325-8

THE EUROPEAN PHYSICAL JOURNAL SPECIAL TOPICS

Regular Article

Convergence dynamics and scaling laws in the dissipative relativistic kicked rotator

Daniel Borin[1,2,a], Danilo S. Rando[1,2], Edson D. Leonel[2,b], and Diego F. M. Oliveira[1,c]

[1] School of Electrical Engineering and Computer Science, University of North Dakota, Grand Forks, ND 58202, USA
[2] Institute of Geosciences and Exact Sciences, São Paulo State University (UNESP), Rio Claro, SP, Brazil

Received 23 May 2025 / Accepted 15 April 2026
© The Author(s) 2026

Abstract We investigate the convergence dynamics of this system near period-doubling bifurcations by combining analytical derivations and large-scale numerical simulations. At the bifurcation threshold ($K = K_c$), the dynamics reduce to a normal form that produces a power-law decay $d(n) \propto n^{-1/2}$, from which the critical exponents $\alpha = 1$, $\beta = -1/2$, and $z = -2$ are derived. These analytical predictions are confirmed numerically and shown to satisfy the homogeneous scaling relation $z = \alpha/\beta$. Linearization of the map near the fixed point yields an exponential relaxation law $d_n = d_0 e^{-n/\tau}$ for $K < K_c$, with $\tau \propto (K_c - K)^{-1}$, leading to the relaxation exponent $\delta = -1$. The remarkable agreement between theory and simulation demonstrates that the dissipative relativistic kicked rotator shares the same universality class as one-dimensional unimodal maps, despite its higher dimensionality and relativistic corrections.

1 Introduction

Bifurcations are fundamental to the study of nonlinear dynamical systems [1, 2], providing a mathematical framework to understand how qualitative changes in system behavior arise as control parameters are varied [3–5]. These transitions mark the boundary between distinct dynamical regimes, such as steady states, periodic oscillations, and chaotic motion, and play a central role in explaining how complex behaviors emerge from simple deterministic rules [6–8]. A single bifurcation event can drastically alter the phase-space structure of a system, creating or annihilating attractors, and changing the number or stability of equilibrium points [9, 10].

From a theoretical point of view, bifurcations represent singularities in the parameter space of dynamical equations, where infinitesimal parameter variations produce qualitative shifts in the long-term behavior of trajectories [11–14]. The classical classification of bifurcations (saddle-node, pitchfork, Hopf, and period-doubling) has been central to the development of modern nonlinear dynamics. Among these, the period-doubling bifurcation stands out as a universal route to chaos, occurring in diverse physical and biological systems and characterized by well-defined scaling properties [4, 5, 15]. Near the bifurcation threshold, the system exhibits self-similar behavior, where the evolution of trajectories can be described by scaling laws and critical exponents, concepts that parallel those found in phase transitions and critical phenomena [16–19].

The study of bifurcations extends far beyond abstract mathematics, offering explanatory power across a wide range of scientific disciplines. In physics, bifurcation analysis reveals the mechanisms underlying transitions to turbulence in fluid dynamics [20], the onset of instabilities in plasma systems [21], and resonance structures in celestial mechanics [22]. In biology, it provides information on rhythm generation in neural and cardiac systems [23], predator–prey oscillations in ecology [24], and regulatory switches that control gene expression [25]. In engineering, bifurcation theory enables the design of feedback and control systems capable of stabilizing or harnessing nonlinear dynamics [26]. These examples show the interdisciplinary nature of bifurcation theory across the natural and applied sciences.

Within this broader context, the kicked rotator model [27, 28] serves as a paradigmatic system to explore the emergence of chaos in periodically driven dynamical systems. The model, which represents a rotor subject to

[a] e-mail: d.borin@hotmail.com
[b] e-mail: edson-denis.leonel@unesp.br
[c] e-mail: diegofregolente@gmail.com (corresponding author)

Published online: 26 April 2026

[10] D. Borin, M. Rolim Sales, E. D. Leonel, and D. F. M. Oliveira. *On the Dynamics of the q-Tsallis Gauss Iterated Map*. Physica A: Statistical Mechanics and its Applications **686**, 131352 (2026). DOI: https://doi.org/10.1016/j.physa.2026.131352

Physica A 686 (2026) 131352

Contents lists available at ScienceDirect

Physica A

journal homepage: www.elsevier.com/locate/physa

On the dynamics of the q-Tsallis Gauss Iterated Map

Daniel Borin [a,b,*], Matheus Rolim Sales [c,b], Edson Denis Leonel [b], Diego Fregolent Mendes de Oliveira [a]

[a] School of Electrical Engineering and Computer Science, University of North Dakota, 58202, Grand Forks, ND, USA
[b] São Paulo State University (UNESP), Institute of Geosciences and Exact Sciences, 13506-900, Rio Claro, SP, Brazil
[c] University of Essex, School of Mathematics, Statistics and Actuarial Science, Wivenhoe Park, Colchester, CO4 3SQ, United Kingdom

ARTICLE INFO

Dataset link: https://doi.org/10.5281/zenodo.17593788

ABSTRACT

We investigate the dynamical properties of a q-deformed generalization of the Gaussian iterated map, referred to as the q-Tsallis Gaussian Iterated Map, obtained by replacing the standard exponential with the Tsallis q-exponential function. Through bifurcation diagrams, Lyapunov exponent analysis, and isoperiodic diagrams, we characterize the transitions between periodic and chaotic regimes, as well as the emergence of multistability and bubbling phenomena, reveals that the introduction of the nonextensive parameter induces significant changes in the system's dynamics.

1. Introduction

Boltzmann–Gibbs (BG) statistical mechanics is one of the most fundamental frameworks in theoretical physics. Originally developed to provide an analytical description of thermodynamical quantities at thermal equilibrium, it has since been applied to a wide range of other physical systems [1–3]. The core of this theory is the Boltzmann–Gibbs entropy [4,5], defined as

$$S_{BG} = -k \sum_{i=1}^{W} p_i \ln p_i, \tag{1}$$

where k is a positive constant (typically chosen as $k = k_B$, the Boltzmann constant, or simply $k = 1$ in information theory), W is the total number of accessible micro-states, and $\{p_i\}$ are the probabilities associated with each state, satisfying $\sum_{i=1}^{W} p_i = 1$.

Despite its success, BG statistical mechanics does not adequately capture the behavior of many complex systems. These include, for example, turbulent flows [6–8], quantum entanglement [9,10], trapped ion subjected to radiofrequency heating [11], cosmic rays [12,13], high-energy particle collisions [14–18], financial markets [19–22], biological motion [23–26], and systems exhibiting classical [27–33] or quantum [34,35] chaos. In such systems, standard BG entropy often does not provide an accurate or complete description, leading to the development of more general approaches.

In response to this limitation, nonextensive statistical mechanics was proposed by Constantino Tsallis [36–41] as a generalization of BG statistical mechanics. Inspired by multifractal systems [42–44], Tsallis introduced a generalized entropy formula, known as the Tsallis entropy:

$$S_q = k \frac{1 - \sum_{i=1}^{W} p_i^q}{q - 1}, \tag{2}$$

* Corresponding author at: School of Electrical Engineering and Computer Science, University of North Dakota, 58202, Grand Forks, ND, USA.
E-mail address: d.borin@hotmail.com (D. Borin).
URL: https://danielborin.github.io/ (D. Borin).

https://doi.org/10.1016/j.physa.2026.131352
Received 3 December 2025; Received in revised form 22 January 2026
Available online 4 February 2026
0378-4371/© 2026 The Authors. Published by Elsevier B.V. This is an open access article under the CC BY license (http://creativecommons.org/licenses/by/4.0/).

[9] M. Rolim Sales, L. C. de Souza, D. Borin, M. Mugnaine, J. D. Szezech Jr., R. L. Viana, I. L. Caldas, E. D. Leonel, and C. G. Antonopoulos. *pynamicalsys: A Python toolkit for the analysis of dynamical systems*. Chaos, Solitons & Fractals **201**, 117269 (2025). DOI: `https://doi.org/10.1016/j.chaos.2025.117269`

Chaos, Solitons and Fractals 201 (2025) 117269

Contents lists available at ScienceDirect

Chaos, Solitons and Fractals

journal homepage: www.elsevier.com/locate/chaos

pynamicalsys: A Python toolkit for the analysis of dynamical systems

Matheus Rolim Sales [a,b], Leonardo Costa de Souza [c,d], Daniel Borin [b,e], Michele Mugnaine [c,f], José Danilo Szezech [c,g,h], Ricardo Luiz Viana [i], Iberê Luiz Caldas [c], Edson Denis Leonel [b], Chris G. Antonopoulos [a,*]

[a] *University of Essex, School of Mathematics, Statistics and Actuarial Science, Wivenhoe Park, Colchester, CO4 3SQ, United Kingdom*
[b] *São Paulo State University (UNESP), Institute of Geosciences and Exact Sciences, 13506-900, Rio Claro, SP, Brazil*
[c] *Institute of Physics, University of São Paulo, 05315-970, São Paulo, SP, Brazil*
[d] *Department of Physics, Institute for Complex Systems and Mathematical Biology, SUPA, University of Aberdeen, AB24 3UX, Aberdeen, United Kingdom*
[e] *University of North Dakota, School of Electrical Engineering and Computer Science, 58202, Grand Forks, ND, United States of America*
[f] *Lorena School of Engineering (EEL-USP), University of São Paulo, 12602-810, Lorena, SP, Brazil*
[g] *Graduate Program in Science, State University of Ponta Grossa, 84030-900, Ponta Grossa, PR, Brazil*
[h] *Department of Mathematics and Statistics, State University of Ponta Grossa, 84030-900, Ponta Grossa, PR, Brazil*
[i] *Federal University of Paraná, Department of Physics, Interdisciplinary Center for Science, Technology and Innovation, Center for Modeling and Scientific Computing, 81531-980, Curitiba, PR, Brazil*

ARTICLE INFO

Keywords:
Nonlinear dynamical systems
Chaos theory
Python package

ABSTRACT

Since Lorenz's seminal work on a simplified weather model, the numerical analysis of nonlinear dynamical systems has become one of the main subjects of research in physics. Despite of that, there remains a need for accessible, efficient, and easy-to-use computational tools to study such systems. In this paper, we introduce `pynamicalsys`, a simple yet powerful open-source Python module for the analysis of nonlinear dynamical systems. In particular, `pynamicalsys` implements tools for trajectory simulation, bifurcation diagrams, Lyapunov exponents and several others chaotic indicators, period orbit detection and their manifolds, as well as escape and basins analysis. We demonstrate the capabilities of `pynamicalsys` through a series of examples that reproduces well-known results in the literature while developing the mathematical analysis at the same time. We also provide the Jupyter notebook containing all the code used in this paper, including performance benchmarks. `pynamicalsys` is freely available via the Python Package Index (PyPI) and is intended to support both research and teaching in nonlinear dynamics.

1. Introduction

The success of Newton's theory on mechanics led to the idea of a deterministic, and fully predictable Universe. Laplace once famously stated that if an intellect at a certain moment in time would know all the forces that set nature in motion, and all the positions of all objects, then this intellect would be able to predict the past and the future of the entire Universe [1]. This idea was later challenged by Poincaré in his seminal work on the stability of the solar system [2]. Poincaré, to simplify the problem,

* Corresponding author.
E-mail addresses: rolim.sales.m@gmail.com (M.R. Sales), canton@essex.ac.uk (C.G. Antonopoulos).

https://doi.org/10.1016/j.chaos.2025.117269
Received 7 July 2025; Received in revised form 16 September 2025; Accepted 17 September 2025
0960-0779/© 2025 The Author(s). Published by Elsevier Ltd. This is an open access article under the CC BY license (http://creativecommons.org/licenses/by/4.0/).

[8] D. Borin, J. D. Szezech Jr. and M. Rolim Sales. *Characterizing and quantifying weak chaos in fractional dynamics*. Chaos, Solitons & Fractals **200**, 117137, (2025). DOI: `https://doi.org/10.1016/j.chaos.2025.117137`

Chaos, Solitons and Fractals 200 (2025) 117137

Contents lists available at ScienceDirect

Chaos, Solitons and Fractals

journal homepage: www.elsevier.com/locate/chaos

Characterizing and quantifying weak chaos in fractional dynamics

Daniel Borin [a,b,*], José Danilo Szezech Jr. [c,d,e], Matheus Rolim Sales [b,f]

[a] University of North Dakota, School of Electrical Engineering and Computer Science, 58202, Grand Forks, ND, USA
[b] São Paulo State University (UNESP), Institute of Geosciences and Exact Sciences, 13506-900, Rio Claro, SP, Brazil
[c] Graduate Program in Science, State University of Ponta Grossa, 84030-900, Ponta Grossa, PR, Brazil
[d] Department of Mathematics and Statistics, State University of Ponta Grossa, 84030-900, Ponta Grossa, PR, Brazil
[e] Institute of Physics, University of São Paulo, 05508-900, São Paulo, SP, Brazil
[f] University of Essex, School of Mathematics, Statistics and Actuarial Science, Wivenhoe Park, Colchester, CO4 3SQ, UK

ARTICLE INFO

Keywords:
Fractional maps
Cascade of bifurcations type trajectories
Weak chaos
Hurst exponent
Recurrence time entropy

ABSTRACT

A particularly intriguing and unique feature of fractional dynamical systems is the cascade of bifurcations type trajectories (CBTT). We examine the CBTTs in a generalized version of the standard map that incorporates the Riemann–Liouville fractional derivative, known as the Riemann–Liouville Fractional Standard Map (RLFSM). We propose a methodology that uses two quantifiers based solely on the system's time series: the Hurst exponent and the recurrence time entropy, for characterizing such dynamics. This approach allows us to effectively characterize the dynamics of the RLFSM, including regions of CBTT and chaotic behavior. Our analysis demonstrates that regions of CBTT are associated with trajectories that exhibit lower values of these quantifiers compared to strong chaotic regions, indicating weakly chaotic dynamics during the CBTTs.

1. Introduction

Fractional dynamical systems (FDS) are systems governed by fractional differential/difference equations (FDE), incorporating fractional time derivatives/differences [1–3]. FDEs are integro-differential/difference equations, and solving them requires extensive computational resources [4]. This complexity makes the investigation of their general properties particularly challenging. In this sense, the research on nonlinear fractional dynamical systems has advanced notably, with several studies [5–17]. Many of these investigations are based on fractional maps that describe periodically kicked systems. [18–24].

A special property of these systems is that FDS exhibit memory effects, leading to potentially unconventional properties in FDE solutions [25–27]: trajectories may intersect, attractors can overlap, and attractors exist only in an asymptotic sense, with their limiting values not necessarily belonging to their basins of attraction.

In this sense, a novel type of regime unique to FDS emerges in fractional systems, called cascade of bifurcations type trajectories (CBTT) [27]. In CBTT, a sequence of bifurcations occurs not due to variations in the system parameters, as in traditional dynamical systems, but rather along a single attracting trajectory during its temporal evolution. These bifurcations occur within specific time windows during which the trajectory is confined to smaller subsets of the phase space, as if temporarily trapped. The orbit enters from the chaotic region into a CBBT, remains there for some time, and then returns to the chaotic region, repeating this process multiple times. This behavior is similar to that of sticky orbits in two-dimensional, area-preserving maps. The stickiness effect [28–35], also known as weak chaos, is one of the main features of two-dimensional, area-preserving maps. It occurs when chaotic orbits exhibit

* Corresponding author at: São Paulo State University (UNESP), Institute of Geosciences and Exact Sciences, 13506-900, Rio Claro, SP, Brazil.
E-mail address: d.borin@hotmail.com (D. Borin).

https://doi.org/10.1016/j.chaos.2025.117137
Received 7 July 2025; Received in revised form 19 August 2025; Accepted 24 August 2025
0960-0779/© 2025 Published by Elsevier Ltd.

[7] D. Borin *Hurst exponent: A method for characterizing dynamical traps*, Physical Review E **110**, 064227 (2024). DOI: https://doi.org/10.1103/PhysRevE.110.064227

Hurst exponent: A method for characterizing dynamical traps

Daniel Borin*

São Paulo State University (UNESP), IGCE - Physics Department, 13506-900, Rio Claro, Sao Paulo, Brazil

(Received 3 July 2024; accepted 24 October 2024; published 31 December 2024)

Dynamical trapping occurs when the duration of time spent in specific regions of phase space increases, often associated with stickiness around invariant islands during manifold crossings. This paper introduces the Hurst exponent as a tool to characterize the dynamics of a typical quasiintegrable Hamiltonian system with coexisting regular and chaotic regions. Beyond detecting chaotic orbits and sticky regions, applying a finite-time analysis reveals a multimodal distribution of the finite-time Hurst exponent, where each mode corresponds to motion around islands of different hierarchical levels. The advantage of the Hurst exponent method over other standard techniques lies in its ability to quickly indicate chaotic dynamical structures. It effectively distinguishes between quasiperiodic and chaotic orbits temporarily trapped in sticky domains using very short trajectories. Additionally, since it operates based on time series data, it facilitates the exploration of trapping effects in dynamic systems that lack well-defined laws, a common scenario in natural dynamics.

DOI: 10.1103/PhysRevE.110.064227

I. INTRODUCTION

Hamiltonian systems represent a category of dynamical systems that elucidate the dynamic behavior of particles in motion, relying on the principle of energy conservation. Within this group, a distinction arises between integrable and nonintegrable Hamiltonian systems. In integrable Hamiltonian systems, the motion of particles follows regular and discernible patterns. Conversely, nonintegrable Hamiltonian systems present a more intricate and unpredictable nature, where the phase space exhibits a complex combination of regularity and chaos, featuring Kolmogorov-Arnold-Moser (KAM) islands, invariant tori, spanning curves, and chaotic seas [1]. Due to the existence of islands scattered throughout the chaotic sea, the sea forms a fat fractal [2], making it hard to say exactly where one island ends and another begins. Larger islands are surrounded by smaller ones, and those smaller ones are in turn surrounded by even smaller islands. This pattern repeats at smaller and smaller scales, creating an endless hierarchy of islands within islands. [3] These characteristics introduce features such as dynamical traps, which affect the diffusion process [4], leading to intriguing properties in the dynamics.

In a general sense, the dynamical trap is a domain in phase space where a particle (or its trajectory) can spend arbitrarily long finite time, performing almost regular dynamics, called a flight, even though the entire trajectory is random in any appropriate sense [5]. In a chaos scenario, there are the dynamical traps named stickiness [6–12], which emerge when orbits, initially influenced by chaotic dynamics, exhibit a prolonged interaction with specific regions characterized by regular behavior, such that these trajectories become temporarily "stuck" or trapped to particular structures within the phase space for a time that may be, eventually, long. This phenomenon affects global properties of the system, such as the decay of correlations [8,13,14] and transport [9]. Before escaping, the orbits are confined within a region bounded by cantori [15], a Cantor set formed from the remnants of the destroyed KAM tori. This structure serves as a partial barrier to the transport in phase space and can be trapped in the region cantori enclosed. Once inside a cantorus, chaotic orbits can cross into an inner cantorus. This process can continue to infinitely small scales within the hierarchical structure of islands around islands [16].

A way to quantify these trap effects is the finite-time Lyapunov exponent (FTLE) [17,18] that measures the exponential rates of principal divergences of the initially neighboring trajectories during finite-time intervals. However, computing requires a well-defined law that describes the orbit, which is unavailable in some natural dynamics. Moreover, these exponents might not be the most effective method for detecting stickiness. Once an orbit is trapped, the largest Lyapunov exponent decreases, slowing down its convergence—it takes longer to reach its asymptotic (infinite-time) value.

Recently, a new method has been proposed to detect chaotic orbits by calculating the Shannon entropy of the recurrence time [19–21]. It has proven to be a better option for distinguishing between regular and chaotic orbits than the Lyapunov exponents. However, it has only applied in situations where the Slater theorem [22,23] is valid.

This paper presents a measure to identify regular, chaotic, and sticky regions: the Hurst exponent, which is essentially a measure of the long-term memory of time series. Using the Hurst exponent, it is possible to distinctly identify both the regular regions and the transitions to chaotic motion as a system parameter varies. Additionally, computing the finite-time Hurst exponent (FTH) distribution reveals a multimodal pattern, where each peak corresponds to a distinct hierarchical level within the islands-around-islands structure.

*Contact author: d.borin@hotmail.com

 ©2024 American Physical Society

[6] A. L. P. Livorati, A. P. Faber, and D. Borin *Asymptotic convergence for the dynamics of a Duffing-like oscillator under scaling analyses*, Chaos **35**, 013108 (2025). DOI: https://doi.org/10.1063/5.0233700

Chaos ARTICLE pubs.aip.org/aip/cha

Asymptotic convergence for the dynamics of a Duffing-like oscillator under scaling analyses

Cite as: Chaos **35**, 01 31 08 (2025); doi: 1 0.1 063/5.0233700
Submitted: 1 6 August 2024 · Accepted: 6 December 2024 ·
Published Online: 3 January 2025

View Online Export Citation CrossMark

André Luís Prando Livorati,[a] André Paganotti Faber, and Daniel Borin

AFFILIATIONS

IGCE—Physics Department, São Paulo State University (UNESP), 13506-900 Rio Claro, SP, Brazil

Note: This paper is part of the Focus Issue, From Sand to Shrimps: In Honor of Professor Jason A. C. Gallas.
[a] **Author to whom correspondence should be addressed:** andre.livorati@unesp.br

ABSTRACT

The dynamics of the convergence for the stationary state considering a Duffing-like equation are investigated. The driven potential for these dynamics is supplied by a damped forced oscillator that has a piecewise linear function. Fixed points and their basins of attraction were identified and measured. We used entropy basin techniques to characterize the basins of attraction, where a changeover in its boundary basin entropy is observed concerning the boundary length. Additionally, we have a set of polar coordinates to describe the asymptotic convergence of the dynamics based on the range of the control parameter and initial conditions. The entire convergence to the stationary state was characterized by scaling laws.

Published under an exclusive license by AIP Publishing. https://doi.org/10.1063/5.0233700

23 June 2025 13:28:30

A Duffing-like equation is studied considering a driven potential given by a piecewise linear function. The modeling has applications in several areas, such as electronic circuits, synchronization, mechanical systems, and biology, among others. For a specific range of the control parameter, we set two attracting fixed points and characterized their basins of attraction. Through the analysis of the entropy basin, we observed a transition in the boundary basin entropy for a given critical control parameter. The results indicate a transition in the length of the basin boundary. To investigate the asymptotic convergence of the dynamics to the fixed points more precisely, we applied a linear to polar coordinates transformation, which presented itself as a useful metric for the description of the convergence to the stationary states, and by varying ranging the control parameter and initial conditions, an exponential decay to the fixed points was observed. We have proposed some scaling law arguments to describe this behavior, and the numerical results we obtained are in good agreement, since a single and universal plot was drawn. These results confirm the robustness of the formalism, which may be extended to other similar dynamical systems.

I. INTRODUCTION

Nonlinear differential equations are often used to describe the behavior of dynamical systems. Depending on the nonlinear terms involved in the equations, a rich variety of nonlinear phenomena can be observed, considering both conservative and dissipative dynamics.[1,2] A variation in the control parameters of the system may lead the dynamics to exhibit phase transitions, which, in the context of statistical mechanics, can be linked to abrupt changes in spatial structure.[3,4] In contrast, alterations in the phase space structure are specifically associated with phase transitions in dynamical systems.[5–7]

A useful technique to describe such phase transitions is scaling analysis, where near the criticality, the dynamics can be characterized via critical exponents,[8–14] especially if there is an asymptotic behavior of some physical observable.[15–20] In addition, scaling laws can contribute to the development of more precise and robust mathematical models for the description of complex phenomena.[21] The importance of scaling laws extends to several areas, including the physics of critical phenomena;[22] materials science;[23] macro, micro, and nanoscales;[24] multifractal objects;[25] astronomy;[26] fractional dynamics;[27] plasma physics;[28,29] biology;[30,31] and engineering;[32,33] among many other applications.[34]

One of the most widely researched nonlinear dynamical systems is the Duffing oscillator.[35] The nonlinear terms in the differential equation of this system make it possible to analyze several complex phenomena such as bifurcations,[36–38] resonance,[39–41] and chaotic transitions.[42–44] In addition, the nonlinear dynamics of the Duffing equation has direct applications in several areas, including biology,[45,46] laser dynamics,[47] materials engineering,[48–51] and electrical circuits,[52–55] among others.

Published under an exclusive license by AIP Publishing

[5] M. Rolim Sales, D. Borin, D. R. da Costa, J. D. Szezech Jr., and E. D. Leonel *An investigation of escape and scaling properties of a billiard system*, Chaos **34**, 113122 (2024). DOI: https://doi.org/10.1063/5.0222215

Chaos ARTICLE pubs.aip.org/aip/cha

An investigation of escape and scaling properties of a billiard system

Cite as: Chaos **34**, 113122 (2024); doi: 10.1063/5.0222215
Submitted: 6 June 2024 · Accepted: 24 October 2024 ·
Published Online: 8 November 2024

Matheus Rolim Sales,[1,a)] Daniel Borin,[1] Diogo Ricardo da Costa,[1] José Danilo Szezech, Jr.,[2,3] and Edson Denis Leonel[1]

AFFILIATIONS

[1] Departamento de Física, Universidade Estadual Paulista (UNESP), 13506-900 Rio Claro, SP, Brazil
[2] Programa de Pós-Graduaç ao em Ciências, Universidade Estadual de Ponta Grossa, 84030-900 Ponta Grossa, PR, Brazil
[3] Departamento de Matemática e Estatística, Universidade Estadual de Ponta Grossa, 84030-900 Ponta Grossa, PR, Brazil

Note: This paper is part of the Focus Issue on Anomalous Diffusion and Fluctuations in Complex Systems and Networks.
[a)] **Author to whom correspondence should be addressed:** matheusrolim95@gmail.com

ABSTRACT

We investigate some statistical properties of escaping particles in a billiard system whose boundary is described by two control parameters with a hole on its boundary. Initially, we analyze the survival probability for different hole positions and sizes. We notice that the survival probability follows an exponential decay with a characteristic power-law tail when the hole is positioned partially or entirely over large stability islands in phase space. We find that the survival probability exhibits scaling invariance with respect to the hole size. In contrast, the survival probability for holes placed in predominantly chaotic regions deviates from the exponential decay. We introduce two holes simultaneously and investigate the complexity of the escape basins for different hole sizes and control parameters by means of the basin entropy and the basin boundary entropy. We find a non-trivial relation between these entropies and the system's parameters and show that the basin entropy exhibits scaling invariance for a specific control parameter interval.

Published under an exclusive license by AIP Publishing. https://doi.org/10.1063/5.0222215

08 November 2024 16:31:27

The phase space of a typical two-dimensional Hamiltonian system is not completely ergodic. There is a coexistence of chaotic and regular regions that gives rise to the well-known phenomenon of stickiness. Chaotic orbits become trapped near stability islands for long, but finite, times, and this intermittence in the chaotic motion shapes the transport and statistical properties across phase space. In this paper, we analyze the escape dynamics of a billiard system whose boundary is defined by two control parameters with an exit hole along its boundary. We find that the survival probability either follows an exponential or a stretched exponential decay depending on the position of the hole. By introducing two holes simultaneously, we construct the escape basins for different hole's sizes and quantify the basins complexity using the basin entropy and the basin boundary entropy. The complexity of the basins depends nontrivially on the control parameters, and we find that the basin entropy exhibits scaling invariance for a specific control parameter interval.

I. INTRODUCTION

In general, the phase space of a typical quasi-integrable Hamiltonian system is mixed, where regular and chaotic domains coexist.[1] The regular regions consist of periodic and quasiperiodic orbits that lie on invariant tori, while the chaotic orbits fill densely the whole available region in phase space. For two-dimensional area-preserving maps, the invariant tori divides the phase space into distinct and unconnected domains; i.e., an orbit initially inside an island will never reach the chaotic sea and vice versa.[1,2] The stability islands and chaotic regions organize themselves in phase space in an infinite hierarchical islands-around-islands structure, where the larger islands are surrounded by smaller islands, which are in turn surrounded by even smaller islands and so on for increasingly smaller scales.[3,4] This complex interplay between stability islands and chaotic regions gives rise to the phenomenon of stickiness.[5–12] The stickiness of chaotic orbits occurs near stability

Published under an exclusive license by AIP Publishing

[4] D. Borin, V. L. G. de Brito, E. D. Leonel, and M. Hansen *Buzz pollinaation: A theorical analysis via scaling invariance*, Physical Review E **110**, 054201 (2024). DOI: `https://doi.org/10.1103/PhysRevE.110.054201`

Buzz pollination: A theoretical analysis via scaling invariance

Daniel Borin,[1] Vinicius Lourenço Garcia de Brito,[2] Edson Denis Leonel,[1] and Matheus Hansen[3]
[1]*São Paulo State University (UNESP), IGCE - Physics Department, 13506-900, Rio Claro, SP, Brazil*
[2]*Instituto de Biologia, Universidade Federal de Uberlândia, Uberlândia, 38405-315, MG, Brazil*
[3]*Center for Mathematics and Applications (NOVA Math), NOVA School of Science and Technology (NOVA FCT), Universidade NOVA de Lisboa, Quinta da Torre, 2829-516, Caparica, Portugal*

(Received 31 January 2024; accepted 30 August 2024; published 1 November 2024)

Nearly half of the bee species can perform a fascinating stereotyped behavior to collect pollen grains by vibrating flowers, known as buzz pollination. During the floral visit, these bees mechanically transfer the vibrations produced by their thoracic indirect flight muscles to the flower anther, inducing the movement of the pollen grains and leading them to be released through a small pore or slit placed at the tip of the anther in poricidal flowers. In such flowers, pollen release is affected by the vibrational behavior of buzzing bees, primarily their duration and velocity amplitude. However, we know little about how poricidal anther morphology may influence it. In this work, we investigated through a theoretical and numerical point of view the buzz pollination process considering a typical poricidal anther of a tomato flower (*Solanum lycopersicum*), which in our work will be approached by a rectangular billiard, experiencing vibrations applied by a bumblebee (*Bombus terrestris*). Our primary goals in this paper are (i) to understand the mechanism behind the pollen release in this model, (ii) to observe some scale effects associated with morphological variations of the anther (as pore size and anther shape), and (iii) analyze how these results are related to natural buzz pollination systems.

DOI: 10.1103/PhysRevE.110.054201

I. INTRODUCTION

Animal vectors pollinate most flowering plants, making bees the most frequent pollinator group [1–3], it being estimated that bees are responsible for nearly 80% of all insect-mediated pollination in nature [4–6]. During their floral visits, bees can perform several behaviors to collect different floral resources such as nectar, oils, and pollen grains. A fascinating case of such bee behavior on flowers is floral buzzing [7,8]. Medium to large-sized female bees of many species can vibrate their thoracic muscles on flowers to collect pollen grains [9]. Such high-pitched vibrations are mechanically transferred to anthers, releasing pollen, which is eventually deposited onto stigmas in a process called buzz pollination [8,10,11]. Buzz pollination may occur in more than 20 000 flowering species, distributed in 65 nonrelated families, most of them bearing tubular anthers that open by a small apical pore or slit and provide pollen as the only or leading floral resource, the so-called "pollen flowers" [10,12]. Although buzz pollination is a well-documented phenomenon, the mechanical interaction of poricidal anthers with bee mechanical vibrations and its effect on pollen release is still poorly understood.

The vibrations of thoracic muscles are part of several bee behaviors, including flight, thermogenesis, communication, and buzz pollination. In general, while visiting flowers, bees may produce continuous vibrations of up to two seconds or several multiple short pulses of vibrations of tens to hundreds of milliseconds [8,13]. Such mechanical floral vibrations have a high fundamental peak frequency (i.e., number of cycles per second), generally from 100 Hz to 400 Hz. Finally, the bee's vibrations may also be described by the amplitude (i.e., the magnitude of change of sinusoidal motion) of their body displacement, velocity, or acceleration. Despite amplitude being hard to measure during floral buzzing empirically, it is believed to be, together with vibration duration, the most crucial bee vibrational component related to pollen released by poricidal anthers. When all the other vibrational parts are kept constant, peak velocity amplitude is the most promising observable affecting pollen release by poricidal anthers in numerical approaches [14]. Besides the biomechanical abilities of bees during floral buzzing, the anther morphology should also play a key role in pollen release during buzz pollination [15].

There is a vast morphological diversity of poricidal anthers in buzz-pollinated pollen flowers. Poricidal anthers may vary in shape, size, and pore size among species and even within species in the same flower (i.e., heteranthery). These anther morphological traits may affect pollen release during floral buzzing. More prominent anthers release more pollen grains per time unit than small ones during flower lifespan [15]. However, given the reduced spatial scale of such a phenomenon, it is hard to access the physical features of individual pollen grains, as the escape probability from the anther, which can hamper our understanding of other potential effects of anther morphology in pollen release. In this sense, mathematical models describe it better and create theoretical hypotheses that could be empirically tested.

In this study, we are particularly interested in investigating the buzz pollination process considering a billiard approach [16–18]. Our method considers the anther of the flower shaped as a billiard system, which has a boundary that will oscillate according to specific vibrations produced by a bee to simulate a typical buzz pollination process [14]. In this way, we simulate the contact between a tomato flower (*Solanum*

 ©2024 American Physical Society

[3] M. Rolim Sales, D. Borin, L. C. de Souza, J. D. Szezech Jr., R. L. Viana, I. L. Caldas, and E. D. Leonel *Ratchet current and scaling properties in a nontwist mapping*, Chaos, Solitons & Fractals **189**, 115614 (2024). DOI: https://doi.org/10.1016/j.chaos.2024.115614

Chaos, Solitons and Fractals 189 (2024) 115614

Contents lists available at ScienceDirect

Chaos, Solitons and Fractals

journal homepage: www.elsevier.com/locate/chaos

Ratchet current and scaling properties in a nontwist mapping

Matheus Rolim Sales [a,*], Daniel Borin [a], Leonardo Costa de Souza [b], José Danilo Szezech Jr. [c,d], Ricardo Luiz Viana [e], Iberê Luiz Caldas [b], Edson Denis Leonel [a]

[a] Departamento de Física, Universidade Estadual Paulista (UNESP), 13506-900, Rio Claro, SP, Brazil
[b] Instituto de Física, Universidade de São Paulo, 05315-970, São Paulo, SP, Brazil
[c] Programa de Pós-Graduação em Ciências, Universidade Estadual de Ponta Grossa, 84030-900, Ponta Grossa, PR, Brazil
[d] Departamento de Matemática e Estatística, Universidade Estadual de Ponta Grossa, 84030-900, Ponta Grossa, PR, Brazil
[e] Departamento de Física, Universidade Federal do Paraná, 81531-990, Curitiba, PR, Brazil

ARTICLE INFO

Keywords:
Ratchet effect
Unbalanced stickiness
Scaling invariance
Critical exponents

ABSTRACT

We investigate the transport of particles in the chaotic component of phase space for a two-dimensional, area-preserving nontwist map. The survival probability for particles within the chaotic sea is described by an exponential decay for regions in phase space predominantly chaotic and it is scaling invariant in this case. Alternatively, when considering mixed chaotic and regular regions, there is a deviation from the exponential decay, characterized by a power law tail for long times, a signature of the stickiness effect. Furthermore, due to the asymmetry of the chaotic component of phase space with respect to the line $I = 0$, there is an unbalanced stickiness that generates a ratchet current in phase space. Finally, we perform a phenomenological description of the diffusion of chaotic particles by identifying three scaling hypotheses, and obtaining the critical exponents via extensive numerical simulations.

1. Introduction

The phase space of a two-dimensional integrable Hamiltonian system is composed of periodic and quasiperiodic invariant tori. When a weak perturbation is introduced into such a system, according to the Kolmogorov-Arnold-Moser (KAM) theorem [1], the sufficiently irrational tori survive the perturbation (KAM tori), while the rational ones are destroyed. Near the original position of the destroyed rational tori, emerges a set of elliptical and hyperbolic fixed points, as outlined by the Poincaré-Birkhoff theorem [1]. The chaotic motion appears in the vicinity of the hyperbolic fixed points due to their unstable nature, while the elliptical points are the centers of the regular regions, hereafter named stability islands. The coexistence of chaotic and regular regions in two-dimensional quasi-integrable Hamiltonian system makes its phase space neither integrable nor uniformly hyperbolic. The phase space is divided into distinct and unconnected domains, where the chaotic orbits fill densely the available region in phase space and the stability islands consist of periodic and quasiperiodic orbits that lie on invariant tori. Furthermore, an orbit initially in the chaotic sea will never enter any island, and the periodic and quasi-periodic orbits will never reach the chaotic sea [1,2].

For increasing perturbation strength, the KAM tori are also destroyed and their remnants form a Cantor set known as cantori [2–4]. The role of the KAM tori and the cantori in the transport of particles in phase space differs fundamentally. While the KAM tori are full barriers to the transport in phase space, the cantori act as partial barriers, allowing particles to pass through them. When a particle crosses a cantorus, it might stay trapped in the region bounded by the cantorus for a long, but finite, period of time, during which it behaves similarly as a quasiperiodic orbit, until it escapes to the chaotic sea. This intermittence in the dynamics of a chaotic orbit is the phenomenon of stickiness [4–12]. The structure of stability islands embedded in the chaotic sea and cantori organize itself in a hierarchical structure of islands-around-islands, where the larger islands are surrounded by smaller islands, which are in turn surrounded by even smaller islands and so on for increasingly smaller scales [13,14]. In this way, during the time a chaotic orbit is trapped in a region bounded by a cantorus, it might cross inner cantori for arbitrarily small scales and thus stay trapped for longer times. This long times affects the statistical properties of the transport of particles in phase space [15–18], as well as the recurrence time statistics [19–24], the survival probability [10,25–35], and the decay of correlations [6–8,36,37].

About two decades ago, a new feature was observed in the transport of particles in the chaotic component of phase space in Hamiltonian systems: the existence of a preferential direction for the transport without an external bias, the so-called Hamiltonian ratchet [38–44]. The ratchet

* Corresponding author.
E-mail address: rolim.sales@unesp.br (M. Rolim Sales).

https://doi.org/10.1016/j.chaos.2024.115614
Received 17 June 2024; Received in revised form 11 September 2024; Accepted 1 October 2024
Available online 10 October 2024
0960-0779/© 2024 Elsevier Ltd. All rights are reserved, including those for text and data mining, AI training, and similar technologies.

[2] D. Borin *Caputo fractional standard map: Scaling invariance analyses*, Chaos, Solitons & Fractals **181**, 114597 (2024). DOI: https://doi.org/10.1016/j.chaos.2024.114597

Chaos, Solitons and Fractals 181 (2024) 114597

Contents lists available at ScienceDirect

Chaos, Solitons and Fractals

journal homepage: www.elsevier.com/locate/chaos

Caputo fractional standard map: Scaling invariance analyses

Daniel Borin

Departamento de Física, Univ. Estadual Paulista - Unesp, Av.24A, 1515, Bela Vista, Rio Claro, CEP: 13506-900, SP, Brazil

ARTICLE INFO

Keywords:
Fractional standard map
Fractional discrete map
Caputo derivative
Escape of particles
Scattering properties
Survival probability
Scaling invariance
Nonlinear dynamics

ABSTRACT

In this paper, we investigate the scaling invariance of survival probability in the Caputo fractional standard map of the order $1 < \alpha < 2$ considered on a cylinder. We consider relatively large values of the nonlinearity parameter K for which the map is chaotic. The survival probability has a short plateau followed by an exponential decay and is scaling invariant for all considered values of α and K.

1. Introduction

Differential equations are a fundamental tool for studying dynamical systems, enabling the investigation of the evolution of observables over time and capturing the long-term behavior of these systems. These equations elucidate the rates of change in system variables and typically involve integer-order derivatives. A generalization of this theory has led to the rise of the field of fractional differential equations (FDEs) [1], extending the conventional framework of differential equations by incorporating fractional derivatives. This extension has countless applications in various scientific fields, such as quantum mechanics [2–7], electrodynamics [8–11], economics [12–15], engineering [16–18], biology [19,20], and geology [21].

Fractional derivatives come in various types, each with its unique characteristics and applications. The most common among them include Riemann–Liouville, Caputo, Grünwald–Letnikov, Hadamard type, etc. [1]. As initial conditions are crucial in physical dynamics, adopting the Caputo derivative in mechanical systems is convenient. This choice is particularly useful since the initial conditions for specific fractional dynamical systems align with those for usual dynamical systems, allowing for a clearer physical interpretation of the system.

Sometimes, differential equations can be complicated. A way to simplify the problem is to reduce it to the study of simple discrete maps. This approach provides a simplified yet valuable perspective on the dynamics of the system, enhancing its suitability for simulations and computational studies. Maps, derived from equations of motion involving fractional derivatives, exhibit a noteworthy characteristic: long-term memory effects [22,23]. In this context, the present state of the system is uniquely determined by all past states, adding an intriguing layer of complexity and historical dependence to the analysis.

Memory is a significant property of human beings and is the subject of extensive biophysical and psychological research. The possibility of investigating the dynamics of memory in neurons and proteins [24] becomes attractive for the study of fractional maps.

An essential and insightful measure when exploring the statistical characteristics of transport phenomena is the concept of survival probability. This probability quantifies the likelihood of a diffusing particle remaining within a specific region at a given point in time. In the context of fully chaotic systems, the behavior of survival probability exhibits a distinct pattern over time, characterized by exponential decay [25]. These properties have not been explored for Caputo fractional maps.

Motivated by the above descriptions, this paper aims to explore the dynamic characteristics of a Caputo Fractional Map obtained by replacing the integer derivative with the Caputo derivative in the equation of motion that originates the famous standard map (Chirikov–Taylor Map). More specifically, we vary control parameters and observe how they affect the survival probability, seeking invariance of scaling.

The layout of the study is as follows: The Caputo Fractional Standard Map is introduced in Section 2. In Section 3, a study of survival probability is presented, varying all control parameters and demonstrating that this observable is scaling invariant concerning the same parameters. Finally, a discussion is provided in Section 4.

E-mail address: d.borin@hotmail.com.

https://doi.org/10.1016/j.chaos.2024.114597
Received 23 November 2023; Received in revised form 6 February 2024; Accepted 9 February 2024
0960-0779/© 2024 Elsevier Ltd. All rights reserved.

[1] D. Borin, A. L. P. Livoratti and E. D. Leonel *An investigation of the survival probability for chaotic diffusion in a family of discrete Hamiltonian mappings*, Chaos, Solitons & Fractals **175**, 113965 (2023). DOI: https://doi.org/10.1016/j.chaos.2023.113965

Chaos, Solitons and Fractals 175 (2023) 113965

Contents lists available at ScienceDirect

Chaos, Solitons and Fractals

journal homepage: www.elsevier.com/locate/chaos

An investigation of the survival probability for chaotic diffusion in a family of discrete Hamiltonian mappings

Daniel Borin [a,b,1,*], André Luís Prando Livorati [a,c,1], Edson Denis Leonel [a,1]

[a] Departamento de Física, Univ. Estadual Paulista - Unesp, Av.24A, 1515, Bela Vista, Rio Claro, CEP: 13506-900, SP, Brazil
[b] Departamento de Matemática, Univ. Estadual Paulista - Unesp, Av.24A, 1515, Bela Vista, Rio Claro, CEP: 13506-900, SP, Brazil
[c] Universidade Paulista (UNIP), Instituto de Ciências Exatas e Tecnologia, Rua Miguel Guidoti, 405, Parque Egisto Ragazzo, Limeira, CEP: 13485342, SP, Brazil

ARTICLE INFO

Keywords:
Chaotic diffusion
Stickiness effect
Survival probability

ABSTRACT

Diffusive processes usually model the transport of particles in nonlinear systems. Complete chaos leads to normal diffusion, while mixed phase space gives rise to a phenomenon called stickiness, leading to anomalous diffusion. We investigate the survival probability that a particle moving along a chaotic region in a mixed-phase space has to survive a specific domain. We show along the chaotic part far from islands that an exponential decay describes the survival probability. Nonetheless, when the islands are incorporated into the domain, the survival probability exhibits an exponential decay for a short time, changing to a slower decay for a considerable enough time. This changeover is a signature of stickiness. We solve the diffusion equation by obtaining the probability density to observe a given particle along a specific region within a certain time interval. Integrating the probability density for a defined phase space area provides analytical survival probability. Numerical simulations fit well the analytical findings for the survival probability when the region is fully chaotic. However, the agreement could be better when mixed structure with islands and periodic areas are included in the domain.

1. Introduction

Hamiltonian systems are a class of dynamical systems in classical mechanics that describe the motion of particles or objects based on energy conservation which has been studied for centuries, with seminal contributions from mathematicians such as Lagrange, Jacobi, and Poincaré. In integrable Hamiltonian systems, the motion of particles is predictable and follows regular patterns, allowing for the system's complete solution through algebraic or geometric methods. In this case, the number of constants of motion equals the degrees of freedom marked by the number of canonical variables pairs (e.g., position and momentum).

However, not all Hamiltonian systems are integrable, and the behavior of non-integrable systems can be much more complex and difficult to predict. Generally, Hamiltonian systems are, usually, non-integrable and non-ergodic [1–3]. Non-integrability arises due to non-linearities or perturbations in the Hamiltonian equations, which lead to chaotic behavior and a breakdown of predictability. In this context, non-integrable Hamiltonian systems have become an essential topic of research in modern mathematics and physics, with significant implications in fields such as celestial mechanics [4], plasma physics [5], and quantum mechanics [6,7].

A powerful observable in the study of the statistical properties of the transport is the survival probability, that is, the probability that a diffusing particle remains in a determined region at some time. To study chaotic Hamiltonian systems, we can divide the analysis into two groups [8]. In the case of fully chaotic systems, the decay over time follows an exponential pattern: $P(\tau) \sim e^{-\frac{\tau}{\tau_s}}$ [9]. However, most physically realistic systems are a mixture of chaotic and regular dynamics in the phase space. In these systems, there is the stickiness effect, where the particles tendency to stick to regular regions, resulting in the probability $P(\tau)$ decays by a power law: $P(\tau) \sim \tau^{-\gamma}$ [10]. This statistic is associated with anomalous transport [11,12], that is, a diffusive process where the mean square displacement increases with a power β of τ that is not equal to 1 $\left\langle (\Delta_\tau x)^2 \right\rangle \sim \tau^\beta$, where $x(\tau)$ represents dynamical variable which presents anomalous diffusion [13,14]. This observation has motivated the adoption of appropriate statistical theories like fractional kinetics [15–17] and continuous-time random walk (CTRW) [18–20] to describe such systems. Furthermore, both exponents can be related by relationship $\gamma + \beta \approx 3$ [9]. This paper considers a family of two-dimensional, nonlinear, and area-preserving maps described by the angle θ and action I variables. The nonlinear term is given by a sine function controlled by a parameter ϵ. For $\epsilon = 0$,

* Corresponding author at: Departamento de Física, Univ. Estadual Paulista - Unesp, Av.24A, 1515, Bela Vista, Rio Claro, CEP: 13506-900, SP, Brazil.
E-mail address: daniel.borin@unesp.br (D. Borin).
[1] The authors contributed equally on the manuscript.

https://doi.org/10.1016/j.chaos.2023.113965
Received 19 April 2023; Received in revised form 12 July 2023; Accepted 21 August 2023
Available online 2 September 2023
0960-0779/© 2023 Elsevier Ltd. All rights reserved.

Bibliography

[1] V. Afraimovich and G. M. Zaslavsky. Sticky orbits of chaotic hamiltonian dynamics. In S. Benkadda and G. M. Zaslavsky, editors, *Chaos, Kinetics and Nonlinear Dynamics in Fluids and Plasmas*, pages 59–82, Berlin, Heidelberg, 1998. Springer Berlin Heidelberg.

[2] E. Alessio, A. Carbone, G. Castelli, and V. Frappietro. Second-order moving average and scaling of stochastic time series. *The European Physical Journal B-Condensed Matter and Complex Systems*, 27(2):197–200, 2002.

[3] K. T. Alligood, T. D. Sauer, and J. A. Yorke. Chaos: an introduction to dynamical systems, 1997.

[4] E. G. Altmann, A. E. Motter, and H. Kantz. Stickiness in mushroom billiards. *Chaos: An Interdisciplinary Journal of Nonlinear Science*, 15(3):033105, 2005.

[5] E. G. Altmann, A. E. Motter, and H. Kantz. Stickiness in hamiltonian systems: From sharply divided to hierarchical phase space. *Phys. Rev. E*, 73:026207, 2006.

[6] V. Anishchenko, A. Kopeikin, J. Kurths, T. Vadivasova, and G. Strelkova. Studying hyperbolicity in chaotic systems. *Physics Letters A*, 270(6):301–307, 2000.

[7] V. I. Arnold. Proof of a theorem of a. n. kolmogorov on the invariance of quasi-periodic motions under small perturbations of the hamiltonian. *Russian Mathematical Surveys*, 18(5):9–36, 1963.

[8] V. I. Arnold. *Mathematical Methods of Classical Mechanics*. Springer, New York, 2 edition, 1989.

[9] D. Assaf and S. Gadbois. Definition of chaos. *American Mathematical Monthly*, 99(9):865–865, 1992.

[10] K. G. Atman and H. Şirin. Nonlocal phenomena in quantum mechanics with fractional calculus. *Reports on Mathematical Physics*, 86(2):263–270, 2020.

[11] J. Banks, J. Brooks, G. Cairns, G. Davis, and P. Stacey. On devaney's definition of chaos. *The American Mathematical Monthly*, 99(4):332–334, 1992.

[12] G. Benettin, L. Galgani, A. Giorgilli, and J. M. Strelcyn. Lyapunov characteristic exponents for smooth dynamical systems and for hamiltonian systems; a method for computing all of them. part 1: Theory. *Meccanica*, 15:9–20, 1980.

[13] G. Benettin, L. Galgani, and J.-M. Strelcyn. Kolmogorov entropy and numerical experiments. *Phys. Rev. A*, 14(6):2338, 1976.

[14] M. Berry. Regular and irregular motion. *AIP Conference Proceedings*, 46(1):16–120, 1978.

[15] R. Bevilacqua, O. Menchi, A. Milani, A. Nobili, and P. Farinella. Resonances and close approaches. i. the titan-hyperion case. *The moon and the planets*, 22(2):141–152, 1980.

[16] R. N. Bhattacharya, V. K. Gupta, and E. Waymire. The hurst effect under trends. *Journal of applied probability*, 20(3):649–662, 1983.

[17] N. Boccara. *Modeling Complex Systems*. Springer New York, New York, NY, 2004.

[18] D. Borin. Caputo fractional standard map: Scaling invariance analyses. *Chaos, Solitons & Fractals*, 181:114597, 2024.

[19] D. Borin. Equações diferenciais e modelagem de alguns fenômenos físicos. Master's thesis, Universidade Estadual Paulista (Unesp), 2024.

[20] D. Borin. Hurst exponent: A method for characterizing dynamical traps. *Phys. Rev. E*, 110:064227, 2024.

[21] D. Borin, V. L. G. de Brito, E. D. Leonel, and M. Hansen. Buzz pollination: A theoretical analysis via scaling invariance. *Phys. Rev. E*, 110(5):054201, 2024.

[22] D. Borin, E. D. Leonel, and D. F. M. de Oliveira. Survival probability of particles inside the lemon billiard. *Phys. Rev. E*, 114:014224, 2026.

[23] D. Borin, A. L. P. Livorati, and E. D. Leonel. An investigation of the survival probability for chaotic diffusion in a family of discrete Hamiltonian mappings. *Chaos, Solitons & Fractals*, 175:113965, 2023.

[24] D. Borin and D. F. Oliveira. Self-similar shrimp structures and bifurcation hierarchies in the gumowski–mira map. *Physica A: Statistical Mechanics and its Applications*, 700:131892, 2026.

[25] D. Borin, D. S. Rando, E. D. Leonel, and D. F. M. de Oliveira. Convergence dynamics and scaling laws in the dissipative relativistic kicked rotator. *European Physical Journal Special Topics*, 2026.

[26] D. Borin, M. Rolim Sales, E. D. Leonel, and D. F. M. de Oliveira. On the dynamics of the q-tsallis gauss iterated map. *Physica A: Statistical Mechanics and its Applications*, 686:131352, 2026.

[27] D. Borin, J. D. Szezech, and M. R. Sales. Characterizing and quantifying weak chaos in fractional dynamics. *Chaos, Solitons & Fractals*, 200:117137, 2025.

[28] W. E. Boyce and R. C. DiPrima. *Elementary Differential Equations and Boundary Value Problems*. Wiley, 11 edition, 2017.

[29] M. Braun. *Differential Equations and Their Applications*. Springer, 4 edition, 1993.

[30] R. L. Burden and J. D. Faires. *Numerical Analysis*. Brooks/Cole, Cengage Learning, Boston, MA, 9 edition, 2011.

[31] A. B. Cambel. *Applied Chaos Theory: A Paradigm for Complexity*. Academic Press, San Diego, CA, 1993.

[32] A. Carbone, G. Castelli, and H. Stanley. Time-dependent hurst exponent in financial time series. *Physica A: Statistical Mechanics and its Applications*, 344(1):267–271, 2004.

[33] M. Casartelli, E. Diana, L. Galgani, and A. Scotti. Numerical computations on a stochastic parameter related to the kolmogorov entropy. *Phys. Rev. A*, 13(5):1921, 1976.

[34] G. Casati and J. Ford. Stochastic transition in the unequal-mass toda lattice. *Phys. Rev. A*, 12(4):1702, 1975.

[35] B. Chirikov and D. Shepelyansky. Correlation properties of dynamical chaos in hamiltonian systems. *Physica D: Nonlinear Phenomena*, 13(3):395–400, 1984.

[36] B. V. Chirikov. A universal instability of many-dimensional oscillator systems. *Physics Reports*, 52(5):263–379, 1979.

[37] B. V. Chirikov and D. L. Shepelyansky. Asymptotic statistics of poincaré recurrences in hamiltonian systems with divided phase space. *Phys. Rev. Lett.*, 82:528–531, 1999.

[38] E. A. Coddington and N. Levinson. *Theory of Ordinary Differential Equations*. McGraw-Hill, New York, 1955.

[39] G. Contopoulos. Orbits in highly perturbed dynamical systems. iii. nonperiodic orbits. *Astronomical Journal*, 76:147, 1971.

[40] M. Couillard and M. Davison. A comment on measuring the hurst exponent of financial time series. *Physica A: Statistical Mechanics and its Applications*, 348:404–418, 2005.

[41] G. Cristadoro and R. Ketzmerick. Universality of algebraic decays in hamiltonian systems. *Phys. Rev. Lett.*, 100:184101, 2008.

[42] D. R. da Costa, A. Fujita, A. M. Batista, M. R. Sales, and J. D. Szezech Jr. Conservative generalized bifurcation diagrams and phase space properties for oval-like billiards. *Chaos, Solitons & Fractals*, 155:111707, 2022.

[43] R. M. da Silva, C. Manchein, M. W. Beims, and E. G. Altmann. Characterizing weak chaos using time series of lyapunov exponents. *Phys. Rev. E*, 91:062907, 2015.

[44] I. Dana. Kicked harper models and kicked charge in a magnetic field. *Physics Letters A*, 197(5):413–416, 1995.

[45] S. Das, C. B. Dock, Y. Saiki, M. Salgado-Flores, E. Sander, J. Wu, and J. A. Yorke. Measuring quasiperiodicity. *Europhysics Letters*, 114(4):40005, 2016.

[46] S. Das and J. A. Yorke. Super convergence of ergodic averages for quasiperiodic orbits. *Nonlinearity*, 31(2):491, 2018.

[47] M. A. de Aguiar. Tópicos de mecânica clássica. *Editora Livraria da Fısica, Sao Paulo*, 2011.

[48] R. Devaney. *An introduction to chaotic dynamical systems*. CRC press, 2018.

[49] D. Ding, J. Wang, M. Wang, Z. Yang, W. Wang, Y. Niu, and X. Xu. Controllable multistability of fractional-order memristive coupled chaotic map and its application in medical image encryption. *The European Physical Journal Plus*, 138(10):908, 2023.

[50] P. Doukhan, G. Oppenheim, and M. Taqqu. *Theory and applications of long-range dependence*. Springer Science & Business Media, 2002.

[51] J. P. Eckmann and D. Ruelle. Ergodic theory of chaos and strange attractors. *Rev. Mod. Phys.*, 57:617–656, 1985.

[52] M. Edelman. Fractional standard map: Riemann–liouville vs. caputo. *Communications in Nonlinear Science and Numerical Simulation*, 16(12):4573–4580, 2011.

[53] M. Edelman. Universal fractional map and cascade of bifurcations type attractors. *Chaos: An Interdisciplinary Journal of Nonlinear Science*, 23(3):033127, 2013.

[54] M. Edelman. *Evolution of Systems with Power-Law Memory: Do We Have to Die? (Dedicated to the Memory of Valentin Afraimovich)*, pages 65–85. Springer International Publishing, Cham, 2020.

[55] M. Edelman. Stability of fixed points in generalized fractional maps of the orders 0< α< 1. *Nonlinear Dynamics*, 111(11):10247–10254, 2023.

[56] M. Edelman and A. B. Helman. Asymptotic cycles in fractional maps of arbitrary positive orders. *Fractional Calculus and Applied Analysis*, 25(1):181–206, 2022.

[57] M. Edelman, A. B. Helman, and R. Smidtaite. Bifurcations and transition to chaos in generalized fractional maps of the orders $0 < \alpha < 1$. *Chaos: An Interdisciplinary Journal of Nonlinear Science*, 33(6):063123, 2023.

[58] M. Edelman and L. A. Taieb. New types of solutions of non-linear fractional differential equations. In *Advances in Harmonic Analysis and Operator Theory: The Stefan Samko Anniversary Volume*, pages 139–155. Springer, 2013.

[59] M. Edelman and V. E. Tarasov. Fractional standard map. *Physics Letters A*, 374(2):279–285, 2009.

[60] C. Efthymiopoulos, G. Contopoulos, N. Voglis, and R. Dvorak. Stickiness and cantori. *Journal of Physics A: Mathematical and General*, 30(23):8167, 1997.

[61] S. N. Evangelou and J.-L. Pichard. Critical quantum chaos and the one-dimensional harper model. *Phys. Rev. Lett.*, 84:1643–1646, 2000.

[62] E. Fermi. On the origin of the cosmic radiation. *Phys. Rev.*, 75:1169–1174, 1949.

[63] U. Feudel, C. Grebogi, B. R. Hunt, and J. A. Yorke. Map with more than 100 coexisting low-period periodic attractors. *Phys. Rev. E*, 54:71–81, 1996.

[64] J. Ford and G. H. Lunsford. Stochastic behavior of resonant nearly linear oscillator systems in the limit of zero nonlinear coupling. *Phys. Rev. A*, 1(1):59, 1970.

[65] C. Froeschlé. Numerical study of dynamical systems with three degrees of freedom. ii. numerical displays of four-dimensional sections. *Astronomy and Astrophysics*, 5:177, 1970.

[66] C. Froeschlé. Numerical study of a four-dimensional mapping. *Astronomy and Astrophysics*, 16:172, 1972.

[67] T. Geisel, R. Ketzmerick, and G. Petschel. New class of level statistics in quantum systems with unbounded diffusion. *Phys. Rev. Lett.*, 66:1651–1654, 1991.

[68] J. Geweke and S. Porter-Hudak. The estimation and application of long memory time series models. *Journal of Time Series Analysis*, 4(4):221–238, 1983.

[69] H. Goldstein. *Classical mechanics*, volume 2. Addison-wesley Reading, MA, 1950.

[70] P. Grassberger and H. Kantz. Universal scaling of long-time tails in hamiltonian systems? *Physics Letters A*, 113(4):167–171, 1985.

[71] D. Grech and Z. Mazur. Can one make any crash prediction in finance using the local hurst exponent idea? *Physica A: Statistical Mechanics and its Applications*, 336(1):133–145, 2004.

[72] J. M. Greene. Two-dimensional measure-preserving mappings. *Journal of Mathematical Physics*, 9(5):760–768, 1968.

[73] J. M. Greene. A method for determining a stochastic transition. *Journal of Mathematical Physics*, 20(6):1183–1201, 1979.

[74] J. M. Greene. A method for determining a stochastic transition. *Journal of Mathematical Physics*, 20(6):1183–1201, 1979.

[75] D. M. Grobman. Homeomorphisms of systems of differential equations. *Doklady Akademii Nauk SSSR*, 128:880–881, 1959.

[76] W. R. Hamilton. On a general method in dynamics. *Philosophical Transactions of the Royal Society*, pages 247–308, 1834. Also in Mathematical Papers, Vol. 2, pp. 103–161.

[77] W. R. Hamilton. Second essay on a general method in dynamics. *Philosophical Transactions of the Royal Society*, pages 95–144, 1835. Also in Mathematical Papers, Vol. 2, pp. 162–211.

[78] M. Harle and U. Feudel. Hierarchy of islands in conservative systems yields multimodal distributions of ftles. *Chaos, Solitons & Fractals*, 31(1):130–137, 2007.

[79] P. G. Harper. Single band motion of conduction electrons in a uniform magnetic field. *Proceedings of the Physical Society. Section A*, 68(10):874, 1955.

[80] P. Hartman. A lemma in the theory of structural stability of differential equations. *Proceedings of the American Mathematical Society*, 11:610–620, 1960.

[81] P. Hartman. *Ordinary Differential Equations*. SIAM, 2002.

[82] M. Hénon and C. Heiles. The applicability of the third integral of motion: some numerical experiments. *Astronomical Journal*, 69:73, 1964.

[83] M. Hirata, B. Saussol, and S. Vaienti. Statistics of return times: A general framework and new applications. *Communications in Mathematical Physics*, 206:33–55, Sept. 1999.

[84] D. R. Hofstadter. Energy levels and wave functions of bloch electrons in rational and irrational magnetic fields. *Phys. Rev. B*, 14:2239–2249, 1976.

[85] H. E. Hurst. Long-term storage capacity of reservoirs. *Transactions of the American Society of Civil Engineers*, 116(1):770–799, 1951.

[86] H. E. Hurst. Methods of using long-term storage in reservoirs. *Proceedings of the institution of civil engineers*, 5(5):519–543, 1956.

[87] H. E. Hurst. A suggested statistical model of some time series which occur in nature. *Nature*, 180(4584):494–494, 1957.

[88] H. E. Hurst, R. P. Black, and Y. M. Simaika. *Long-Term Storage: An Experimental Study*. Constable, London, 1965.

[89] R. Ishizaki, T. Horita, T. Kobayashi, and H. Mori. Anomalous diffusion due to accelerator modes in the standard map. *Progress of Theoretical Physics*, 85(5):1013–1022, 1991.

[90] C. G. J. Jacobi. Ueber ein neues integral für den fall der drei körper, 1836. Monatsbericht der Königlichen Preußischen Akademie der Wissenschaften zu Berlin, pp. 59–60.

[91] C. G. J. Jacobi. Zur theorie der variations-rechnung und der differential-gleichungen. *Journal für die reine und angewandte Mathematik*, 17:68–82, 1837. Also in Werke, Vol. 4, pp. 39–55.

[92] A. Jan, S. Boulaaras, F. A. Abdullah, and R. Jan. Dynamical analysis, infections in plants, and preventive policies utilizing the theory of fractional calculus. *The European Physical Journal Special Topics*, 232(14):2497–2512, 2023.

[93] C. F. Karney. Long-time correlations in the stochastic regime. *Physica D: Nonlinear Phenomena*, 8(3):360–380, 1983.

[94] C. F. F. Karney. Stochastic ion heating by a lower hybrid wave: II. *The Physics of Fluids*, 22(11):2188–2209, 1979.

[95] A. A. Khennaoui, V.-T. Pham, V. P. Thoai, A. Ouannas, G. Grassi, and S. Momani. From lozi map to fractional memristive lozi map. *The European Physical Journal Special Topics*, 232(14):2385–2393, 2023.

[96] A. Y. Khinchin. *Continued Fractions*. The University of Chicago Press, 1964.

[97] A. A. Kilbas, H. M. Srivastava, and J. J. Trujillo. *Theory and applications of fractional differential equations*, volume 204. elsevier, 2006.

[98] V. Klemeš. The hurst phenomenon: A puzzle? *Water Resources Research*, 10(4):675–688, 1974.

[99] A. N. Kolmogorov. On conservation of conditionally periodic motions for a small change in hamilton's function. *Doklady Akademii Nauk SSSR*, 98:527–530, 1954.

[100] T. Kruger, L. D. Pustyl'nikov, and S. E. Troubetzkoy. Acceleration of bouncing balls in external fields. *Nonlinearity*, 8(3):397, 1995.

[101] T. S. Krüger, P. P. Galuzio, T. d. L. Prado, R. L. Viana, J. D. Szezech, and S. R. Lopes. Mechanism for stickiness suppression during extreme events in hamiltonian systems. *Phys. Rev. E*, 91:062903, 2015.

[102] S. Lahmiri. A nonlinear analysis of cardiovascular diseases using multi-scale analysis and generalized hurst exponent. *Healthcare Analytics*, 3:100142, 2023.

[103] W.-S. Lam, W. Ray, P. N. Guzdar, and R. Roy. Measurement of hurst exponents for semiconductor laser phase dynamics. *Phys. Rev. Lett.*, 94:010602, 2005.

[104] P.-S. Laplace. *Essai philosophique sur les probabilités*. Courcier, Paris, 1814.

[105] N. Laskin. Fractional schrödinger equation. *Phys. Rev. E*, 66:056108, 2002.

[106] N. Laskin. Time fractional quantum mechanics. *Chaos, Solitons & Fractals*, 102:16–28, 2017.

[107] P. Leboeuf, J. Kurchan, M. Feingold, and D. P. Arovas. Phase-space localization: Topological aspects of quantum chaos. *Phys. Rev. Lett.*, 65:3076–3079, 1990.

[108] P. Leboeuf, J. Kurchan, M. Feingold, and D. P. Arovas. Topological aspects of quantum chaos. *Chaos: An Interdisciplinary Journal of Nonlinear Science*, 2(1):125–130, 1992.

[109] P. Lebœuf. Normal and anomalous diffusion in a deterministic area-preserving map. *Physica D: Nonlinear Phenomena*, 116(1):8–20, 1998.

[110] E. D. Leonel and A. L. Livorati. Thermodynamics of a bouncer model: A simplified one-dimensional gas. *Communications in Nonlinear Science and Numerical Simulation*, 20(1):159–173, 2015.

[111] A. Letnikov. On the historical development of the theory of differentiation with arbitrary index. *Sbornik Mathematics (Matematicheskii Sbornik)*, 3(2):85–112, 1868.

[112] B. Lévi and B. Georgeot. Quantum computation of a complex system: The kicked harper model. *Phys. Rev. E*, 70:056218, 2004.

[113] C. Li and G. Chen. Estimating the lyapunov exponents of discrete systems. *Chaos: An Interdisciplinary Journal of Nonlinear Science*, 14(2):343–346, 2004.

[114] H. Li, Y. Shen, Y. Han, J. Dong, and J. Li. Determining Lyapunov exponents of fractional-order systems: A general method based on memory principle. *Chaos, Solitons & Fractals*, 168:113167, 2023.

[115] T.-Y. Li and J. A. Yorke. Period three implies chaos. *The American Mathematical Monthly*, 82(10):985–992, 1975.

[116] A. J. Lichtenberg and M. A. Lieberman. *Regular and chaotic dynamics*, volume 38. Springer Science & Business Media, 2013.

[117] A. J. Lichtenberg and B. P. Wood. Diffusion on two space and time scales. *Phys. Rev. Lett.*, 62:2213–2216, 1989.

[118] A. J. Lichtenberg and B. P. Wood. Diffusion through a stochastic web. *Phys. Rev. A*, 39:2153–2159, 1989.

[119] M. Lieberman and V. Godyak. From fermi acceleration to collisionless discharge heating. *IEEE Transactions on Plasma Science*, 26(3):955–986, 1998.

[120] M. A. Lieberman and A. J. Lichtenberg. Stochastic and adiabatic behavior of particles accelerated by periodic forces. *Phys. Rev. A*, 5:1852–1866, Apr 1972.

[121] S. Lim. Fractional derivative quantum fields at positive temperature. *Physica A: Statistical Mechanics and its Applications*, 363(2):269–281, 2006.

[122] R. Lima and D. Shepelyansky. Fast delocalization in a model of quantum kicked rotator. *Phys. Rev. Lett.*, 67:1377–1380, 1991.

[123] A. L. P. Livorati, A. P. Faber, and D. Borin. Asymptotic convergence for the dynamics of a Duffing-like oscillator under scaling analyses. *Chaos*, 35(1):013108, 2025.

[124] A. L. P. Livorati, T. Kroetz, C. P. Dettmann, I. L. Caldas, and E. D. Leonel. Stickiness in a bouncer model: A slowing mechanism for fermi acceleration. *Phys. Rev. E*, 86:036203, 2012.

[125] A. L. P. Livorati, D. G. Ladeira, and E. D. Leonel. Scaling investigation of fermi acceleration on a dissipative bouncer model. *Phys. Rev. E*, 78:056205, 2008.

[126] E. Lloyd. Stochastic reservoir theory. *Advances in hydroscience*, 4:281–339, 1967.

[127] S. R. Lopes, J. D. Szezech, R. F. Pereira, A. A. Bertolazzo, and R. L. Viana. Anomalous transport induced by nonhyperbolicity. *Phys. Rev. E*, 86:016216, 2012.

[128] A. M. Lyapunov. The general problem of the stability of motion. *International journal of control*, 55(3):531–534, 1992.

[129] T. Ma, J. Mou, S. Banerjee, and Y. Cao. Analysis of the functional behavior of fractional-order discrete neuron under electromagnetic radiation. *Chaos, Solitons & Fractals*, 176:114113, 2023.

[130] J. T. Machado, V. Kiryakova, and F. Mainardi. Recent history of fractional calculus. *Communications in Nonlinear Science and Numerical Simulation*, 16(3):1140–1153, 2011.

[131] R. MacKay and J. Meiss. Survey of hamiltonian dynamics. In *Hamiltonian Dynamical Systems*, pages 3–19. CRC Press, 2020.

[132] R. Mackay, J. Meiss, and I. Percival. Transport in hamiltonian systems. *Physica D: Nonlinear Phenomena*, 13(1):55–81, 1984.

[133] R. S. MacKay, J. D. Meiss, and I. C. Percival. Stochasticity and transport in hamiltonian systems. *Phys. Rev. Lett.*, 52:697–700, 1984.

[134] S. Majee, S. Barman, A. Khatua, T. Kar, and S. Jana. The impact of media awareness on a fractional-order seir epidemic model with optimal treatment and vaccination. *The European Physical Journal Special Topics*, 232(14):2459–2483, 2023.

[135] C. Manchein and M. W. Beims. Conservative generalized bifurcation diagrams. *Physics Letters A*, 377(10):789–793, 2013.

[136] B. Mandelbrot. Une classe de processus stochastiques homothetiques a soi-application a la loi climatologique de he hurst. *Comptes Rendus Hebdomadaires des Seances de l Academie des Sciences*, 260(12):3274, 1965.

[137] B. B. Mandelbrot. Limit theorems on the self-normalized range for weakly and strongly dependent processes. *Zeitschrift für Wahrscheinlichkeitstheorie und verwandte Gebiete*, 31(4):271–285, 1975.

[138] B. B. Mandelbrot and J. W. Van Ness. Fractional brownian motions, fractional noises and applications. *SIAM review*, 10(4):422–437, 1968.

[139] B. B. Mandelbrot and J. R. Wallis. Noah, joseph, and operational hydrology. *Water Resources Research*, 4(5):909–918, 1968.

[140] B. B. Mandelbrot and J. R. Wallis. Robustness of the rescaled range r/s in the measurement of noncyclic long run statistical dependence. *Water Resources Research*, 5(5):967–988, 1969.

[141] B. B. Mandelbrot and J. R. Wallis. Some long-run properties of geophysical records. *Water resources research*, 5(2):321–340, 1969.

[142] T. Manos and M. Robnik. Survey on the role of accelerator modes for anomalous diffusion: The case of the standard map. *Phys. Rev. E*, 89:022905, 2014.

[143] N. C. Matalas and C. S. Huzzen. A property of the range of partial sums. In *Proceedings of the International Hydrology Symposium*, volume 1, pages 252–257, 1967.

[144] J. A. Matos, S. M. Gama, H. J. Ruskin, A. A. Sharkasi, and M. Crane. Time and scale hurst exponent analysis for financial markets. *Physica A: Statistical Mechanics and its Applications*, 387(15):3910–3915, 2008.

[145] J. D. Meiss, J. R. Cary, C. Grebogi, J. D. Crawford, A. N. Kaufman, and H. D. Abarbanel. Correlations of periodic, area-preserving maps. *Physica D: Nonlinear Phenomena*, 6(3):375–384, 1983.

[146] K. Miller and B. Ross. *An Introduction to the Fractional Calculus and Fractional Differential Equations*. Wiley, 1993.

[147] P. A. P. Moran. *The Theory of Storage*. Wiley, New York, 1959.

[148] M. A. Moreles and R. Lainez. Mathematical modelling of fractional order circuit elements and bioimpedance applications. *Communications in Nonlinear Science and Numerical Simulation*, 46:81–88, 2017.

[149] J. Moser. On invariant curves of area-preserving mappings of an annulus. *Nachrichten der Akademie der Wissenschaften in Göttingen, II. Mathematisch-Physikalische Klasse*, pages 1–20, 1962.

[150] M. Nakane and C. G. Fraser. The early history of the hamilton-jacobi dynamics: 1834–1837. *Centaurus*, 44:161–183, 2002.

[151] P. E. O'Connell. A simple stochastic model of hurst's law. *Mathematical Models in Hydrology*, 1(100):169–187, 1971.

[152] T. Okushima. New method for computing finite-time lyapunov exponents. *Phys. Rev. Lett.*, 91:254101, 2003.

[153] U. Orinaite, I. Telksniene, T. Telksnys, and M. Ragulskis. How does the fractional derivative change the complexity of the caputo standard fractional map. *International Journal of Bifurcation and Chaos*, 34(07):2450085, 2024.

[154] V. I. Oseledec. A multiplicative ergodic theorem, lyapunov characteristic numbers for dynamical systems. *Transactions of the Moscow Mathematical Society*, 19:197–231, 1968.

[155] E. Ott. *Chaos in Dynamical Systems*. Cambridge University Press, 2 edition, 2002.

[156] A. Ouannas, X. Wang, A.-A. Khennaoui, S. Bendoukha, V.-T. Pham, and F. E. Alsaadi. Fractional form of a chaotic map without fixed points: Chaos, entropy and control. *Entropy*, 20(10):720, 2018.

[157] J. Palis and W. de Melo. *Geometric Theory of Dynamical Systems: An Introduction*. Springer, New York, 1982.

[158] M. S. Palmero and I. L. Caldas. Confining and escaping magnetic field lines in tokamaks: Analysis via symplectic maps. *Fundamental Plasma Physics*, 8:100027, 2023.

[159] G. Park and C. S. Chang. Diffusion by extrinsic noise in the kicked harper map. *Phys. Rev. E*, 63:066213, 2001.

[160] T. Parker and L. Chua. Chaos: A tutorial for engineers. *Proceedings of the IEEE*, 75(8):982–1008, 1987.

[161] R. A. Pasmanter. From chaotic advection to chaotic schrödinger-type equations. *Phys. Rev. A*, 42:3622–3625, 1990.

[162] C.-K. Peng, S. V. Buldyrev, S. Havlin, M. Simons, H. E. Stanley, and A. L. Goldberger. Mosaic organization of dna nucleotides. *Phys. Rev. E*, 49:1685–1689, 1994.

[163] Y. B. Pesin. Characteristic lyapunov exponents and smooth ergodic theory. *Russian mathematical surveys*, 32(4):55–114, 1977.

[164] H. Poincaré. Sur le problème des trois corps et les équations de la dynamique. *Acta mathematica*, 13(1):A3–A270, 1890.

[165] H. Poincaré. *Les méthodes nouvelles de la mécanique céleste*. Gauthier-Villars, Paris, 1 edition, 1899.

[166] L. S. Pontryagin. *Ordinary Differential Equations*. Mir Publishers, Moscow, 1969.

[167] L. D. Pustyl'nikov. Existence of a set of positive measure of oscillating motions in a certain problem of dynamics. *Doklady Akademii Nauk*, 202(2):287–289, 1972.

[168] L. D. Pustyl'nikov. Stable and oscillating motions in nonautonomous dynamical systems. a generalization of c. l. siegel's theorem to the nonautonomous case. *Mathematics of the USSR-Sbornik*, 23(3):382, 1974.

[169] L. Ren, L. Qin, H. Jahanshahi, and J. Mou. Infinitely many coexisting attractors and scrolls in a fractional-order discrete neuron map. *International Journal of Bifurcation and Chaos*, 33(16):2350197, 2023.

[170] W. Rippl. The capacity of storage reservoirs for water supply. *Van Nostrand's Engineering Magazine (1879-1886)*, 29(175):67, 1883.

[171] I. Rodriguez-Iturbe, J. M. Mejia, and D. R. Dawdy. Streamflow simulation: 1. a new look at markovian models, fractional gaussian noise, and crossing theory. *Water Resources Research*, 8(4):921–930, 1972.

[172] B. Rojo-Garibaldi, A. I. Aguilar-Hernández, and G. Martínez–Mekler. Nonlinear comparative analysis of Greenland and Antarctica ice cores data. *Chaos: An Interdisciplinary Journal of Nonlinear Science*, 34(8):083123, 2024.

[173] M. Rolim Sales, D. Borin, D. R. da Costa, J. D. Szezech, and E. D. Leonel. An investigation of escape and scaling properties of a billiard system. *Chaos*, 34(11):113122, 2024.

[174] M. Rolim Sales, D. Borin, L. C. de Souza, J. D. Szezech, R. L. Viana, I. L. Caldas, and E. D. Leonel. Ratchet current and scaling properties in a nontwist mapping. *Chaos, Solitons & Fractals*, 189:115614, 2024.

[175] M. R. Sales, L. C. de Souza, D. Borin, M. Mugnaine, J. D. Szezech, R. L. Viana, I. L. Caldas, E. D. Leonel, and C. G. Antonopoulos. pynamicalsys: A python toolkit for the analysis of dynamical systems. *Chaos, Solitons & Fractals*, 201:117269, 2025.

[176] M. R. Sales, M. Mugnaine, J. D. Szezech Jr., R. L. Viana, I. L. Caldas, N. Marwan, and J. Kurths. Stickiness and recurrence plots: An entropy-based approach. *Chaos: An Interdisciplinary Journal of Nonlinear Science*, 33(3):033140, 2023.

[177] M. Sano and Y. Sawada. Measurement of the lyapunov spectrum from a chaotic time series. *Phys. Rev. Lett.*, 55:1082–1085, 1985.

[178] A. B. Schelin and K. H. Spatschek. Directed chaotic transport in the tokamap with mixed phase space. *Phys. Rev. E*, 81:016205, 2010.

[179] Y. Scher, S. Reuveni, and D. S. Grebenkov. Escape of a sticky particle. *Phys. Rev. Res.*, 5:043196, 2023.

[180] I. Shimada and T. Nagashima. A numerical approach to ergodic problem of dissipative dynamical systems. *Progress of Theoretical Physics*, 61(6):1605–1616, 1979.

[181] S. Shinohara. The threshold for global diffusion in the kicked harper map. *Physics Letters A*, 298(5):330–334, 2002.

[182] M. Siddiqui. The asymptotic distribution of the range and other functions of partial sums of stationary processes. *Water Resources Research*, 12(6):1271–1276, 1976.

[183] R. Sikora and S. Pawłowski. Fractional derivatives and the laws of electrical engineering. *COMPEL-The international journal for computation and mathematics in electrical and electronic engineering*, 37(4):1384–1391, 2018.

[184] R. Sikora and S. Pawlowski. On certain aspects of application of fractional derivatives in the electromagnetism. *Przeglad Elektrotechniczny*, 94(1):101–104, 2018.

[185] S. Smale. Differentiable dynamical systems. *Bulletin of the American Mathematical Society*, 73(6):747–817, 1967.

[186] T. P. Stefański and J. Gulgowski. Electromagnetic-based derivation of fractional-order circuit theory. *Communications in Nonlinear Science and Numerical Simulation*, 79:104897, 2019.

[187] T. P. Stefański and J. Gulgowski. Signal propagation in electromagnetic media described by fractional-order models. *Communications in Nonlinear Science and Numerical Simulation*, 82:105029, 2020.

[188] S. D. Stoddard and J. Ford. Numerical experiments on the stochastic behavior of a lennard-jones gas system. *Phys. Rev. A*, 8(3):1504, 1973.

[189] S. H. Strogatz. *Nonlinear dynamics and chaos: with applications to physics, biology, chemistry, and engineering*. Chapman and Hall/CRC, 2024.

[190] J. Sutcliffe, S. Hurst, A. G. Awadallah, E. Brown, and K. Hamed. Harold edwin hurst: the nile and egypt, past and future. *Hydrological Sciences Journal*, 61(9):1557–1570, 2016.

[191] J. Szezech, S. Lopes, and R. Viana. Finite-time lyapunov spectrum for chaotic orbits of non-integrable hamiltonian systems. *Physics Letters A*, 335(5):394–401, 2005.

[192] J. Szezech, A. Schelin, I. Caldas, S. Lopes, P. Morrison, and R. Viana. Finite-time rotation number: A fast indicator for chaotic dynamical structures. *Physics Letters A*, 377(6):452–456, 2013.

[193] M. Tabor. *Chaos and Integrability in Nonlinear Dynamics: An Introduction*. John Wiley & Sons, New York, 1989.

[194] V. E. Tarasov. Differential equations with fractional derivative and universal map with memory. *Journal of Physics A: Mathematical and Theoretical*, 42(46):465102, 2009.

[195] V. E. Tarasov. Discrete map with memory from fractional differential equation of arbitrary positive order. *Journal of Mathematical Physics*, 50(12):122703, 2009.

[196] V. E. Tarasov. General fractional dynamics. *Mathematics*, 9(13), 2021.

[197] V. E. Tarasov. Discrete maps with distributed memory fading parameter. *Computational and Applied Mathematics*, 43(3):113, 2024.

[198] V. E. Tarasov. General fractional economic dynamics with memory. *Mathematics*, 12(15):2411, 2024.

[199] V. E. Tarasov. Periodically kicked rotator with power-law memory: Exact solution and discrete maps. *Fractal and Fractional*, 9(7):472, 2025.

[200] V. E. Tarasov and M. Edelman. Fractional dissipative standard map. *Chaos: An Interdisciplinary Journal of Nonlinear Science*, 20(2):023127, 2010.

[201] V. E. Tarasov and G. M. Zaslavsky. Fractional equations of kicked systems and discrete maps. *Journal of Physics A: Mathematical and Theoretical*, 41(43):435101, 2008.

[202] J. B. Taylor and E. W. Laing. Invariant for a particle interacting with an electrostatic wave in a magnetic field. *Phys. Rev. Lett.*, 35:1306–1307, 1975.

[203] T. Tél and M. Gruiz. *Chaotic dynamics: an introduction based on classical mechanics*. Cambridge University Press, 2006.

[204] V. Teverovsky and M. Taqqu. Testing for long-range dependence in the presence of shifting means or a slowly declining trend, using a variance-type estimator. *Journal of time series analysis*, 18(3):279–304, 1997.

[205] U. Tirnakli, C. Tsallis, and K. Cetin. Dynamical robustness of discrete conservative systems: Harper and generalized standard maps. *Journal of Statistical Mechanics: Theory and Experiment*, 2020(6):063206, 2020.

[206] D. Valério, J. T. Machado, and V. Kiryakova. Some pioneers of the applications of fractional calculus. *Fractional Calculus and Applied Analysis*, 17:552–578, 2014.

[207] M. Vellekoop and R. Berglund. On intervals, transitivity= chaos. *The American Mathematical Monthly*, 101(4):353–355, 1994.

[208] F. Vivaldi, G. Casati, and I. Guarneri. Origin of long-time tails in strongly chaotic systems. *Phys. Rev. Lett.*, 51:727–730, Aug. 1983.

[209] J. R. Wallis and P. E. O'Connell. Firm reservoir yield—how reliable are historic hydrological records? *Hydrological Sciences Bulletin*, 18:347–365, 1973.

[210] M. Wilkinson and R. J. Kay. Semiclassical limits of the spectrum of harper's equation. *Phys. Rev. Lett.*, 76:1896–1899, 1996.

[211] J. Williams and G. Benson. Resonances in the neptune-pluto system. *Astronomical Journal*, 76:167, 1971.

[212] A. Wolf, J. B. Swift, H. L. Swinney, and J. A. Vastano. Determining lyapunov exponents from a time series. *Physica D: Nonlinear Phenomena*, 16(3):285–317, 1985.

[213] W. F. Wreszinski. *Mecânica clássica moderna*. EDUSP, 1997.

[214] G.-C. Wu and D. Baleanu. Jacobian matrix algorithm for Lyapunov exponents of the discrete fractional maps. *Communications in Nonlinear Science and Numerical Simulation*, 22(1):95–100, 2015.

[215] L.-S. Young. Statistical properties of dynamical systems with some hyperbolicity. *Annals of Mathematics*, 147(3):585–650, 1998.

[216] G. Zaslavskii, R. Sagdeev, and A. Chernikov. Stochastic nature of streamlines in steady-state flows. *Zh. eksp. teor. Fiz*, 94:102–15, 1988.

[217] G. Zaslavskii, M. I. Zakharov, A. Neishtadt, R. Sagdeev, and D. Usikov. Multidimensional hamiltonian chaos. *Zhurnal Eksperimentalnoi i Teoreticheskoi Fiziki*, 96:1563–1586, 1989.

[218] G. Zaslavsky. Chaos, fractional kinetics, and anomalous transport. *Physics Reports*, 371(6):461–580, 2002.

[219] G. Zaslavsky. Dynamical traps. *Physica D: Nonlinear Phenomena*, 168-169:292–304, 2002.

[220] G. M. Zaslavsky. Stochastic webs and their applications. *Chaos: An Interdisciplinary Journal of Nonlinear Science*, 1(1):1–12, 1991.

[221] G. M. Zaslavsky. Renormalization group theory of anomalous transport in systems with hamiltonian chaos. *Chaos: An Interdisciplinary Journal of Nonlinear Science*, 4(1):25–33, 1994.

[222] G. M. Zaslavsky. *Hamiltonian chaos and fractional dynamics*. Oxford University Press, USA, 2005.

[223] G. M. Zaslavsky. *Physics of chaos in Hamiltonian systems*. World Scientific, 2nd edition, 2007.

[224] G. M. Zaslavsky, D. Stevens, and H. Weitzner. Self-similar transport in incomplete chaos. *Phys. Rev. E*, 48:1683–1694, 1993.

[225] H.-Y. Zhang, Z.-Q. Feng, S.-Y. Feng, and Y. Zhou. Typical algorithms for estimating hurst exponent of time sequence: A data analyst's perspective. *IEEE Access*, 12:185528–185556, 2024.

Index

C^k
  diffeomorphism, 33
  functions, 33

Action–angle variables, 23
Adjusted range (R), 92, 95
Area preservation, 38
Asymptotic stability, 36, 37

Backward orbit, 33
Bouncer model, 73
  complete version, 74
  finite-time Lyapunov exponents, 83
  fixed points, 82
  Hurst exponent in, 105
  Lyapunov exponents, 82
  phase space, 80
  static wall approximation, 79

Canonical coordinates, 18
Canonical transformations, 20
Cascade of bifurcations type trajectories (CBTT), 109
  Hurst exponent distribution in, 113
  Hurst exponent in, 111
Chaos definition (Devaney), 57
Commensurate frequencies, 24
Conservative generalized bifurcation diagram, 100
Conservative maps, 38
Constants of motion, 19
Continued fractions, 30
Contraction mapping theorem, 36

Dense sets, 58
diffeomorphism, 33
Diophantine condition, 29
Dynamical systems, 17

Finite-time analysis, 102, 111
Fixed points, 33
  Classification, 38
  Hyperbolic, 37
  stability, 36
Forward orbit, 33
Fractional standard map, 108

Hamiltonian formalism, 17
Hamilton–Jacobi equation, 21
Hamilton's characteristic function, 21
Hamilton's equations, 18
Harper model, 84
Hartman–Grobman theorem, 37
Heteroclinic points/orbits, 50
homeomorphism, 33
Homoclinic points/orbits, 50
Homoclinic tangles, 53
Horseshoe (Smale), 54
Hurst effect / Hurst phenomenon, 92
Hurst exponent
  distribution, 102, 105
  in bouncer model, 105
  in standard map, 98
  distribution, 113
  in Cascade of bifurcations type trajectories (CBTT), 111, 113
  in kicked Harper map, 105
Hyperbolic points, 37

Incommensurate frequencies, 24
Integrable systems, 21
Invariant directions, 49
Invariant manifolds
  global, 51
  local, 50
Irrational tori, 24

KAM theorem, 29
KAM tori, 29
Kicked Harper map, 85
    fixed points, 87
    Hurst exponent in, 105
    Lyapunov exponent in, 87
    phase space, 85

Lyapunov exponent
    in kicked harper map, 87
    in standard map, 72
    probability distribution, 73, 83, 88
    in Bouncer model, 82
Lyapunov exponents
    for one-dimensional maps, 60
    QR method, 62
Lyapunov stability, 36

Non-degeneracy condition (KAM), 31
Non-integrable systems, 25

Orbit
    backward, 33
    forward, 33
    periodic, 33

Periodic orbit, 33
Phase space, 18
Poincaré map / section, 40
Poincaré–Birkhoff theorem, 44

Quasi-Integrable Systems, 25

R/S analysis, 95
Rational tori, 24
Riemann–Liouville Fractional standard map (RLFSM), 108
Rotation number, 25

Sensitive dependence on initial conditions, 57
Smale horseshoe, 54
Small denominators problem, 28
Standard deviation, 92
Standard map, 66, 97
    Hurst exponent in, 98
    Lyapunov exponent, 72
    phase space, 70
    fixed points, 71
Stickiness, 96
Stroboscopic maps, 41

Topological Conjugacy, 33, 35
Topological transitivity, 57
Twist maps
    perturbed, 43
    unperturbed, 42

Winding number, 25